

**USING LONGWAVE INFRARED  
SPECTROSCOPY TO  
DIFFERENTIATE SILICA AND  
CALCITE VARIETIES AS  
POTENTIAL SCALING  
INDICATORS WITHIN  
GEOHERMAL SYSTEMS**

LAWRENCE ONYANGO AMOLLOH

July, 2020

SUPERVISORS:

Dr. Chris Hecker

Dr. Arjan Dijkstra





# **USING LONGWAVE INFRARED SPECTROSCOPY TO DIFFERENTIATE SILICA AND CALCITE VARIETIES AS POTENTIAL SCALING INDICATORS WITHIN GEOHERMAL SYSTEMS**

LAWRENCE ONYANGO AMOLLOH

Enschede, The Netherlands, July, 2020

Thesis submitted to the Faculty of Geo-Information Science and Earth Observation of the University of Twente in partial fulfilment of the requirements for the degree of Master of Science in Geo-information Science and Earth Observation.

Specialization: Applied Remote Sensing for Earth Sciences (ARS)

## **SUPERVISORS:**

Dr. Chris Hecker

Dr. Arjan Dijkstra

## **THESIS ASSESSMENT BOARD:**

Prof. Victor Jetten (Chair)

Dr. Martin Schodlok (External Examiner, Federal Institute for Geosciences and Natural Resources (BGR), Germany)

#### DISCLAIMER

This document describes work undertaken as part of a programme of study at the Faculty of Geo-Information Science and Earth Observation of the University of Twente. All views and opinions expressed therein remain the sole responsibility of the author, and do not necessarily represent those of the Faculty.

## ABSTRACT

Mineral scaling is a common problem in many geothermal environments around the world with significant effects such as a decline in geothermal energy production and the costs involved in controlling its formation or removing the already formed. Mineral scaling may form in surface steam pipes, generator blades, inside the wellbore casings, or within reservoir openings (e.g., fractures, vugs, and veins) through mineral precipitation as a result of temperature-pressure changes. The formation of such minerals that result in scaling in any given geothermal environment is dependent on the reservoir fluid chemistry, mineralogical composition of the reservoir rock, and the prevailing temperature-pressure conditions amongst others. The most problematic mineral scaling widely experienced include silica, calcite, and metallic scaling. Determination of minerals such as quartz, chalcedony, amorphous silica, and platy calcite associated with the formation of scaling may provide useful information about the reservoir conditions for quick decision making including whether that well can be fit for steam production once completed or drilling should be stopped. Currently, such decisions are based on geochemical fluid analysis which is mainly done after drilling completion. This study intended to establish whether LWIR spectroscopy can be used to detect and distinguish the different silica polymorphs and calcite varieties using pure samples which can then be applied to geothermal drill cuttings. Image data were acquired using a hyperspectral OWL LWIR camera. The LWIR images were preprocessed then processed using the Minimum Noise Fraction (MNF) transform method. Regions of interest were created and reflectance spectra extracted and converted into emissivity for interpretation. Other analysis techniques including XRD, FTIR-ATR, and SWIR imaging spectroscopy were also used to compare the results of the LWIR imaging analysis. From XRD and FTIR-ATR results, some samples were determined to have been wrongly classified based on the accompanying documentation and therefore had to be renamed accordingly. The LWIR spectroscopy results indicate that the various silica polymorphs have distinguishing features that can differentiate them from one another. Quartz and chalcedony have similar emissivity feature shape but chalcedony has a deeper main emissivity feature (about 1.5 times that of quartz). Both quartz and chalcedony have main emissivity peaks at longer wavelengths (~8600 nm) compared to ~8200 nm for the opaline silica series as well as tridymite. The 2<sup>nd</sup> emissivity feature is also at longer wavelengths (~8300 nm) compared to ~8200 nm for tridymite and ~8000 nm for opaline silica series. Opal-A has local emissivity features at longer wavelengths at ~11500 and ~10200 while opal-CT has its local emissivity features at shorter wavelengths at ~8500 nm and ~8800 nm. The 2<sup>nd</sup> feature of tridymite at ~8200 nm distinguishes it from the opaline series (~8000 nm). Cristobalite sample is noted to resemble quartz with minor features suggestive of just cristobalite traces present in the sample. The opal-C spectrum shows some chalcedonic features which could be indicative of additional microcrystalline silica material. Crystalline silica polymorphs have their emissivity features at longer wavelengths compared to those of opaline silica at shorter wavelength positions demonstrating the effects of crystallinity changes. It is also evident that no significant spectral changes can be attributed to the color appearance of the opaline silica series. Even though there are evidence of minor spectral shape differences and wavelength shifts amongst the calcite samples, the results could not be used to confirm the identity. A variety of bladed samples needs to be imaged for comparison. This study, therefore, has demonstrated that LWIR spectroscopy is an ideal technique that can be used in characterizing the different silica varieties.

## ACKNOWLEDGEMENTS

First and foremost, I thank God for giving good health and perseverance throughout this program.

Secondly, I would like to acknowledge my employer, the Kenya Electricity Generating Company (KenGen), and ITC for the great opportunity offered to me through this sponsorship to pursue this MSc program in Geo-Information Science and Earth Observation with specialization in Applied Remote Sensing for Earth Science. Thank you.

Much appreciation to my supervisors Dr. Chris Hecker and Dr. Arjan Dijkstra for their valuable guidance, constructive criticism, and encouragement. I Am also grateful for your help with the laboratory measurements and sample preparations. This would not have been successful without you. I also extend my appreciation to prof. dr. Freek van der Meer for his contributions during the proposal development.

Many thanks to the ITC's department of Earth Systems Analysis for their support in ensuring that the required data for the study were available. Particularly for the facilitation to acquire study samples, facilitating data collection in Kenya, and image acquisition at the Federal Institute for Geosciences and Natural Resources (BGR), Germany. Many thanks to the University of Twente's high-pressure laboratory department for using the facility to synthesize tridymite sample and Dr. Carolyn Lievens for the XRD sample measurements

Special thank you to Dr. Martin Schodlok of the Federal Institute for Geosciences and Natural Resources (BGR), Germany for the great help with image acquisitions. I also want to thank Prof. Steven Ruff from Arizona State University for providing a spectrum of chalcedony that was used to positively identify the study chalcedony.

I also extend my appreciation to my colleagues at KenGen for the different ways they contributed to the successful completion of this work. Special thank you to Mr. P. Mangi, Mr. Kizito Opondo, Mr. F. Wekesa, Mr. V. Otieno, Mr. V. Bosire, Miss E. Bonyo, and the fantastic geology team that was instrumental during data collection.

I would also like to appreciate my fellow ARS students particularly Akhil, Doreen, and Meaza for their contributions towards this study and other students from other departments, Emily, Dickson, and others for the support and encouragement and the moments we shared. I will never forget you.

Lastly, am deeply grateful to my family members especially my mum, my sister Lucy, my brother Nick, and my niece Alyn and friends for their unending prayers, love, and support throughout this period. I appreciate and love you all. May God bless you immensely.

# TABLE OF CONTENTS

---

1.	INTRODUCTION.....	7
1.1.	Background.....	7
1.2.	Research Objective.....	9
1.3.	Previous studies .....	9
2.	DATASETS.....	12
2.1.	Mineral Samples.....	12
2.2.	Secondary datasets.....	15
2.3.	Geothermal drill cuttings .....	16
3.	RESEARCH METHODOLOGY .....	18
3.1.	Laboratory Synthesis of Tridymite Sample.....	18
3.2.	LWIR and SWIR image acquisition .....	18
3.3.	Data processing.....	20
3.4.	FTIR-ATR measurements .....	23
3.5.	X-Ray Diffraction (XRD) sample analysis.....	23
4.	RESULTS .....	26
4.1.	Image processing results .....	26
4.2.	XRD analysis .....	29
4.3.	FTIR-ATR analysis .....	33
4.4.	LWIR spectral features of silica polymorphs .....	35
4.5.	Spectral feature difference in the silica polymorphs .....	42
4.6.	Spectral feature changes in silica polymorphs due to increase in crystallinity .....	43
4.7.	Effect of color on spectral features of opaline silica series.....	43
4.8.	Quantitative analysis of LWIR and XRD features (e.g., magnitude, depth and width) of silica polymorphs.....	43
4.9.	LWIR spectral features of calcite varieties.....	44
4.10.	SWIR Image analysis results.....	45
5.	Discussions .....	48
5.1.	LWIR spectral feature differences of silica polymorphs and how they compare to published data .....	48
5.2.	LWIR spectral differences due to crystallinity of silica polymorphs.....	51
5.3.	LWIR spectral feature differences of different colored opaline silica .....	51
5.4.	Quantitative comparison of LWIR and XRD features (e.g., magnitude, depth and width) of silica polymorphs.....	52
5.5.	Calcite LWIR spectral feature differences in comparison with published data .....	52
5.6.	Possible cause of shifts in spectral feature positions in calcite varieties.....	52
6.	CONCLUSIONS AND RECOMMENDATIONS .....	53
6.1.	Conclusions .....	53
6.2.	Recommendations.....	54

## LIST OF FIGURES

---

Figure 1: Image 1(a), showing from left to right cristobalite (Crist) which is marked with a red spot, chalcedony (Chalc), and quartz sample1 (Qtz1) and quartz sample2 (Qtz2) in fig. 1 (b) respectively.....	13
Figure 2: Opal-A mineral samples from left to right; OA_Aus1 and OA_Aus2 (from Queensland Australia), OA_Eth (from Shewa, Ethiopia), and OA_Gre (from Naxos, Greece) respectively.....	14
Figure 3: Opal-CT samples from left to right; OCT1, OCT2, OCT3, OCT4, OCT5, and OCT6 respectively. The similar arrangement used while scanning (OCT1 in front) except for OCT6 which was scanned in a separate group.....	14
Figure 4: Calcite sample varieties used in the study. From left to right; Bcalc, Calc1, and Calc2 respectively. Note that the triangular plane on Calc2 is not a facet/cleaved plane but a cut surface.....	15
Figure 5: Image showing some of the collected geothermal drill cuttings. Sample identification including well ID and depth of sampling.....	17
Figure 6: Image on the left (a) shows samples arranged on a plank of wood using putty while (b) shows samples arranged inside a box filled with sand during sample preparation for imaging .....	20
Figure 7: Images of selected individual bands after forward MNF transform showing the reducing image quality in the different image bands as observed from the box containing Grp2 samples .....	21
Figure 8: Flowchart summarizing the processes involved in data acquisition and analysis. ....	25
Figure 9: Image spectrum from Qtz1 sample before processing (a) and after applying MNF processing (b) .....	26
Figure 10: Comparison of image single-pixel emissivity spectrum and averaged ROI-based pixels' emissivity spectrum.....	26
Figure 11: An example of spectra compared without continuum removal (A), when continuum removed (B) and the stacked plots of the continuum removed (C) .....	27
Figure 12: Appearance of spectral features after spectral normalization, unstacked spectra (a), and stacked spectra (b). ....	27
Figure 13: XRD diffractograms of Crist sample showing peaks matching opal-C and opal-CT peaks confirming its mineralogy (cristobalite). Quartz peaks also present .....	29
Figure 14: XRD diffractograms of the crystalline silica series (cristobalite, quartz, chalcedony, & the synthesized tridymite sample).....	30
Figure 15: XRD diffractograms of the different opaline silica series (opal-A, opal-C & opal-CT samples). Q, T, and C represent quartz, tridymite & cristobalite peaks respectively.....	31
Figure 16: Diffractograms showing differences between opal-C, chalcedony, and quartz .....	32
Figure 17: XRD diffractograms of calcite samples1 (Calc1), sample2 (Calc2), and bladed calcite (Bcalc) showing the main intensity peaks (C1, C2, C3, C4).....	33
Figure 18: FTIR-ATR absorbance feature comparison of crystalline silica polymorphs (a) and opaline silica (b).....	34
Figure 19: FTIR-ATR spectral comparison of the study calcite samples with varying magnitudes and width. Features compared with published data .....	35
Figure 20: Stacked normalized sample spectra of Qtz1 and Qtz2 samples compared to JPL and ASU spectral libraries (a) and LWIR image in RGB (R~38, G~29, B~13) with ROIs where the average spectra were extracted (b).....	36
Figure 21: Chalc sample spectra compared with the published USGS library spectrum and a single chalcedony spectrum obtained from prof. Steven Ruff (Arizona State University) in (a) and an RGB image (bands 38, 29 & 13) with ROIs (b).....	37

Figure 22: Emissivity spectra of silicic-acid synthesized tridymite powder sample and an ASU spectral library spectrum. Dotted lines indicating positions of the main emissivity minima.....	38
Figure 23: Spectral features of cristobalite sample measured compared to the cristobalite spectra from the ASU spectral library.....	39
Figure 24: Spectra of opal-A samples (OA_Aus1 & OA_Aus2) compared with the standard USGS spectral library spectrum (left) and sample RGB image (38, 29, 13) showing ROIs locations of OA_Aus1 (top) and OA_Aus2 (below) (right). .....	40
Figure 25: Spectral features of Opal-CT samples compared to ASU spectral library spectrum (a). RGB (38, 29, 13) of LWIR images (b) arranged top to bottom similar to the respective sample spectrum showing ROI. Dashed lines show feature positions.....	41
Figure 26: LWIR spectra of the opal-C sample compared to an ASU library spectrum (opal-CT/C) in (a) and RGB image showing ROI 1&2 locations for OC_Gre_1 and OC_Gre_2 spectra respectively (b) .....	41
Figure 27: Plots (a) showing the spectral feature differences between the studied silica polymorphs while (b) shows differences between opaline silica series.....	42
Figure 28: Sample spectra of calcite varieties matched with standard library spectra (fig. a) and RGB of the LWIR image with the ROI where the averaged spectra were extracted (fig. b).....	45
Figure 29: SWIR spectral features of different calcite varieties compared to the USGS spectra and stacked together .....	46
Figure 30: SWIR spectra of opal-C (a), opal-CT samples (b), opal-A samples (c), and comparison of opal-A sample spectra with USGS library spectrum and TSG spectrum (d).....	47

## LIST OF TABLES

---

Table 1: Summary of datasets used in the study analysis and validation and their sources .....	16
Table 2: Specifications of the OWL LWIR camera and SWIR camera used for imaging (source: <a href="https://www.specim.fi/products/owl/">https://www.specim.fi/products/owl/</a> ) .....	19
Table 3: Calculated FWHM and depths of the LWIR deepest spectral features for the silica polymorphs	43
Table 4: FWHM and magnitude of XRD main peaks for the silica polymorphs calculated using Scherrer equation.....	44

# 1. INTRODUCTION

## 1.1. Background

Geothermal energy is one of the clean, safe, and reliable energy sources besides wind and solar energy. It exists below the earth's surface at great depths (Majorowicz and Minea, 2015) under high temperature and pressure conditions. Exploitation of this resource starts with the exploration to map out prospecting areas and to confirm the resource availability using different techniques. Numerous previous studies (e.g., Richter et al., 2010; Coolbaugh et al., 2007; & Calvin et al., 2015) have explained different methods employed in geothermal energy exploration. The determinant subsurface conditions for the occurrence of a geothermal resource include permeability, heat source, temperature conditions, geothermal fluids composition, and the reservoir rock type.

Continuous geothermal exploitation worldwide experiences challenges with optimum energy production and efficiency due to mineral scaling. Scaling is the precipitation or deposition of minerals from saturated geothermal fluids within geothermal environments due to changes in temperature and pressure conditions and fluid composition resulting from water-rock interaction (Alt-Epping et al., 2013). Scaling occurs within the reservoir (fractures, veins, vugs), wellbore casings, surface steam pipes, or on the generator blades during production (Godinho & Withers, 2018; van den Heuvel et al., 2018; Simmons and Christenson, 1994). Due to scaling, clogging of the surface pipes and wellbore casings or reservoir voids may take place, hence reduced fluid flow or loss of porosity.

Extensive studies on mineral scaling prediction and monitoring within geothermal systems have been done using geochemical analysis of geothermal fluids (Jamero et al., 2018; Poonoosamy et al., 2019; Diamond & Alt-Epping, 2014; García et al., 2005). Observations have indicated that some scalings such as metal sulfide scales may result in corrosion of the well casings (Akaku, 1990). To avoid such situations, therefore, an earlier understanding of the scaling potential and type of mineral scaling likely to occur may guide in determining the type of casing materials to be used in any particular production wells. Though a useful method, the geochemical analysis of the geothermal fluids may not be appropriate where an immediate decision is required on-site while drilling is still ongoing.

Nonetheless, it has been suggested that the characterization of hydrothermal alteration minerals could be employed towards understanding and predicting likely future scaling tendencies (Reyes, 1990). It has also been demonstrated by Hedenquist (1991) that there exists a relationship between fluid composition and distribution, and hydrothermal alteration mineralization characterized from drill cores.

The most common and problematic mineral scaling experienced in geothermal environments include, but are not limited to, silica and carbonate scaling (Haklidir & Haklidir, 2017). Specifically, amorphous silica (opal-A) and platy calcite (also referred to as bladed calcite) are the common forms of silica and carbonate scaling, respectively (Simmons & Christenson, 1994; Haklidir & Haklidir, 2017). Other silica polymorphs likely to form scaling include, quartz, chalcedony, and cristobalite depending on the prevailing temperature and pressure conditions and the water-rock interaction.

Silica and calcite occur in different varieties in varying crystal structures but with similar mineralogical compositions depending on the subsurface temperature and pressure conditions. Silica occurs in varying stability temperature and pressure conditions either in crystalline or non-crystalline varieties. Quartz, chalcedony, cristobalite, and tridymite are some of the crystalline forms of silica. Despite the identical chemistry of the different silica polymorphs, it is noted that their structural differences result in slightly

different vibrational absorptions that can be used to distinguish the minerals from each other (Michalski et al., 2003). The non-crystalline silica consists of the amorphous opaline silica series polymorphs (Ruff et al., 2011). The hydrated opal-A, considered more amorphous, opal-C that nearly resembles cristobalite, and opal-CT comprising of both cristobalite and tridymite, are the amorphous/microcrystalline silica polymorphs of opaline silica (Awadh and Yaseen, 2019; Elzea et al., 1994). Opal-A is known to precipitate from saturated silica-rich fluids. Opal-CT is a disordered microcrystalline form of cristobalite and tridymite that forms within an amorphous silica matrix (Elzea et al., 1994).

The formation of calcite mineral may result as a replacement mineral from calcium aluminosilicates or as a precipitate mineral in open voids (Simmons and Christenson, 1994). Calcite precipitates as platy calcite, and may contain impurities such as MgO, FeO and MnO compared to the pure calcite (Simmons and Christenson, 1994). Platy calcite indicates a calcite supersaturation of geothermal fluids due to the loss of CO<sub>2</sub> (Libbey and Williams-Jones, 2016) and can be associated with reservoir zones with boiling conditions (Simmons et al. 2000; Stimac et al. 2019).

Accurate identification of the various silica/calcite varieties within a geothermal reservoir would provide important information about the prevailing reservoir conditions which in turn could be useful in predicting the type of the expected mineral scaling. However, widely used conventional identification methods for mineral identification (binocular/petrographic microscope, X-ray diffractometer (XRD), fluid inclusion studies) cannot accurately distinguish the different silica varieties. For example, amorphous and cryptocrystalline silica varieties are not easily identified using a microscope (Awadh and Yaseen, 2019). Opaline silica, cristobalite, and chalcedony are not easy to differentiate under a binocular microscope but possible in petrographic and XRD (Bargar et al., 1993). Individual opaline silica polymorphs (opal-A, opal-CT, opal-C) are also difficult to distinguish under the microscope. Moreover, opaline silica is easily confused with cristobalite due to the cristobalite content present in the opal-C and opal-CT (Jébrak, 2015). It is also worth noting that conventional methods are time-consuming for sample preparation, difficult to implement at the well site or prone to misidentification of closely related minerals.

This study proposes to carry out an analysis of well-characterized silica/calcite varieties to establish their spectral signature differences with longwave infrared (LWIR) spectroscopy, which in turn can be used on real-world downhole geothermal drill cuttings characterization. This will help towards the identification and quantification of scale minerals such as chalcedony, amorphous silica, and platy calcite, which can be used to infer scaling tendencies.

Spectroscopy uses the spectral absorption features and wavelength positions for mineral composition and abundance mapping (Clark, 1999; Calvin & Pace, 2016; Fox et al., 2017). LWIR spectral range is specifically known for the detection of thermal infrared (TIR) active silica, carbonate, and feldspar-rich minerals within the range of 8-12  $\mu\text{m}$  (Bedell et al., 2017). Although detectable in the LWIR region, the carbonate-rich varieties are also active in the SWIR region with clear distinguishable absorption features.

**LWIR spectral imaging enables a more heterogeneous and representative mineral identification from image data as opposed to point-based measurements.** LWIR spectral imaging technique on drill cores has been deemed useful as demonstrated by studies such as Tappert et al. (2015). Successful differentiation of different opaline silica polymorphs from each other, and cristobalite, as observed in Ruff et al. (2011) is an indication that LWIR can be used in the mapping of the silica and calcite varieties. The spectral differences of the various silica varieties have also been reported by Michalski et al. (2003). On the other hand, calcite is both SWIR and LWIR active with distinct spectral signatures in the two spectral regions.

## 1.2. Research Objective

### 1.2.1. Overall objective

- To differentiate various silica and calcite varieties as potential scaling indicators within geothermal systems using hyperspectral longwave (LWIR) imaging spectroscopy

#### 1.2.1.1. Specific objectives

##### Objective 1

Establish the possible spectral feature differences between various silica/calcite varieties from pure, well-characterized samples using LWIR spectroscopy

##### Research Questions

- ❖ What are the LWIR spectral feature differences from the various silica polymorphs/ calcite varieties? How do they compare to those in published standard spectral libraries?
- ❖ How does an increase/decrease in crystallinity influence the spectral features in the silica polymorphs?
- ❖ Do opal series of different colors (i.e. in the visible range) also show differences in their LWIR spectrum?
- ❖ Can we establish a quantitative link between the spectral feature shape (e.g. position, depth, width) in the LWIR spectra and in the XRD diffractograms for the opal series/ silica?
- ❖ How does the spectral absorption features relate to the structure of the different silica/calcite polymorphs?
- ❖ What are the possible causes of shifts in wavelength positions of the different calcite forms if any?

##### Objective 2

In the original research plan, there was a second major objective: Apply the results on real drill cuttings from production geothermal wells from Olkaria Geothermal Field. However, due to the ongoing global COVID-19 pandemic which severely limited access to the laboratory, it could not be included in this thesis research.

## 1.3. Previous studies

Silica is one of the abundant rock-forming mineral groups that occur below the earth's surface either in crystalline or non-crystalline form. The different silica polymorphs occur in varying geological environments depending on the surrounding temperature and pressure conditions. Quartz, tridymite, and cristobalite are crystalline silica series while chalcedony is cryptocrystalline silica but in some studies often referred to as microcrystalline quartz (Smith, 1998). On the other side, the non-crystalline silica generally refers to the opaline silica polymorphs. The opaline silica polymorphs include opal-A (amorphous silica), opal-CT, and opal-C.

### 1.3.1. Crystalline silica

Chalcedony is described as microcrystalline quartz by some researchers while others refer to chalcedony as crystalline silica. Chalcedony is reported to be structurally bonded by a hydroxyl bond (Si-OH) in addition to the silica bonds Si-O and Si-O-Si (Schmidt and Fröhlich, 2011). The presence of the hydroxylated band in chalcedony, therefore, differentiates it from the crystalline quartz. Cristobalite is a high-temperature silica polymorph common in volcanic rocks at temperatures above 1470°C. Cristobalite occurs within high-silica content volcanic systems or vesicles in many hydrothermal environments, (Smith, 1998). The occurrence of cristobalite has also been associated with opal-C which in some studies is referred to as cristobalite due to its cristobalite-like stacking. Cristobalite is reported to have the Si-O

and Si-O-Si structural bonds, (Smith, 1998). Tridymite just like other silica polymorphs is also associated with volcanic environments. It is defined by two main disordered bonding structures of Si-O and Si-O-Si respectively.

### 1.3.2. Opaline silica (non-crystalline silica)

Opaline silica polymorphs occurrences and differences have extensively been studied, (Awadh and Yaseen, 2019; Herdianita et al., 2000; Milliken et al., 2008; Ruff et al., 2011; Goryniuk, 2004; Chauviré et al., 2017; Lynne et al., 2005). Recent studies such as Curtis et al., (2019), further details the classification of different opaline silica series while comparing the already known opals to new additional samples from newly identified localities. The opaline silica represents the hydrated non-crystalline silica polymorphs with a formula,  $\text{SiO}_2 \cdot n\text{H}_2\text{O}$ . The opaline water content can either be internally contained or surficial silanol group (-Si-OH) or occur as an adsorbed water, (Smith, 1998). The opaline minerals generally form in hydrothermal systems of temperatures  $<100^\circ\text{C}$ . Opaline silica polymorphs may form as a result of hydrothermal alteration activities, precipitation, or continental weathering. These non-crystalline silica forms both below the earth's surface and on the surface where they occur as silica sinter which has widely been used in understanding the underlying conditions of geothermal systems (Herdianita et al., 2000; Ruff et al., 2011). The opaline silica forming on the surface are associated with steaming geothermal grounds such as fumaroles, geothermal geysers, and geothermal vents. The opaline silica is characterized by the varying environmental conditions including temperature, pH, and water-rock reactions, (Ruff et al., 2011). Mostly documented opaline silica series comprises of opal-A, opal-C, and opal-CT. Structurally, the opaline series polymorphs are defined by the Si-O vibrational modes associated with Si-O-Si and Si-OH structures respectively, (Goryniuk, 2004). Another important characteristic of most of the opaline silica polymorphs is their play-of-color display described by Mukherjee (2011) as light interference on the surface caused by the diffracted light by the closely packed hydrated silica spheres forming the opaline silica minerals.

Opal-A, also known as the amorphous silica is the most common polymorphs of the opaline silica series. The amorphous nature of the opal-A as a result of its highly-disordered non-crystalline structure. It is hydrated silica composed of water component (OH) structurally bonded to the silanol (Si) component, (Goryniuk, 2004). The water present in the opal-A can be both absorbed and trapped water or just either of the two. Different Opal-A samples may appear to have a play-of-color nature just as the opal-CT silica mineral, (Curtis et al., 2019). The opal-CT is non-crystalline opaline silica mainly defined by the disordered cristobalite-tridymite mineral stacking structure, an indication of the presence of both cristobalite and tridymite atoms, (Smith, 1998). Smith, (1998) further observes that opal-CT represents the mostly cavity-deposited opaline silica within volcanic rocks. Studies such as Elzea et al., (1994), have also shown that opal-CT can occur in different levels of stacking disorders. The other opaline silica polymorph opal-C is characterized by the well-ordered cristobalite mineral stacking. Opal-C mainly forms due to volcanic ash alteration, similar to opal-CT as opposed to opal-A, (Elzea et al., 1994).

### 1.3.3. Calcite formation

Calcite mineral is considered as the pure form of carbonate mineral group ( $\text{CaCO}_3$ ) compared to other carbonate mineral forms such as magnesite, dolomite, siderite, and ankerite. The mineralogical differences of the carbonate varieties are associated with the presence of either magnesium, iron, or manganese cations in the carbonate material (Green and Schodlok, 2016). From thermal spectroscopy studies of the various carbonate minerals, it has been noted that such cations may alter the overall spectral feature appearance and shifts in wavelength positions of the major features (Green and Schodlok, 2016; Lane and Christensen, 1997). Calcite has a diagnostic feature near  $\sim 11300$  nm but shifts to either shorter or longer

wavelength positions depend on the type of cation present which results in the formation of a different carbonate form (Green and Schodlok, 2016; Lane and Christensen, 1997).

Calcite also exists in different forms under different geological environments. Platy calcite (also known as bladed calcite) is a common form of calcite that forms through precipitation in open spaces such as fractures, veins, vugs, and in steam pipes within geothermal systems, (Simmons and Christenson, 1994). Mineralogically, platy calcite has been determined to contain other minerals most notably MgO, MnO, and FeO in low amounts as previously established from the platy calcite sample analysis from Ohaaki geothermal field (Simmons and Christenson, 1994).

## 2. DATASETS

The primary datasets used in this study are comprised of pure samples of silica and calcite mineral varieties considered to be associated with varying geothermal conditions. Specifically, the study considered crystalline silica polymorphs chalcedony, quartz, tridymite, and cristobalite, the non-crystalline opaline silica series opal-A (amorphous silica), opal-CT, and opal-C, and different calcite varieties including bladed calcite. These silica and calcite samples were considered essential for applying the proposed hyperspectral LWIR imaging spectroscopy and analysis to investigate the existing spectral feature differences of the respective mineral varieties.

Other secondary datasets needed to successfully carry out the study included previously published standard spectral libraries for comparison with the resultant extracted study sample spectra from the hyperspectral LWIR-scanned images for spectral feature and wavelength position characterization. Apart from the standard spectral libraries, published XRD diffractograms were also used for comparison.

The results of the hyperspectral LWIR imaging of the different silica and calcite varieties are intended to be applied to real-world downhole geothermal drill cuttings from Olkaria geothermal field, Kenya to characterize hydrothermal alteration minerals for possible mineral scaling indicators.

### 2.1. Mineral Samples

Different pure silica and calcite varieties of the proposed study minerals were obtained and analyzed to establish their spectral feature differences. These included silica polymorphs chalcedony, quartz, tridymite and cristobalite, and the non-crystalline opaline silica series opal-A, opal-CT, and opal-C. One of the study samples (opal-A samples) was identified to be an opal-C mineral although the accompanying documents indicated opal-A mineral description. Three different calcite mineral samples were also obtained and analyzed. The mineral samples were sourced from either the ITC mineral collection, from the Plymouth University mineral collection, from mineral dealers or from the ITC staff members' personal collections. Tridymite used in this study was synthesized within the University of Twente's (UT) high-pressure laboratory due to the unavailability of the natural mineral sample. Table 1 shows a summary of the samples used in this study. The analyzed mineral samples are described below.

All the study samples are strictly labeled and described in the **datasets section** based on the initial documentation accompanying the samples (e.g., OA\_Eth, OA\_Gre) but **the results and subsequent sections** have taken into account the XRD observations and re-naming for some of the samples (e.g., OA\_Eth changed to OCT\_Eth and OA\_Gre changed to OC\_Gre).

#### 2.1.1. Silica Polymorphs

##### 2.1.1.1. Crystalline Silica Series

The crystalline silica series comprised of chalcedony, quartz, tridymite, and cristobalite mineral samples. Two quartz samples were used in this study, quartz sample1 (Qtz1) and quartz sample2 (Qtz2) (Figure 1). Qtz1 is a translucent grey-brown smoky single crystal while Qtz2 on the other hand is a whitish mineral sample showing numerous quartz crystals cemented together. Both samples were sourced from within ITC's mineral archive. The cristobalite sample (Crist) was sourced from a mineral dealer 'PopularDesignWorks' through its online link <https://www.etsy.com/shop/PopularDesignWorks>. The cristobalite part of the sample is embedded within a phantom amethyst quartz crystal together with goethite arrows and hematite. It appears to have been formed through precipitation or deposition within a void/vesicle (Figure 1). The chalcedony sample (Chalc) used in this study is a grey fine-grained blue

chalcedony (agate) from a broken laboratory ring and puck mill (manufactured by Retch, Germany). For tridymite sample, the synthesized Trid\_silic powder (see Appendix 1f) was used for the analysis (synthesis process described in section 3.1).



a



b

Figure 1: Image 1(a), showing from left to right cristobalite (Crist) which is marked with a red spot, chalcedony (Chalc), and quartz sample1 (Qtz1) and quartz sample2 (Qtz2) in fig. 1 (b) respectively.

## 2.1.2. Non-crystalline silica (Opaline silica series)

### 2.1.2.1. Opal-A

Three opal-A representative mineral samples were obtained and used in the study. Samples were either obtained from amongst the ITC mineral collections or from a mineral museum. Opal-A from Ethiopia (OA\_Eth) and opal-A from Greece (OA\_Gre) (according to the samples' accompanying documentation) both came from the ITC collection while opal-A from Australia (OA\_Aus1 and OA\_Aus2) was obtained from the University of Plymouth mineral collection (originally obtained from mineral dealer Richard Tayler, UK.)

OA\_Aus1 and OA\_Aus2 appear to be hosted/embedded within a brown rock matrix sample with patches of blue and sky blue surfaces. Details from the source indicate that the host rock is 'ironstone' (iron-rich sedimentary rock). The samples are from Queensland, Australia (a more precise mineral location could not be obtained from mineral dealer Richard Tayler). OA\_Eth originated from the Yita Ridge in the Menz Gische district of Shewa Province, Ethiopia while OA\_Gre is from Naxos, Greece. OA\_Eth is glassy with brown/red reflections and is formed half-covered with an outer layer of another rock material. On the other hand, OA\_Gre is observed on the surface of the host rock appearing as colourless dissemination with some form of botryoidal appearance.



Figure 2: Opal-A mineral samples from left to right; OA\_Aus1 and OA\_Aus2 (from Queensland Australia), OA\_Eth (from Shewa, Ethiopia), and OA\_Gre (from Naxos, Greece) respectively.

### 2.1.2.2. Opal-CT

A variety of opal-CT opaline silica series samples were acquired for analysis. Two of the acquired opal-CT samples are whitish while the rest are in different shades of orange/brown colors. Samples were labeled opal-CT1 (OCT1), opal-CT2 (OCT2), opal-CT3 (OCT3), opal-CT4 (OCT4), opal-CT5 (OCT5) and opal-CT6 (OCT6) as shown in Figure 3. OCT2, OCT3, and OCT4 appear to be hosted within a different rock sample unit while OCT1 and OCT6 both are single crystals independent of any hosting material. OCT1 is white and shows a botryoidal structure with small brown spots on the surface while the remaining OCT samples appear glassy. OCT2 is also white like OCT1 but without brown spots. On the other hand, OCT3, OCT4, OCT5, and OCT6 all have different shades of brown/orange. OCT3 is orange, OCT4 appears glassy golden brown, OCT5 shows slight yellowish in appearance while OCT6 appears reddish-brown.

Most of the opal-CT samples including OCT2, OCT3, and OCT4 were sourced from the existing ITC mineral collections while OCT1 was bought from a mineral dealer (<https://www.etsy.com/shop/BallroomMiningCo>) and OCT6 was obtained from the University of Plymouth (from Richard Tayler mineral dealer). OCT6 is indicated to have originated from Rhodope Mountains, Bulgaria.



Figure 3: Opal-CT samples from left to right; OCT1, OCT2, OCT3, OCT4, OCT5, and OCT6 respectively. The similar arrangement used while scanning (OCT1 in front) except for OCT6 which was scanned in a separate group.

### 2.1.3. Calcite Varieties

Three different calcite minerals were acquired for this study. The acquired samples include bladed calcite and two other calcite minerals. Bladed calcite (Bcalc) was bought from a mineral dealer ‘Symbolsforthesource’ through an online link <https://www.etsy.com/shop/Symbolsfromthesource>. Details from the dealer indicated that the sample originated from China and is attached to a blue fluorite mineral

crystal. The bladed calcite sample is made up of plate-like crystals and generally colorless with slight brown tints. The other two calcite samples have rhombohedral crystal habits; the milky-white calcite crystal (Calc1) from the ITC mineral collection, and the clear and transparent (so-called 'Iceland spar') calcite crystal (Calc2) from Arjan Dijkstra's personal collection.



Figure 4: Calcite sample varieties used in the study. From left to right; Bcalc, Calc1, and Calc2 respectively. Note that the triangular plane on Calc2 is not a facet/cleaved plane but a cut surface.

## 2.2. Secondary datasets

### 2.2.1. Spectral libraries

Mineral spectra extracted from the study samples were compared to their corresponding existing published standard library spectra as well as unpublished spectral library mineral spectra. Published spectral libraries used include the US Geological Survey (USGS) (Kokaly et al., 2017), Arizona State University (ASU), (Christensen et al., 2000), and Jet Propulsion Laboratory (JPL) (Baldrige et al., 2009) standard spectral libraries. Additionally, study samples' spectra were also compared to the CSIRO spectral library (Schodlok et al., 2016) as implemented in The Spectral Geologist version 8. Another unpublished single chalcedony mineral spectrum was obtained from the Arizona State University through personal communication (with one, Steve Ruff).

### 2.2.2. Previous published XRD data

In addition to the laboratory XRD analysis of the various study samples at the ITC's Geosciences laboratory, previously published study results were also incorporated in this study to compare the results. These were mainly the previous studies related to silica polymorphs.

Table 1: Summary of datasets used in the study analysis and validation and their sources

Mineral	Sample Description	Source	Sample Locality
Quartz	Qtz1 Qtz2	Both from ITC mineral collection	
Cristobalite	Crist	Bought from a mineral dealer; <a href="https://www.etsy.com/shop/PopularDesignWorks">https://www.etsy.com/shop/PopularDesignWorks</a>	
Tridymite	Trid_silic	Laboratory-synthesized using silicic acid	
Chalcedony	Chalc	ITC staff personal mineral collection	
Opal-A	OA_Aus1 OA_Aus2	Two pieces of an Australian opal-A, University of Plymouth collection, originally from Richard Tayler mineral dealer.	Queensland, Australia
	OA_Eth	From ITC mineral collections	Yita Ridge, Menz in Shewa Province, Ethiopia
	OA_Gre	From ITC mineral collections	Naxos, Greece
Opal-CT	OCT1	Sourced from a mineral dealer; <a href="https://www.etsy.com/shop/BallroomMiningCo">https://www.etsy.com/shop/BallroomMiningCo</a>	
	OCT2 OCT3 OCT4 OCT5	From mineral museum or ITC mineral collections	
	OCT6	From University of Plymouth, originally from Richard Tayler mineral dealer.	Rhodope Mountains, Bulgaria
Calcite	Bcalc	1 sample from a mineral dealer; <a href="https://www.etsy.com/shop/Symbolsfromthesource">https://www.etsy.com/shop/Symbolsfromthesource</a>	
	Other calcite varieties; Calc1 Calc2	Obtained from the ITC mineral archive collections (Calc1) and ITC personal staff collections (Calc2)	

### 2.3. Geothermal drill cuttings

Fieldwork data collection was undertaken as part of the study although samples could not be analyzed due to travel restrictions and the inaccessibility of the laboratories to measure the samples due to the global COVID-19 pandemic. Fieldwork was undertaken between the 31<sup>st</sup> January 2020 and 25<sup>th</sup> February 2020 in Kenya at KenGen's Olkaria geothermal field. Geothermal drill cuttings were collected from pre-selected geothermal production wells experiencing mineral scaling problems and a production well with no issue of scaling for mineralogical comparison. Based on the mentioned parameters, the drill cuttings were collected from three production wells i.e., one silica scaling well, one calcite scaling well and one non-scaling well.

#### 2.3.1. Sampling criteria

The sample collection was limited to wells within the same field of production for a better understanding of the hydrothermal alteration mineralogy as a potential for mineral scaling at a smaller scale before the same could be conducted for the entire geothermal field. For this study, geothermal production wells were pre-selected from Olkaria East Production Field (OEPF).

Data collection was done from three production wells showing silica scaling problems, calcite scaling problems, and a non-scaling well respectively. For each case, one representative well was chosen. Samples were selected from wells OW-34, OW-41, and OW-35. OW-34 was selected for silica scaling analysis, OW-41 for calcite scaling analysis, and OW-35 was selected as a non-scaling well and due to its proximity to the other two wells.

Drill cuttings were selected within every 100 m depth range, and the selection of the exact sample within that depth range was guided by the mineral abundance, lithology, and the presence of veins, fractures, or voids respectively. The mineral abundances of quartz, chalcedony, or amorphous silica for the silica scaling well (OW-34), calcite abundance for the calcite scaling well (OW-41), and calcite and quartz abundance for the non-scaling well (OW-35) were considered. A total of 67 samples were collected (OW-34~21, OW-41~23, and OW-35~23) as detailed in **Error! Reference source not found.** Samples were packed on well-labeled sample bags with the details of the sample such as well ID and sample collection depth range.



Figure 5: Image showing some of the collected geothermal drill cuttings. Sample identification including well ID and depth of sampling

### 3. RESEARCH METHODOLOGY

Different sample analysis methods were employed in analyzing the mineral samples acquired for this study. These include the main study method of hyperspectral LWIR imaging, SWIR imaging, XRD analysis, and FTIR-ATR sample analysis.

Several step-by-step processes were carried out to the different datasets to ensure that the main goal of the study is achieved. First, the laboratory synthesis of the tridymite sample was undertaken. Thereafter, the laboratory-based hyperspectral image acquisition of the different mineral samples was done. The hyperspectral images were acquired using two different camera detectors, LWIR and SWIR hyperspectral cameras. The acquired hyperspectral images were then pre-processed, processed, and analyzed before representative sample spectra could be extracted from the images. Image processing was done to ensure that the final spectral features of the various study samples are free of noisy bands. Both XRD and FTIR-ATR measurements and analysis were carried out for the various samples at the ITC's Geosciences laboratory before comparing its results to the image analysis results as well as published XRD data from previous studies. Also, SWIR image analysis results were compared to the LWIR results.

#### 3.1. Laboratory Synthesis of Tridymite Sample

As already indicated, tridymite samples for this study were laboratory-prepared. The synthesis was attempted using two different starting materials: amorphous powdered silicic acid (Lenher, 1921), and fine-grained quartz (sourced from fluka). The two materials were used for tridymite synthesis to provide different tridymite samples for the LWIR imaging analysis and subsequent comparison. Silicic acid of high purity (Merck, >99% purity) previously heated to 900°C and fluka quartz of similar purity (e.g., fine-grained high purity crystalline quartz, previously heated to 900°C) were used in the synthesis of tridymite (Trid\_silic and Trid\_fq respectively).

The samples, silicic acid and fluka quartz were placed 2 g each on separate high-purity nickel crucibles at 1000°C. The samples were then heated for 6 hours in a conventional muffle furnace at the University of Twente's high-pressure laboratory. After 6 hours, the crucibles with the samples were removed from the cooling ovens (at approximate temperatures slightly >600°C) and quenched in the open air under room temperature (about 30 minutes). The synthesis method is similar to the one used in the cristobalite synthesis, (Shinohara and Kohyama, 1990). The already quenched synthesized tridymite samples were then analyzed using the XRD analysis method to determine whether the synthesis process was successful. From the XRD diffractograms, it was evident that the synthesis of tridymite from fluka quartz was unsuccessful since well-defined quartz peaks dominated the diffractogram, compared to the silicic acid-synthesized tridymite. Thus, the silicic acid synthesized powder sample (Trid\_silic) was used for the study although the sample also still showed quartz peaks an indication that it was not at 100% success.

#### 3.2. LWIR and SWIR image acquisition

Most silica and carbonate mineral varieties are known to be thermal infrared (TIR) active and therefore best identified in the TIR spectrum range. This has been demonstrated in many studies such as Bedell et al. (2017) and Michalski et al., (2003). Notable applications of the LWIR imaging technique is the imaging of drill cores demonstrated by Tappert et al. (2015). Detectable minerals in this spectrum range include quartz, calcite, adularia, chalcedony, and opaline silica varieties, amongst others. Thus, the LWIR hyperspectral imaging detector was selected as the main method to determine whether it can successfully be used in distinguishing in particular, the different silica polymorphs as well as calcite varieties. Image

data acquisitions were conducted at the Federal Institute for Geosciences and Natural Resources laboratory (BGR) in Hannover, Germany using Specim's OWL hyperspectral LWIR and SWIR cameras.

### 3.2.1. Camera Specifications

Hyperspectral LWIR camera used is a high sensitivity cooled MCT detector with spectral selectivity of 84 bands and an extensive speed of up to 100 frames/sec and spectral range of 8-12  $\mu\text{m}$ , (Specim, 2014). On the other hand, SWIR images were acquired using a 1000-2500 nm spectrum range hyperspectral camera. It is also a cooled MCT detector with 384 spatial pixels and 288 spectral bands and a signal to noise ratio of 1050:1 at the maximum signal level. Table 2 below shows the used cameras' specifications.

Table 2: Specifications of the OWL LWIR camera and SWIR camera used for imaging (source: <https://www.specim.fi/products/owl/>)

	OWL LWIR Camera	SWIR Camera
<b>Optical Characteristics</b>		
Spectral range	8-12 $\mu\text{m}$	1000-2500 nm
Spectral bands	84	288
Spectral resolution	100 nm	
Spectral sampling/band	48 nm	
Spatial pixels	384 pixels	384 pixels
<b>Electrical characteristics</b>		
Detector	MCT camera	Cryogenically cooled MCT camera
Numerical aperture	F/2.0	F/2.0
Pixel size	24x24 $\mu\text{m}$	24x24 $\mu\text{m}$
Cooling	Sterling-cycle cooler	Stirling, 25000 h MTTF)
Frame rate	Up to 100 fps	450 fps (max full frame)
SNR	Target 300K 8 $\mu\text{m}$ -450 10 $\mu\text{m}$ -580 12 $\mu\text{m}$ -230	1050:1 (at max. signal level)

### 3.2.2. Sample Preparation and Imaging

Samples were first prepared before the actual imaging was done. Samples were sorted and arranged into groups with the targeted sample surface to be imaged facing up (facing the camera light source). For image acquisition, the samples were arranged in groups as follows:

Grp1~Crist, Chalc & Qtz1;  
 Grp2~Bcalc, Calc1 & Calc2;  
 Grp3~OCT1, OCT2, OCT3, OCT5 & OCT4;  
 Grp3R~OCT1, OCT2, OCT3, OCT4 & OCT5;  
 Grp4~OA\_Aus1, OA\_Aus2, OA\_Eth & OCT6;  
 Grp5~OA\_Gre, Qtz2 & silicate;  
 Grp6~Calc2 & Calc1 and  
 Grp7~Trid\_silic & Trid\_fq respectively.

Samples from Grp2 and Grp5 were imaged from a sand-filled box. The rest of the samples from Grp1, 3, 3R, 4, and 5 with an exception of tridymite were all placed on a black wooden plank using putty from where they were imaged. The putty was used to mount the samples in position without movement on the wooden plank when imaging. Grp7 with the tridymite powder samples were placed in black-painted small

sample holders made of aluminum foil then placed on the wooden plank for imaging. Photos were taken of the samples showing the order of arrangement for possible reference during processing should there be a need (Appendix 1). Samples were then imaged using both hyperspectral LWIR and SWIR cameras. The highlighted groups (in gray) were not processed for analysis. the repeated measurement for Grp3R was used in the analysis of the opal-CT samples instead of Grp3. Figure 6 shows an example of a sample on top of a wooden plank and inside a sand-filled box.

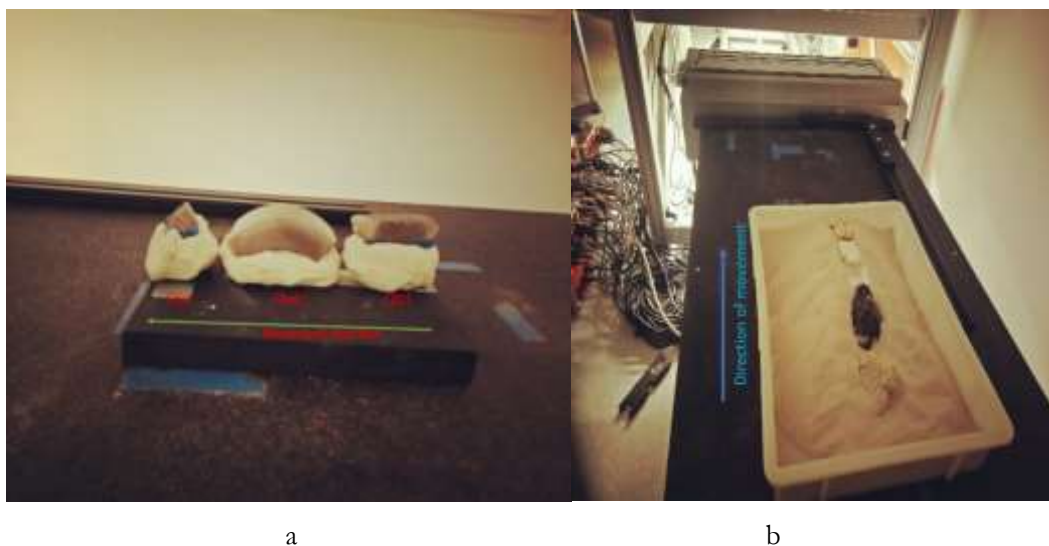


Figure 6: Image on the left (a) shows samples arranged on a plank of wood using putty while (b) shows samples arranged inside a box filled with sand during sample preparation for imaging

### 3.3. Data processing

#### 3.3.1. LWIR Image Pre-processing

Image data pre-processing was done at BGR after the images were acquired. This was done to calibrate the hyperspectral images into reflectance values from the digital number (DN) values to ensure the images are converted into an ENVI standard format datacubes.

#### 3.3.2. LWIR Image Processing

Initial examination of the pre-processed hyperspectral images showed some spectral bands to be noisy. The first 2-3 bands and last 3-6 bands in all the images were determined to be noisy using HypPy software. Similarly, the noise in the data appears to vary throughout the images which required to be reduced or removed. In this regard, the Minimum Noise Fraction transform (MNF) was selected to ensure spectral dimensionality is achieved, as well as noisy data, are suppressed from the image data (Calvin et al., 2015; Kruse et al., 2012; Vaughan et al., 2003). Spatial and spectral sub-setting of the images were performed alongside MNF transform data processing.

Using ENVI's MNF forward transform tool, the images were first sub-set spatially and spectrally to remove the pixels which are outside the imaged sample material as well as remove the noisy first and last bands respectively. From the different sample groups/box, the following bands were removed through spectral sub-setting: Grp1 image~ bands 1-2 and 98-101; Grp2 image~ bands 1-3 and 95-101; Grp3R image~ bands 1-2 and 98-101; Grp4 image~ bands 1-3 and 98-101; Grp5 image~ bands 1-3 and 95-101 and lastly Grp7 image~ bands 1-4 and 98-101 respectively. Forward MNF rotation was then performed and noise statistics file generated. Figure 7 shows an example of the forward MNF transform results from some of the bands with reducing image quality.

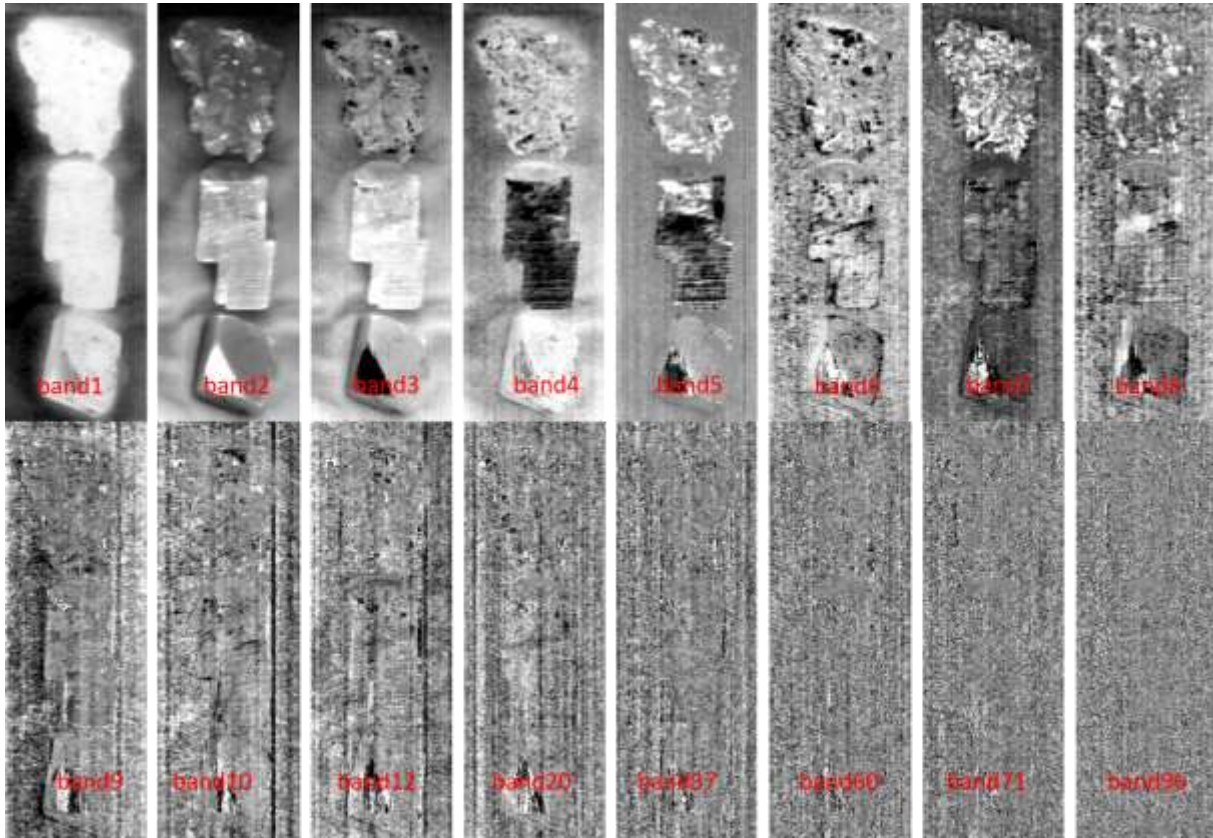


Figure 7: Images of selected individual bands after forward MNF transform showing the reducing image quality in the different image bands as observed from the box containing Grp2 samples

Forward MNF transform resultant image was examined based on individual bands and compared to the generated eigenvalues. This was to help in determining the number of principal image component bands with more information to be applied in the inverse MNF transformation to suppress noise. Eigenvalues with threshold values  $>2.0$  were therefore used in the inverse rotation. In the inverse MNF rotation, 14 component bands were applied on Grp1 and Grp2 images, 12 component bands on Grp3R image; 11 component bands on Grp4 as well as Grp5 images. Likewise, 13 component bands were used in Grp7 image.

### 3.3.3. Sample spectral feature extraction

Spectral features of the study samples were then extracted from the processed hyperspectral images. The spectra were based on the averaged pixels value spectrum instead of the individual pixel-based spectrum for a more sample representative spectrum (Figure 10). Therefore, regions of interest (ROI) were created for each of the individual sample images on different sample surfaces as shown on the various individual sample's RGB images in the results section.

### 3.3.4. Emissivity Calculation

Although the hyperspectral images were calibrated and the sample spectra extracted in reflectance values, they were later converted to emissivity values. This was to simplify their correlation with the published data which are mainly presented in emissivity and not reflectance. Thus, the reflectance spectra were converted to emissivity spectra by applying Kirchhoff's law, (Vaughan et al., 2003). The calculation was done in ENVI's spectral math tool using Kirchhoff's formula,

$$\varepsilon = 1 - r, \quad \text{Equation 1}$$

where  $\varepsilon$ =emissivity and  $r$ =reflectance

### 3.3.5. LWIR spectral normalization

Spectral normalization was done to all the sample spectra to ensure that their feature depths match those of the corresponding reference absorption features. This is because the corresponding library reference spectra and the study samples spectra have varying spectral contrast hence the difficulty in comparing/matching their respective absorption features. Spectral normalization enables the stacking of several sample spectra and library spectra together for easier feature comparison without losing clear visualization of the absorption features.

To ensure that features are comparable with enhanced spectral features, all the sample spectra and the corresponding standard libraries were normalized. The spectra were first individually continuum removed then normalized using an algorithm,

$$(S - \text{MIN}(S))/(\text{MAX}(S) - \text{MIN}(S)), \quad \text{Equation 2}$$

Where  $S$  represents an input spectrum while  $\text{Min}$  and  $\text{Max}(S)$  represent the lowest and highest variable reflectance/emissivity values from the input spectrum respectively.

This algorithm was applied to the continuum removed spectra using ENVI's spectral math tool. The algorithm ensures that all the spectra have their emissivity values range between 0-1 when stacked together for comparison.

### 3.3.6. SWIR data processing

Some of the studied samples are also minerals active within the SWIR spectrum range with distinct spectral features such as calcite, and opaline silica series (opal-A and opal-CT). Calcite, for example, has a carbonate diagnostic feature that is distinct in the SWIR range (Zaini et al., 2014). Therefore, SWIR hyperspectral images with the SWIR active samples (calcite, opal-A, and opal-CT) were analyzed and compared with the LWIR hyperspectral image analysis results.

#### ❖ *SWIR image pre-processing*

First, the SWIR obtained image datasets were calibrated by converting them into reflectance values, a standard ENVI data format, from the digital number (DN) values. The samples were acquired using a 50% reflectance standard, therefore, had to be calibrated to a maximum of 50% reflectance before further processing of the data. This was achieved by employing <fatuspec.sav>, a specim extension file used for pre-processing hyperspectral images, added into the ENVI program. Both dark and white reference images were used in the pre-processing to calibrate the SWIR image.

#### ❖ *SWIR Image Processing*

The hyperspectral SWIR images were then processed using the same procedure applied in the hyperspectral LWIR images. Images were first examined using HypPy program to determine the noisy bands that needed to be removed or any bad band that required prior processing before the actual analysis process. Subsequently, the first bands 1-3 and the last band 288, were observed to be very noisy thus need to subset.

Minimum Noise Fraction transformation (MNF) was used in the analysis of the images. Both spatial and spectral subset was performed during the MNF transformation process. Sub-setting was performed to remove the pixels outside the target material through spatial subset and removal of bands 1-3 through spectral subset. As a result, fewer component bands determined to have information were selected based on the resultant eigenvalues plot and used in the inverse MNF rotation. Eigenvalues with thresholds  $>2.9$  (35 component bands),  $>2.0$  (45 component bands),  $>2.0$  (31 component bands), and  $>3.0$  (20 components) were used in the inverse MNF transform for Grp3R samples, Grp4 samples, Grp5 samples, and Grp2 samples respectively. Regions of interest (ROIs) were later created in the same spots as on the LWIR images for comparison purposes from which an average sample spectrum was extracted. The extracted spectra were continuum removed then normalized using an algorithm (see Equation 2) through spectral math tool in ENVI. Hence, the normalized sample spectra were compared to the published and unpublished spectral libraries and stacked for easier and better visualization. Both HypPy and ENVI software were used in pre-processing, processing, and analysis of the image data.

### 3.4. FTIR-ATR measurements

Attenuated total reflectance Fourier transform infrared (FTIR-ATR) spectroscopy, have widely been used in mineral groups identification qualitatively and also in quantifying mineral content, (Henry et al., 2017; Müller et al., 2015). In this study, the FTIR-ATR method was used measurements of the study samples to compare the results with the LWIR imaging results. Samples were measured using ITC's Bruker Vertex 70 ATR and samples recorded at  $4\text{ cm}^{-1}$  resolution with 64 scans setting.

Measurements were carried out on the XRD-powdered samples as described in the XRD sample analysis section and also contained in a sample preparation logfile, (Appendix 2). Measurements were done by placing the powdered samples onto a diamond crystal before closing the anvil and thereafter running the measurement. Sample measurements were done in duplicates (although not all). Cleaning of the diamond crystal where the samples were placed as well as the anvil was done using ethanol after every single measurement to avoid contamination of the subsequent sample. However, for Calc2 and Crist samples, the same sample was re-run without a new background measurement. Baseline correction for the measurements was then conducted to correct for the atmospheric effect.

### 3.5. X-Ray Diffraction (XRD) sample analysis

X-ray diffraction (XRD) or X-ray powder diffraction is a non-destructive laboratory technique useful in determining the crystallographic structure and chemical composition of minerals. It has been used in numerous studies in mineral mapping and differentiating crystalline from non-crystalline materials on its own or in combination with other techniques; (Awadh and Zahir, 2019; Elzea et al., 1994; Koerting et al., 2015 & Ilieva et al., 2007).

XRD analysis was carried out at the ITC faculty's Geoscience Laboratory using a Bruker D2 Phaser X-ray diffractometer (Fox et al., 2017; Awadh & Zahir, 2019). Different techniques were applied to the different samples to obtain powder for analysis. Large samples with enough material were powdered using a Zirconia ball mill while smaller samples were powdered using a mortar and pestle. A tungsten steel scriber was also used to scratch off powder onto an XRD wafer from two samples. Samples Qtz2, Chalc, OCT6, and Bcalc, were powdered using ball milling. First, a sample piece was broken from each of these samples using a hammer. To avoid contamination, samples were wrapped using a paper towel. The hammered pieces were divided equally into two similar ZrO<sub>2</sub> milling jars, and then seven milling balls were added to each. The samples were then milled for five minutes at 550 rpm. This procedure was repeated for all the four samples while cleaning all the materials used before and after every measurement to avoid contamination. Powdered samples were put into well-labeled small sample bags.

Using a mortar and pestle, samples were manually ground to fine powder ready for analysis. However, the different samples were first crushed into pieces before manual selection of the cleanest pieces, which were then ground in the mortar. Through manual selection, the amount of the host rock samples was minimized. OA\_Gre, OA\_Aus2, OA\_Eth, OCT1, OCT2, OCT3, OCT5, and Calc1 were all powdered using mortar and pestle.

For Calc2 sample, a tungsten steel scriber was used to scrape powder samples directly into an XRD wafer from the damaged edge of the sample for measurement. XRD powder sample was also extracted by drilling into the embedded cristobalite material hosted in a quartz single crystal using a microdrill (Dremel).

The presence of metal pieces especially in the samples ground in the hand mortar or milling jar as a result of gentle scrapping from the jar/mortar using a spatula is possible. Detailed processes indicating the positions in the samples from where XRD powdered was extracted is shown in an XRD logfile (Appendix 2).

XRD measurements were then run either on XRD wafer (e.g., Crist and Calc2), with no glass holder for samples with enough material (e.g., Chalc and Qtz2) or with glass holder for samples that did not have enough material (e.g., OA\_Gre, OA\_Aus2, OA\_Eth, OCT1, OCT2, OCT3, OCT5, and Calc1). Samples were measured in an auto-repeat mode with a sample rotation rate of 30/min. The measurement angle was set at 2theta range of 6-80° while the sample scan increment was set at 0.012°.

After the completion of the measurements, the sample data results were imported into Excel, and diffractograms were plotted. Two theta angles were converted to lattice d-spacings using Bragg's Law. The main mineral peaks were visually identified and used in identifying the different mineral phases. The XRD analysis results were also compared to the existing published datasets. XRD analysis, therefore, was used to classify the different study samples before imaging.

### **3.5.1. Results correlation and validation**

The hyperspectral LWIR image analysis results were compared with the spectral analysis results from the SWIR dataset as well as FTIR-ATR sample analysis. Sample spectra from the calcite varieties and the opaline silica polymorphs from the SWIR datasets were both analyzed for feature differences and compared to the LWIR results. Unlike SWIR results, FTIR-ATR sampling was done for nearly all the study samples which were compared to the LWIR datasets. XRD results were specifically used to validate the results from the LWIR analysis as opposed to both SWIR and FTIR-ATR datasets. These XRD analysis results were compared to the existing published datasets.

The emissivity feature broadness and depths, as well as the broadness and magnitudes of the main peaks in the XRD diffractograms, were calculated for quantitative analysis. The LWIR feature broadness was determined the calculation of the full width at half maximum (FWHM) of the deep features. For XRD diffractograms, the FWHM and peak magnitudes of the main peaks were calculated using the Scherrer equation of calculating the crystallite sizes.

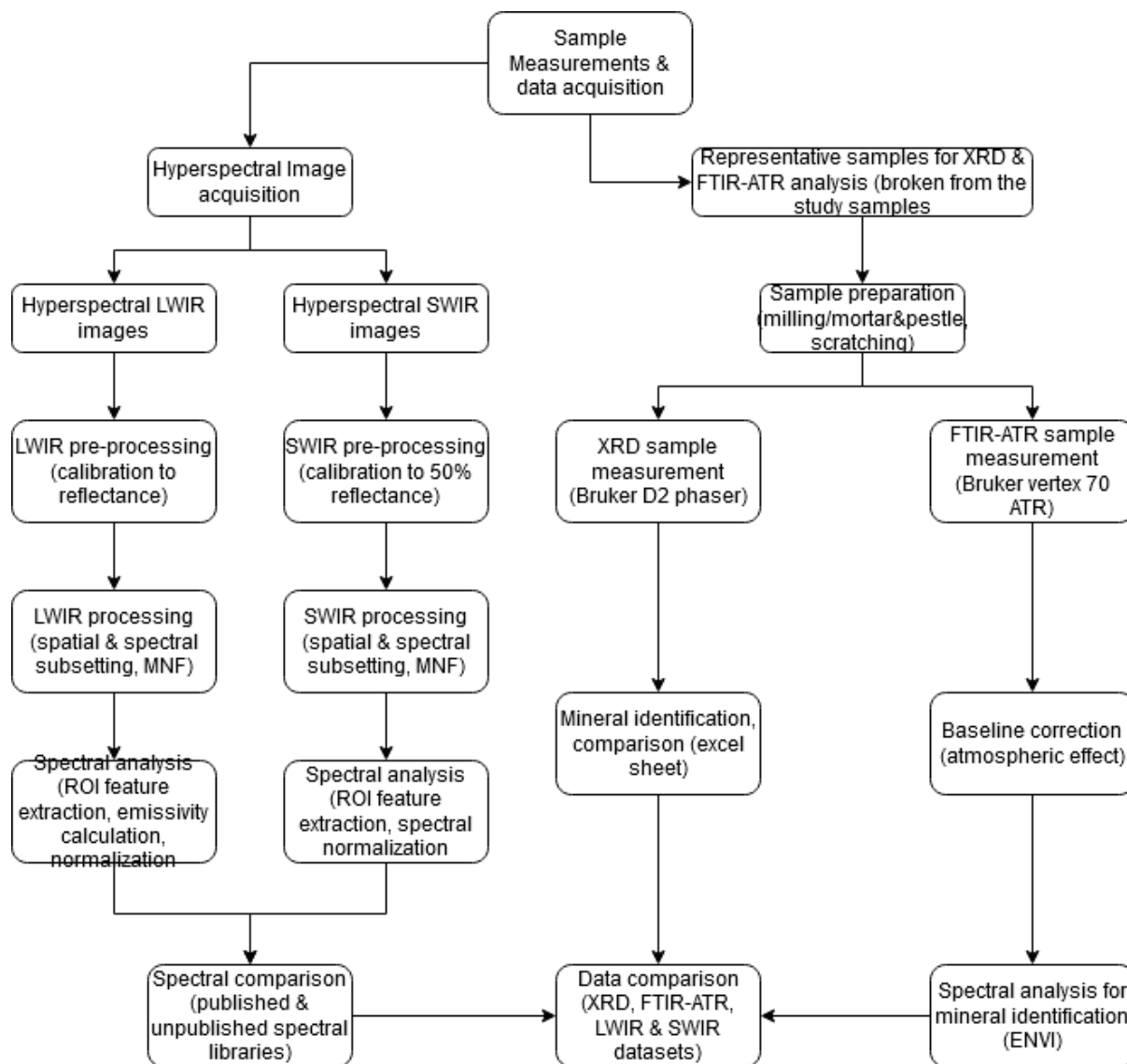


Figure 8: Flowchart summarizing the processes involved in data acquisition and analysis.

## 4. RESULTS

### 4.1. Image processing results

#### 4.1.1. MNF transform

Image processing steps applied to the acquired images helped in the noise reduction and in improving the quality of the sample spectral features. Figure 9 (a) shows a spectrum from an image of Qtz1 before MNF transform and (b) after the MNF transform showing a more improved clear spectral features as observed in the main absorption feature near  $\sim 9000$  nm and the absorption stretching between  $\sim 10000$ - $12000$  nm.

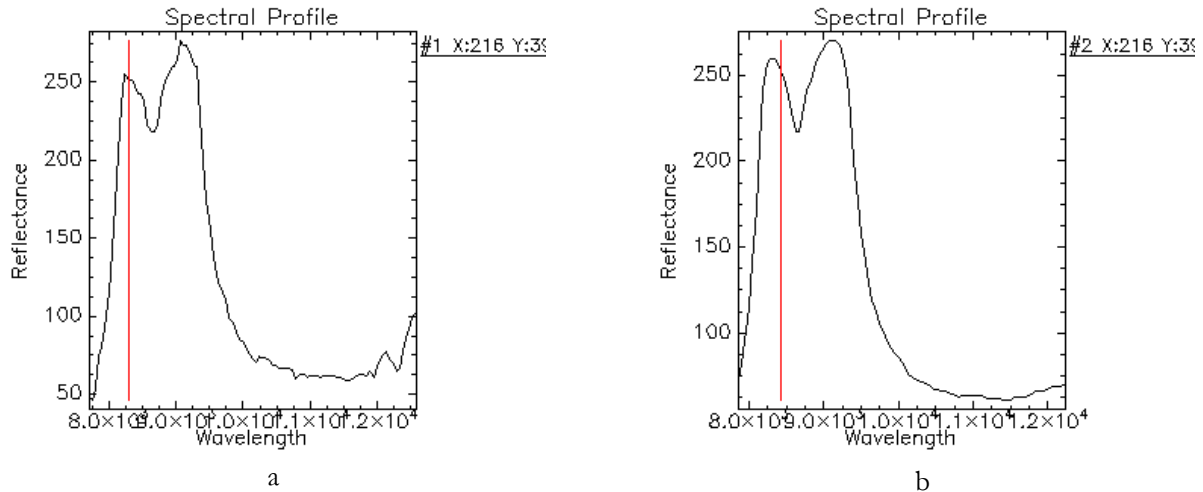


Figure 9: Image spectrum from Qtz1 sample before processing (a) and after applying MNF processing (b)

#### 4.1.2. Spectral feature extraction from ROIs

A comparison between a single pixel-based emissivity spectrum and the averaged spectrum from several pixels within the created ROI has shown improved spectral quality (Figure 10). The green spectrum (averaged spectrum from ROI) appears smoother than the red spectrum (single spectrum).

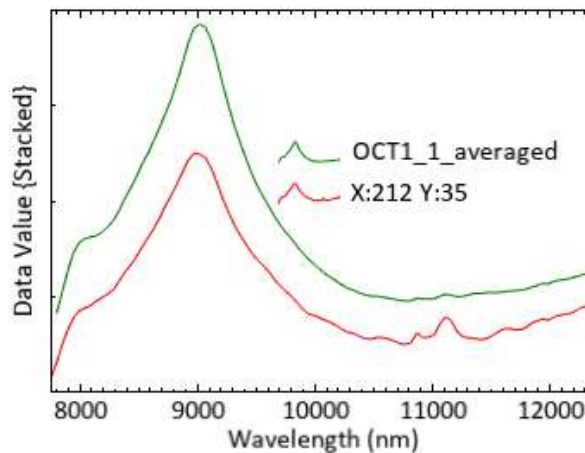


Figure 10: Comparison of image single-pixel emissivity spectrum and averaged ROI-based pixels' emissivity spectrum

#### 4.1.3. Spectral normalization

Differences in the emissivity scale values for the different minerals (both study samples and spectral libraries) were observed to have a negative effect on the overall spectral contrast when the different spectra are compared. However, from the normalized spectra, the spectral contrast of the different

sample spectra is maintained and easily compared. Figure 11 shows a comparison of absorption features of Qtz1 and Crist before continuum removal (A), after continuum removal (B), and the stacked plots of the continuum removed spectra (C) demonstrating the effects of different emissivity values on spectral contrast. The Crist\_1 features disappear in comparison to Qtz1\_1 probably due to the different emissivity values during image acquisition.

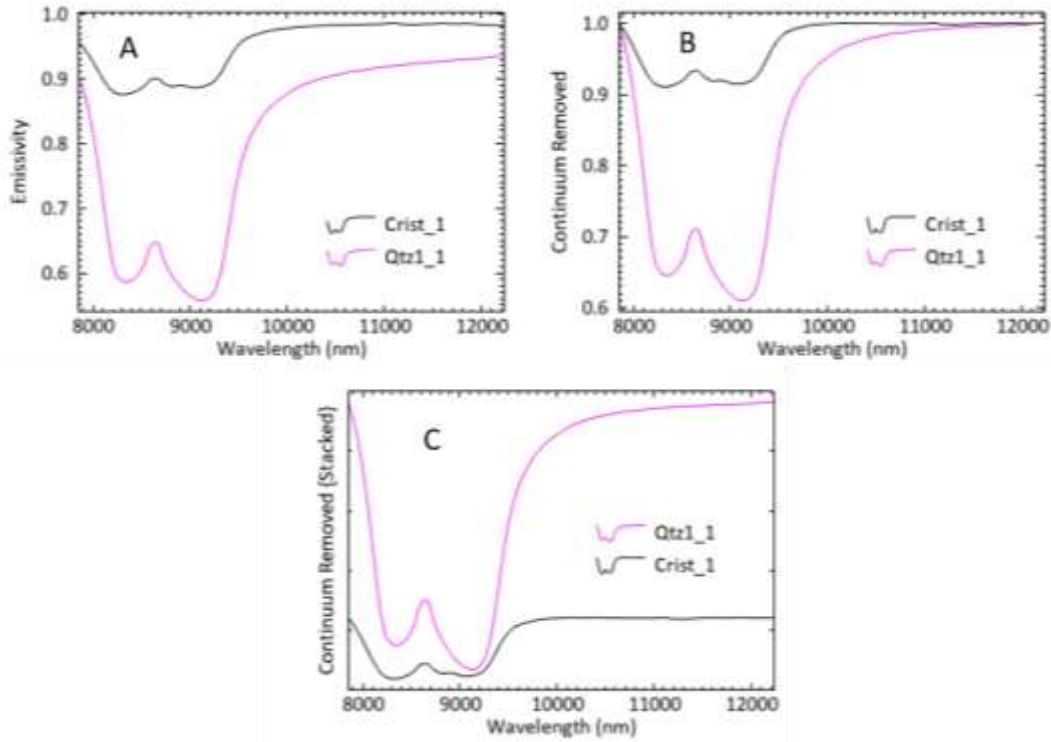


Figure 11: An example of spectra compared without continuum removal (A), when continuum removed (B) and the stacked plots of the continuum removed (C)

After the spectral normalization, the spectral contrast of the individual minerals is maintained for easier comparison (Figure 12).

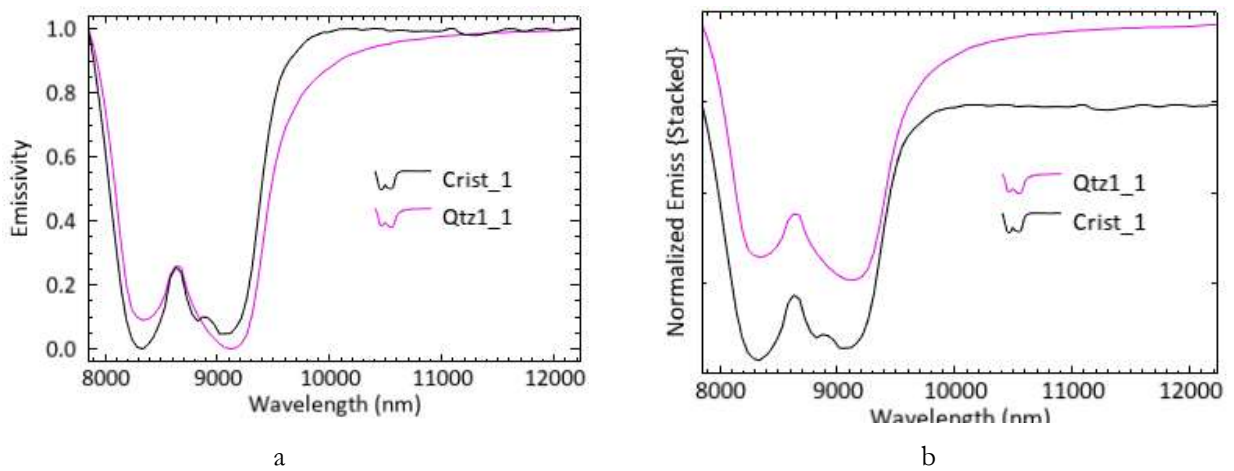


Figure 12: Appearance of spectral features after spectral normalization, unstacked spectra (a), and stacked spectra (b).



## 4.2. XRD analysis

XRD diffractograms were plotted for the different silica polymorphs and calcite varieties for comparison and identification of the individual minerals. From the results, different distinct intensity peak positions have been observed from the different study samples. The XRD diffractograms that were acquired show that some of the mineral samples (OA\_Eth and OA\_Gre) were wrongly classified based on the accompanying documentation. The diffractograms were plotted in d-spacing and not 2theta for easier comparison with the published data and opal classification criteria from Curtis et al., (2019), which are presented in d-spacing.

### 4.2.1. Silica series

XRD diffractograms analysis show quartz and chalcedony both have their intensity peaks at  $\sim 3.34$  Å,  $\sim 4.25/4.30$  Å,  $1.81$  Å,  $1.53$  Å,  $2.28$  Å,  $2.45$  Å, and  $2.94$  Å (Figure 14). The two minerals are noted to have different peak values near  $\sim 4.25$  Å for chalcedony while quartz has a  $\sim 4.30$  Å intensity peak. Quartz generally has sharp intensity peaks compared to chalcedony which is slightly broader peaks. The peaks are similar to those observed by Awadh and Yaseen, (2019), and Curtis et al., (2019). The cristobalite diffractogram has main intensity peaks similar to the quartz peaks especially near  $\sim 3.34$  Å and  $\sim 4.24$  Å. A broad intensity peak centered near  $\sim 6.87$  Å is noted in the cristobalite diffractogram but is missing in both quartz and chalcedony diffractograms (Figure 14). Other cristobalite peaks observed include  $\sim 3.03$  Å,  $\sim 2.45$  Å,  $2.12$  Å,  $1.81$  Å, and  $2.03$  Å (Figure 13 and Appendix 7). Tridymite, (silicic acid synthesized to  $1000^{\circ}\text{C}$ ) shows a broad intensity peak near  $\sim 4.09$  Å (Figure 14) and  $\sim 2.50$  Å (). The observed tridymite peaks differ by  $0.01$  Å to the distinct tridymite peaks of  $\sim 4.10$  Å and  $\sim 2.51$  Å as observed in Curtis et al., (2019).

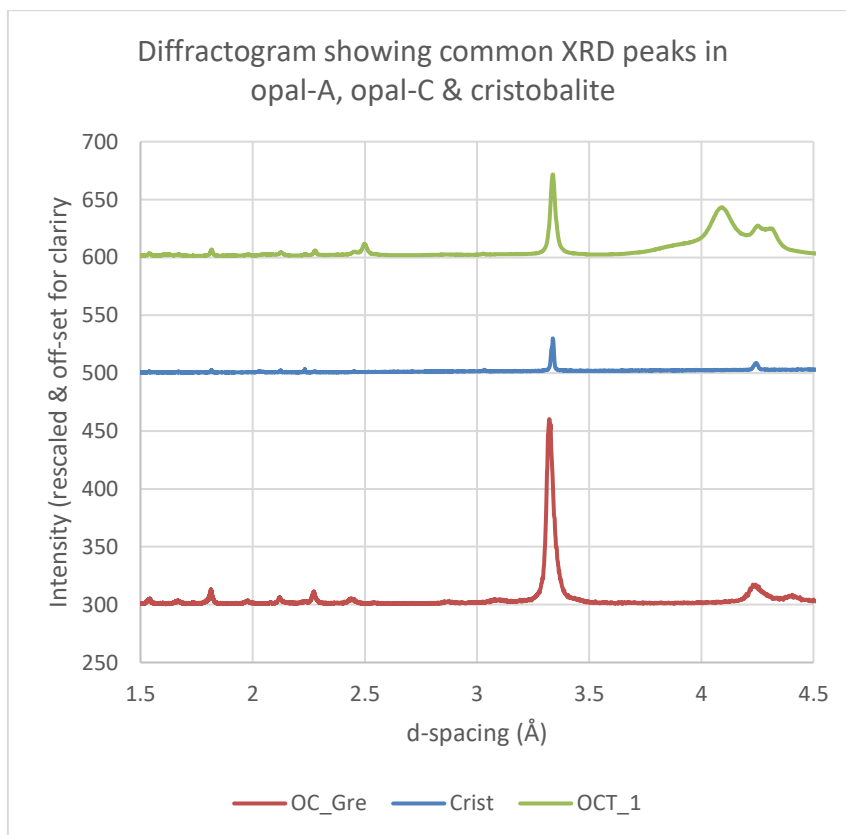


Figure 13: XRD diffractograms of Crist sample showing peaks matching opal-C and opal-CT peaks confirming its mineralogy (cristobalite). Quartz peaks also present

### XRD diffractogram peaks showing differences between the crystalline silica series

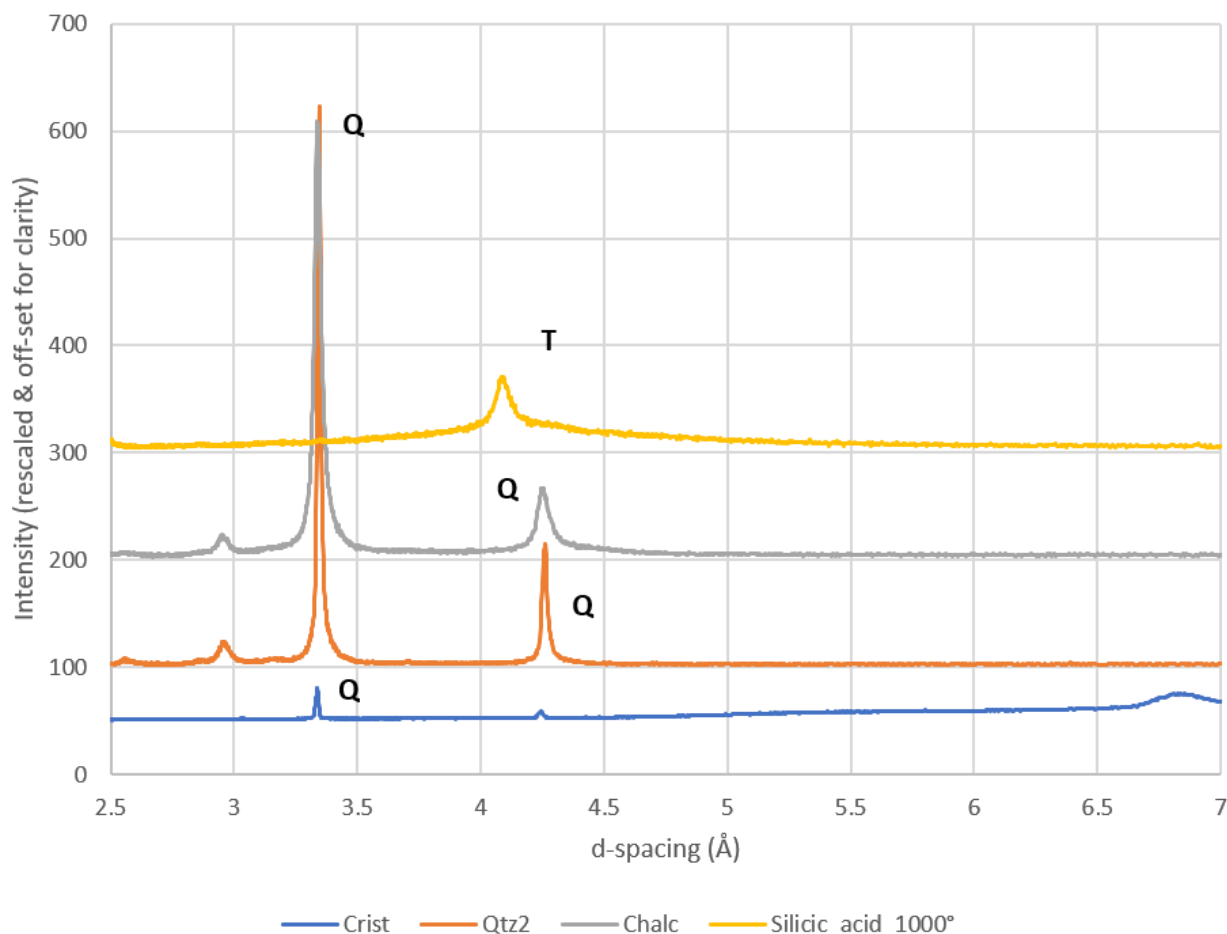


Figure 14: XRD diffractograms of the crystalline silica series (cristobalite, quartz, chalcedony, & the synthesized tridymite sample)

#### 4.2.2. Opaline silica diffractograms

XRD analysis was carried out for all the opaline silica samples except for the OCT4 and OA\_Aus1 samples. The results show that opal-A samples (OA\_Eth and OA\_Gre) were wrongly labeled as opal-A samples. Instead, the XRD diffractograms show peaks indicative of opal-CT for OA\_Eth and opal-C for OA\_Gre respectively (Figure 15). From FTIR-ATR results, both OA\_Eth and OA\_Gre samples have different absorbance spectra to that of the opal-A spectrum as observed in the OA\_Aus2 sample further suggesting that the OA\_Eth and OA\_Gre are not opal-A minerals. **Therefore, based on both XRD and FTIR-ATR results, OA\_Eth and OA\_Gre have been renamed as OCT\_Eth (opal-CT) and OC\_Gre (opal-C) respectively (Figure 15).**

OA\_Aus2 sample has a **slightly broad intensity peak near  $\sim 4.18$  Å** and sharp peaks at  $\sim 3.34$  Å (quartz peak) and  $2.45$  Å (Figure 15). More intensity peaks for the OA\_Aus2 sample are shown in the diffractogram provided in Appendix 6. The sample OCT\_Eth diffractogram intensity peaks are recorded near  $\sim 2.51$  Å and  $\sim 4.10$  Å with a **shorter peak on the right shoulder at  $\sim 4.29$**  and respectively. These intensity peaks ( $\sim 4.10$  Å and  $2.51$  Å) are similar to the observations made from the opal-CT samples' diffractograms (see Figure 15). It is noted that all the opal-CT samples all have a broad peak at  $\sim 4.10$  Å. Additionally, a shoulder shorter peak is also evident on the right of the broad peak ( $\sim 4.10$  Å) of some of

the opal-CT samples at  $\sim 4.25 \text{ \AA}$  as noted in OCT1, OCT2, and OCT\_Eth samples (Figure 15). This shows that the degree of the cristobalite-tridymite stacking may vary from one opal-CT sample to another. Curtis et al., (2019) notes the occurrence of the shorter peak on the shoulder of the  $4.10 \text{ \AA}$  peak makes such opal-CT minerals complex compared to those without the shorter peak which appear simple. The opal-CT samples OCT5, OCT3, and OCT6 do not show the shorter peak value to the right of the  $4.10 \text{ \AA}$ . OCT6 sample is noted to have a weaker peak near  $\sim 2.98 \text{ \AA}$  which is a tridymite peak. Sample OC\_Gre displayed intensity peaks near  $\sim 2.27 \text{ \AA}$ ,  $\sim 2.12 \text{ \AA}$ ,  $\sim 3.34 \text{ \AA}$  and  $\sim 4.25 \text{ \AA}$ . Most of the peaks have also been noted in quartz samples such as the diagnostic  $\sim 3.34 \text{ \AA}$ . The peak at  $\sim 4.28 \text{ \AA}$  is a diagnostic opal-C peak with a shorter peak on the right shoulder near  $\sim 4.40 \text{ \AA}$  (see below). A sharp quart peak near  $3.34 \text{ \AA}$  is also displayed by OC\_Gre and OCT1 but the peak is not noticed in the other opal-CT samples.

The peak at  $\sim 4.10 \text{ \AA}$  in the opaline silica series is noted to decrease in broadness (e.g., becoming sharp) from Opal-A, opal-CT, and Opal-C respectively an indication of increasing crystallinity.

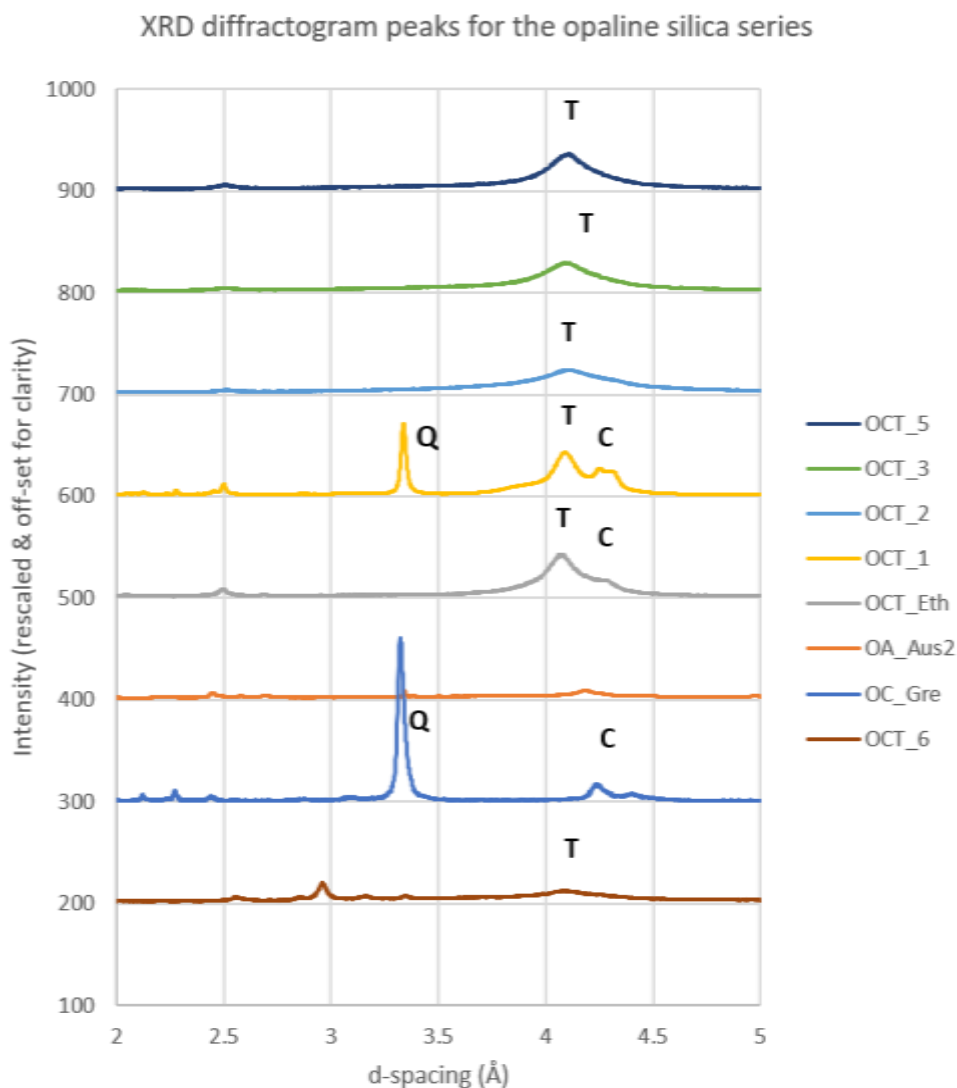


Figure 15: XRD diffractograms of the different opaline silica series (opal-A, opal-C & opal-CT samples). Q, T, and C represent quartz, tridymite & cristobalite peaks respectively.

#### 4.2.3. XRD peaks comparison of opal-C to chalcedony and quartz

XRD diffractograms of OC\_Gre (opal-C), quartz, and chalcedony diffractograms were compared to demonstrate the differences observed in their peaks. OC\_Gre sample shows the characteristic opal-C peak near  $\sim 4.28 \text{ \AA}$  (pointed by an arrow in Figure 16) that is not observed in quartz and chalcedony.

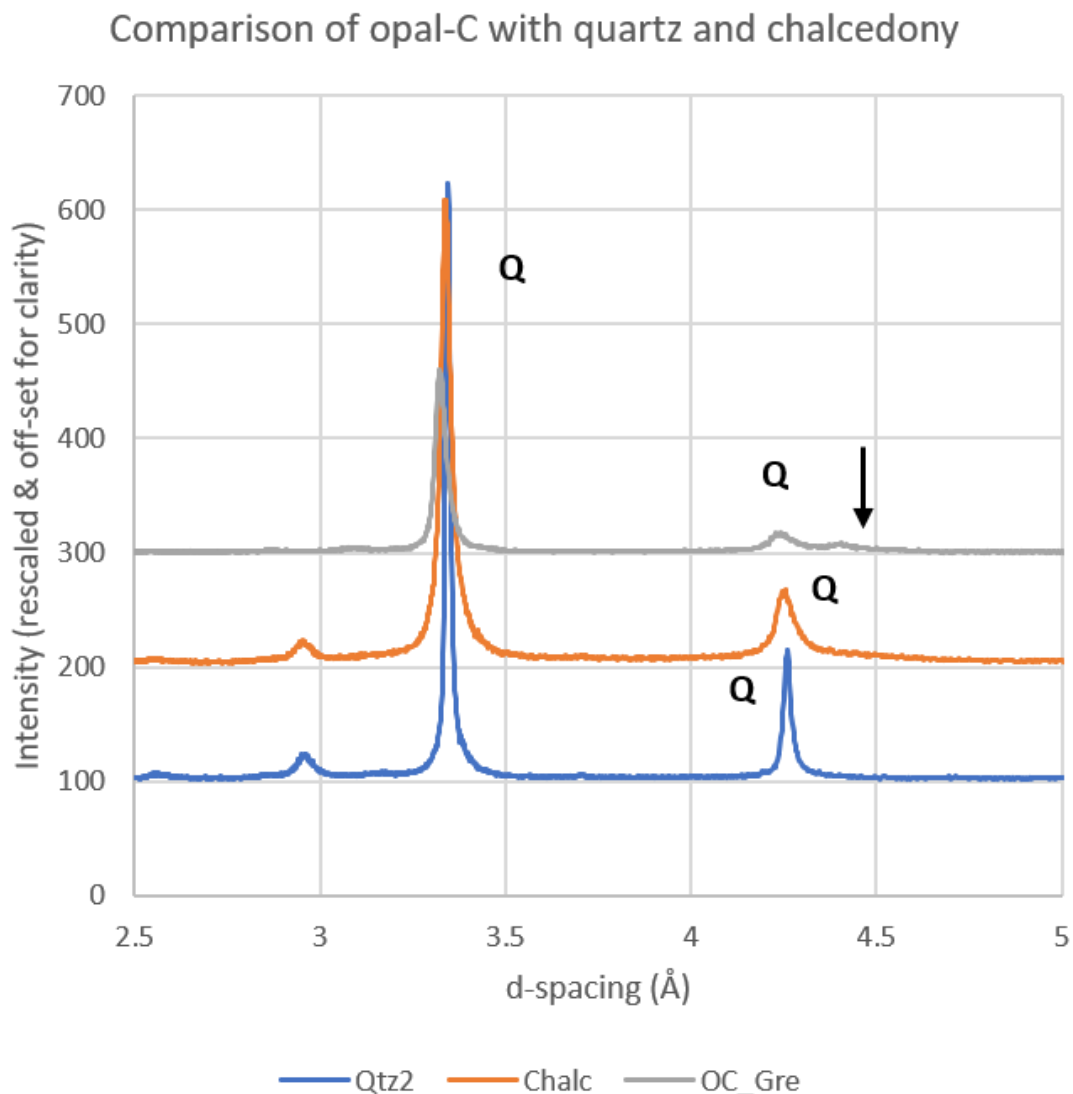


Figure 16: Diffractograms showing differences between opal-C, chalcedony, and quartz

#### 4.2.4. Calcite diffractograms

The XRD diffractograms for calcite samples show that all the calcite samples have their main intensity peaks at the same positions although they have different magnitudes and broadness. These peaks are recorded near  $\sim 3.02 \text{ \AA}$  (C4),  $\sim 2.09 \text{ \AA}$  (C1),  $\sim 2.28 \text{ \AA}$  (C2), and  $\sim 2.49 \text{ \AA}$  (C3) respectively (see Figure 17). Calc1 and Calc2 calcite varieties have sharp intensity peaks compared to Bcalc sample which has broad poor-formed intensity peaks as seen at C1, C2, C3, and C4 peak positions (Figure 17).

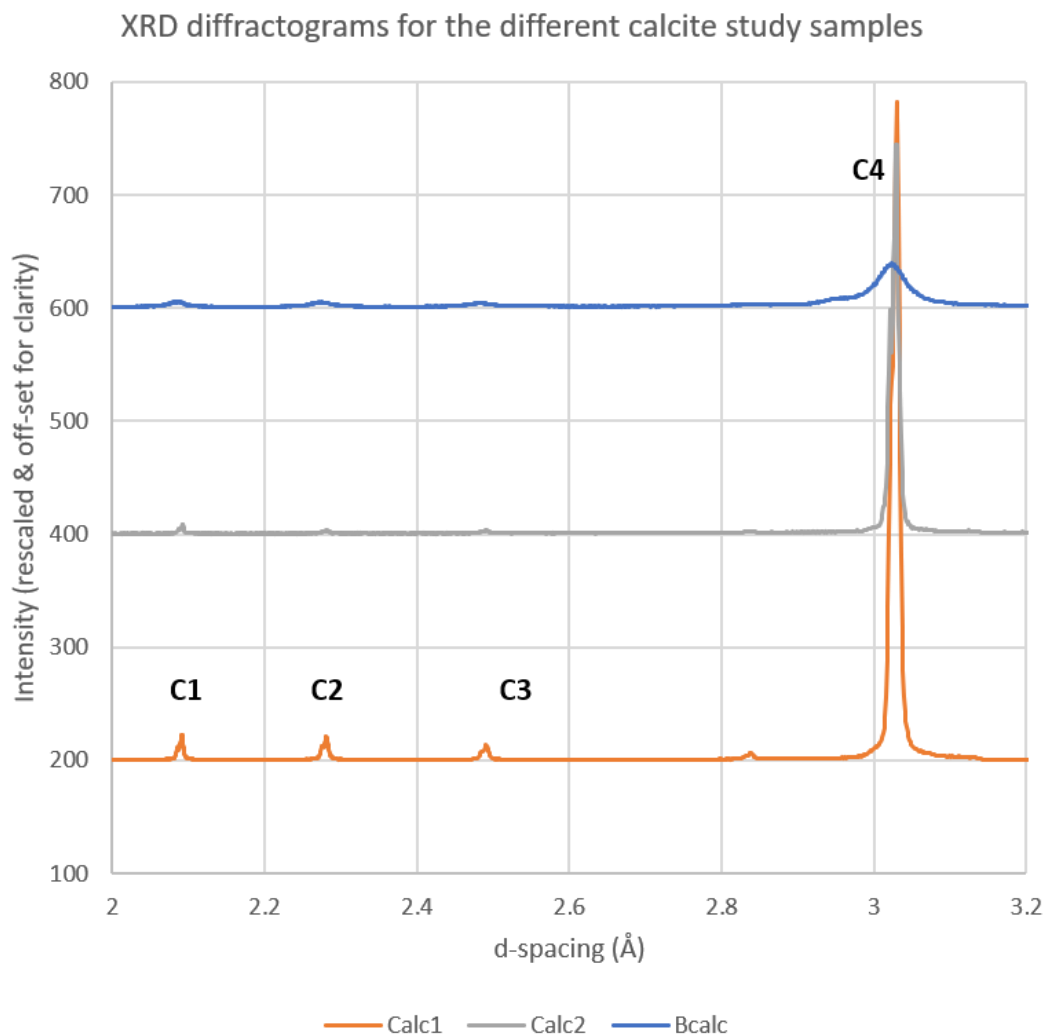


Figure 17: XRD diffractograms of calcite samples1 (Calc1), sample2 (Calc2), and bladed calcite (Bcalc) showing the main intensity peaks (C1, C2, C3, C4)

### 4.3. FTIR-ATR analysis

#### 4.3.1. Silica polymorphs

The FTIR-ATR results display the main absorbance features in all the crystalline silica samples quartz, chalcedony, and cristobalite to be similar in shape and wavelength positions. The main similar features are formed at 1060, 450, 780, and, 694  $\text{cm}^{-1}$  respectively (Figure 18a). The main absorption peak at 1060  $\text{cm}^{-1}$  is broad compared to the absorption peak near 450  $\text{cm}^{-1}$  in all the crystalline silica samples. All the crystalline silica samples are observed to have a doublet feature peak at **780  $\text{cm}^{-1}$** . However, chalcedony has an additional diagnostic absorbance feature at **555  $\text{cm}^{-1}$**  and **497  $\text{cm}^{-1}$**  (Figure 18a). The **555  $\text{cm}^{-1}$**  peaks are not observed in cristobalite and quartz samples while the **497  $\text{cm}^{-1}$**  peaks are noted at a longer wavelength near 505  $\text{cm}^{-1}$  in both cristobalite and quartz respectively (Figure 18a). The study quartz sample spectrum was compared to the published library spectrum from the Ruff project, (Figure 18a). The only observed difference between the quartz library spectrum and the quartz sample spectrum is the doublet feature peak in the library spectrum as opposed to the single feature spectrum for the quartz sample. The two distinct feature peaks noted in chalcedony had previously been observed by Schmidt and Fröhlich, (2011). **From the FTIR-ATR results, it appears the ‘Crist’ sample could be a quartz sample and not cristobalite.**

The opaline silica polymorphs have also displayed their main absorbance feature peaks near the same wavelength positions as observed in the crystalline silica polymorphs. Opal-A sample is noted to have a distinct appearance on the left shoulder of the **feature near 465 cm<sup>-1</sup>** when compared to the other opaline silica samples (Figure 18b). The opal-A sample feature appearance **at 465 cm<sup>-1</sup>** is identical to the one observed in the library spectrum. All the opal-CT samples have similar spectra with the main absorbance features forming near 1070, 465, and 784 cm<sup>-1</sup> respectively (Figure 18b). The opal-CT samples feature peaks at 1070 cm<sup>-1</sup> are broad compared to the 465 cm<sup>-1</sup> peaks. Minor shifts in wavelength positions (about ~15 cm<sup>-1</sup>) are also observed in the different opal-CT samples at the 1070 cm<sup>-1</sup> peaks. Apart from the main absorbance peaks noted in all the opaline silica polymorphs, the FTIR-ATR results also show additional peaks at **580 cm<sup>-1</sup>, 650 cm<sup>-1</sup>, and 1155 cm<sup>-1</sup>** in the OC\_Gre sample (see Figure 18b). These additional peaks are not seen in the opal-A and opal-CT samples. The distinct appearance noted in the opal-A sample (OA\_Aus2) is however not observed in the OCT\_Eth and OC\_Gre (previously classified as opal-A minerals) which agrees with the XRD results on the same.

The main feature difference between the crystalline silica (quartz, cristobalite, and chalcedony) and the opaline silica (opal-A, opal-CT, and opal-C) samples is the **doublet display of the crystalline silica absorbance feature peaks as opposed to the opaline silica single feature appearance at 784 cm<sup>-1</sup>**. The feature positions of the opaline silica are broad and shifted to the longer wavelength positions by approximately ~10 cm<sup>-1</sup> compared to the crystalline silica samples which are narrower (Figure 18).

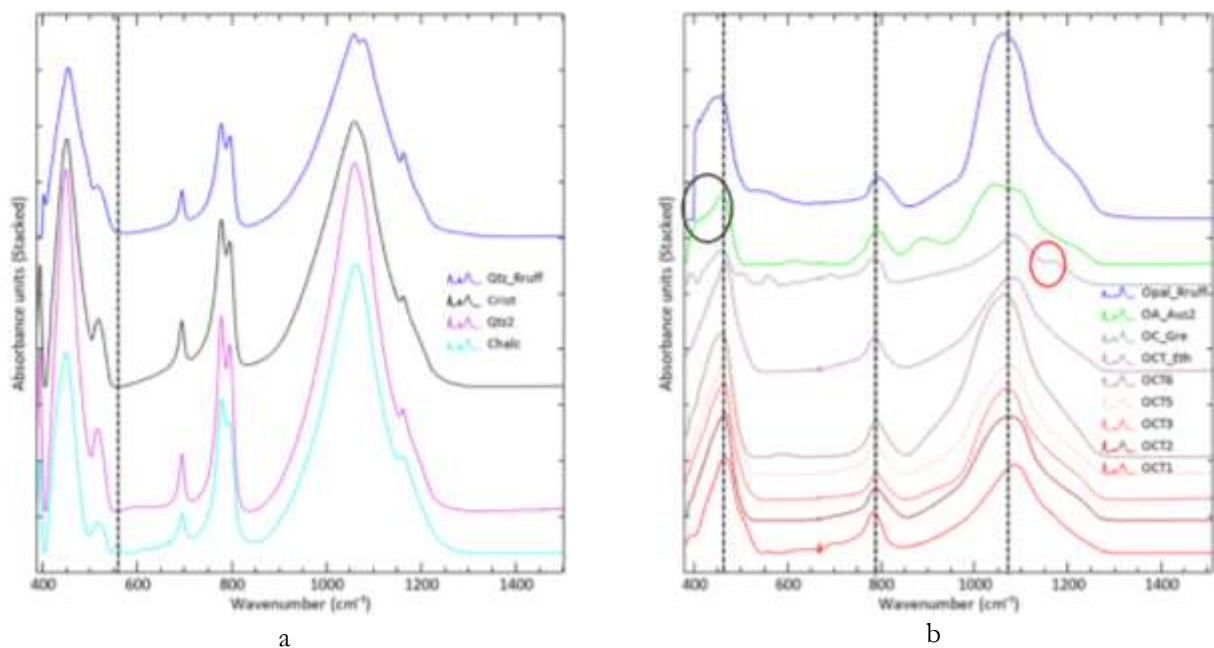


Figure 18: FTIR-ATR absorbance feature comparison of crystalline silica polymorphs (a) and opaline silica (b)

#### 4.3.2. Calcite varieties

The FTIR-ATR results for the three samples that were measured showed similar wavelength positions for the main absorbance features. A comparison of the spectra to the published datasets also concur with the observations made. The samples have their main peaks near ~1396, 1087, 871, and 712 cm<sup>-1</sup> respectively resulting from vibrational modes caused by carbonate ions (CO<sub>3</sub><sup>2-</sup>) stretch or bends. These are in agreement with observations by (Henry et al., 2017). No major difference is, however, observed from the study samples.

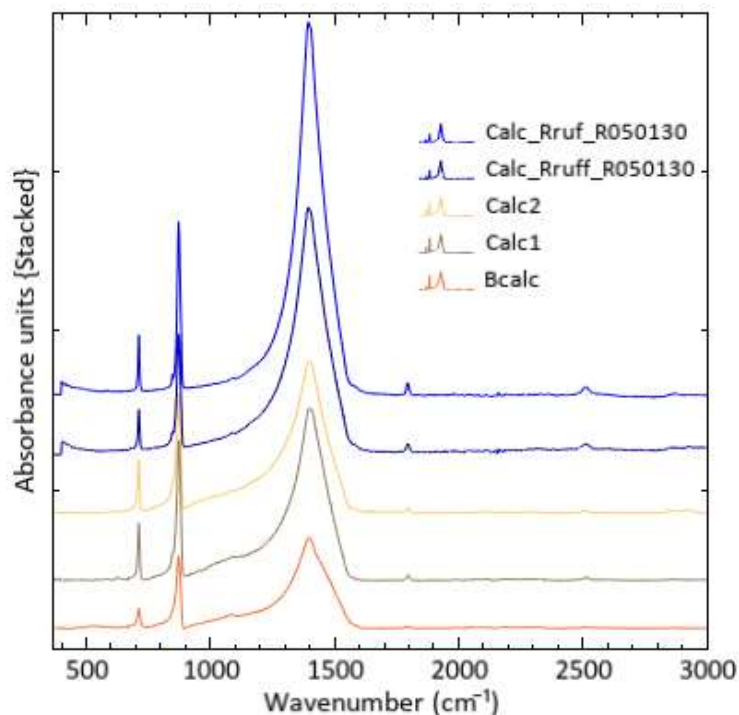


Figure 19: FTIR-ATR spectral comparison of the study calcite samples with varying magnitudes and width. Features compared with published data

#### 4.4. LWIR spectral features of silica polymorphs

Averaged sample spectra were extracted from each of the imaged study samples and their spectral features analyzed (e.g., for feature wavelength position, shape, and width). The spectra were continuum removed, normalized and spectra stacked for easy comparison. Study sample spectra were compared with various published standard spectral libraries such as US Geological Survey (USGS), Jet Propulsion Laboratory (JPL), the Arizona State University (ASU) and the CSIRO spectral libraries. Another unpublished single chalcedony spectrum acquired through personal communication was also used in the spectral comparison. Standard spectral library spectra are presented in blue colors in all the plots. The widths of some of the sample spectra were estimated from the feature's full width at half maximum (FWHM).

##### 4.4.1. Quartz

The emissivity spectra of imaged quartz samples have deepest and 2<sup>nd</sup> deepest emissivity minima near **~9100 nm** and **~8300 nm** respectively separated by a **diagnostic quartz emissivity peak of the Reststrahlen feature at ~8600 nm**. The ~9100 nm minimum is broader compared to the ~8300 nm minimum feature. The right shoulder of the deepest feature and left shoulder of the 2<sup>nd</sup> minimum feature is near vertical to the respective symmetry axis and longer than the opposite shoulders. The ascending right shoulder of the ~9100 nm has its peak near ~11000 nm. The FWHM of the quartz sample measures about **~550 nm** wide for the deepest feature and **~340 nm** for 2<sup>nd</sup> deepest feature. Quartz 1<sup>st</sup> and 2<sup>nd</sup> deepest features measure about **~0.32** and **~0.21** deep respectively.

Comparison with published library data (JPL & ASU) both confirm similarities in the feature shapes and wavelength positions. The diagnostic quartz emissivity peak near ~8600 nm appears sharp and narrow. The minima features are observed at ~9000 nm and ~8400 nm respectively indicating minor shifts (~100 nm) in wavelength positions. Also, the bases of the features in the samples are circular/smoothed compared to the library spectra. The quartz spectra are noted to differ from the other silica varieties

except chalcedony and cristobalite although cristobalite has an additional feature near  $\sim 8800$  nm (Figure 20a).

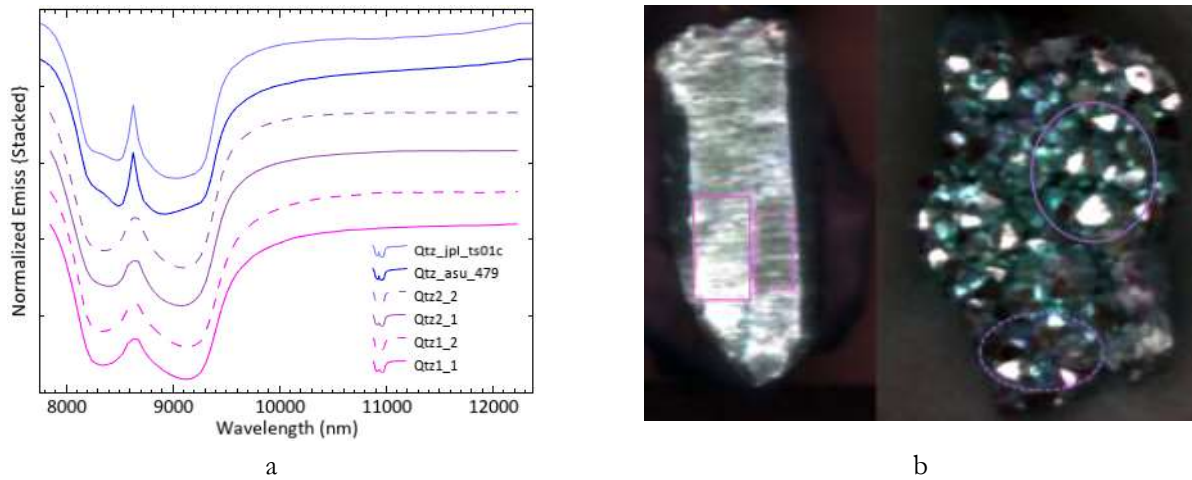


Figure 20: Stacked normalized sample spectra of Qtz1 and Qtz2 samples compared to JPL and ASU spectral libraries (a) and LWIR image in RGB (R $\sim$ 38, G $\sim$ 29, B $\sim$ 13) with ROIs where the average spectra were extracted (b).

#### 4.4.2. Chalcedony

The emissivity spectrum of the chalcedony sample appears similar to that of the quartz sample (Figure 26a). The similarity is both in shape and wavelength position of the diagnostic features. Just like in quartz, the minima features appear near  $\sim 9100$  nm (deepest) and  $\sim 8300$  nm respectively separated by an emissivity peak near  $\sim 8600$  nm. The deepest feature depth is approximately  $\sim 0.43$  while the 2<sup>nd</sup> deepest is about  $\sim 0.16$ .

The comparison with the standard library spectrum shows very distinct differences in terms of their emissivity spectral shapes. The USGS library spectrum has a sharp symmetric emissivity minimum near  $\sim 8100$  nm and a broad emissivity trough stretching from  $\sim 9600$  nm to  $\sim 12000$  nm which is not observed in the study sample. A small shallow emissivity minimum is also present at  $\sim 9300$  nm with the left shoulder longer than the right shoulder. It also has an emissivity peak at  $\sim 8600$  nm. The metadata indicates that the library sample measurement was done on a powdered sample of chalcedony, unlike the study sample. The library spectrum's shape could be attributed to the fine-powder form from which the observed library spectrum was obtained.

In addition to the standard library spectrum, the study sample spectra were also compared with a single spectrum acquired through personal communication from prof. Steven Ruff (Arizona State University). The spectrum of prof. Ruff sample has relatively sharp features compared to the chalcedony study sample. (Figure 21a). The chalcedony sample spectrum is noted to be similar to the quartz sample spectrum but differs from the other silica polymorphs studied.

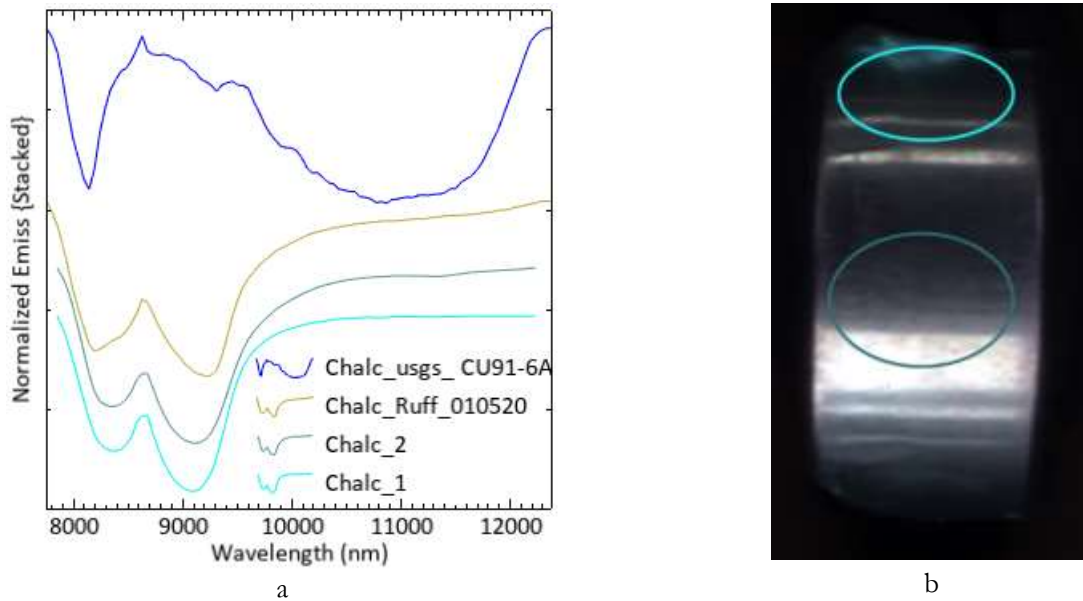


Figure 21: Chalc sample spectra compared with the published USGS library spectrum and a single chalcedony spectrum obtained from prof. Steven Ruff (Arizona State University) in (a) and an RGB image (bands 38, 29 & 13) with ROIs (b).

#### 4.4.3. Tridymite

Tridymite emissivity spectra are characterized by the broad emissivity minima doublet features observed within  $\sim 7800$  nm and  $\sim 10000$  nm emissivity peaks. The deepest emissivity features are observed near  $\sim 9000$  nm and  $\sim 8200$  nm separated by a local emissivity **peak at  $\sim 8300$  nm** respectively. Poorly-formed local emissivity on the left shoulder of the main emissivity feature is noted at  $\sim 8500$  nm and  $\sim 8800$  nm wavelength positions. The right shoulder of the deepest feature is steeper compared to the left shoulder of the same feature. The deepest feature is broad as opposed to the feature at  $\sim 8200$  nm. The deepest emissivity FWHM measures about  $\sim 633$  nm and  $0.63$  nm deep.

The corresponding library spectrum from the ASU spectral library shows the main features at  $\sim 9000$  nm and  $\sim 8000$  nm respectively for the deepest and 2<sup>nd</sup> deepest features separated with an emissivity **peak near  $\sim 8200$  nm**. Local emissivity minima are positioned at  $\sim 8600$  nm and  $\sim 8800$  nm. The deepest emissivity minimum is broad and appears relatively flat at the base compared to the narrower spectrum shape of the study sample. The library spectrum secondary minor emissivity minima are poorly-formed just as noted in the sample spectrum (Figure 22).

Apart from the shape and position of the 2<sup>nd</sup> deepest feature differences, tridymite and cristobalite differ in their main emissivity peaks too. In comparison with Opal-A, it does not have a clear feature at  $\sim 11500$  nm as well as having the local emissivity minima on the right shoulder of the main feature observed in Opal-A.

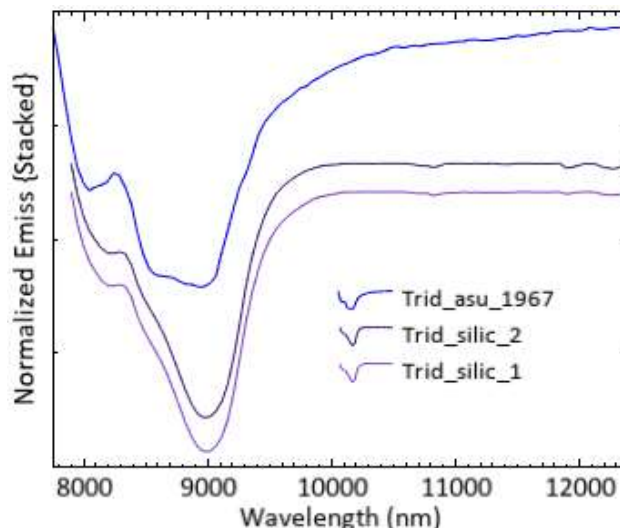


Figure 22: Emissivity spectra of silicic-acid synthesized tridymite powder sample and an ASU spectral library spectrum. Dotted lines indicating positions of the main emissivity minima

#### 4.4.4. Cristobalite

Cristobalite is observed to have its emissivity features at  $\sim 9000$  nm and  $\sim 8300$  nm separated by an emissivity peak at  $\sim 8600$  nm. A secondary emissivity feature near  $\sim 8800$  nm separated from the  $\sim 9000$  nm feature by a small hump-like local emissivity peak at  $\sim 8900$  nm is noted within the diagnostic Si-O absorption stretch. The second feature is relatively narrower compared to the first feature, (Figure 23). Apart from the secondary feature noted near  $\sim 8800$  nm, this cristobalite sample spectrum resembles the spectra of the studied quartz (Figure 20).

The library spectrum of cristobalite is characterized by sharp, narrow absorption features and peaks with minor shifts in the wavelength positions compared to the study sample. The library sample features are formed near  $\sim 9100$  nm and  $8200$  nm with emissivity peak at  $\sim 8400$  nm. Secondary emissivity features are formed near  $\sim 8800$  nm and  $\sim 8500$  nm wavelength positions whereas only  $\sim 8800$  nm feature is noticed in the study sample. The library cristobalite absorption features' shapes appear different from the observed sample spectrum feature shapes (Figure 23). Minor shifts of  $\pm \sim 100$  nm and  $\sim 200$  nm are observed in the sample spectrum's main absorption features and emissivity peak respectively compared to the library spectra.

Cristobalite study sample spectrum appears different from all other silica polymorphs but nearly resembles the quartz sample spectrum. Significantly, the 2<sup>nd</sup> deepest feature is noted to be well-formed in the cristobalite sample at a longer wavelength position (minor shift of  $\sim 100$  nm) compared to the shallow and broad feature in tridymite.

The LWIR spectrum of the study cristobalite together with the XRD and FTIR-ATR observations all tend to suggest that the 'Crist' study sample could be a quartz mineral and not cristobalite. The Crist sample has a typical quartz FTIR-ATR spectrum signature and its XRD diffractogram is dominated by the quartz peak values. The only cristobalite-like feature is noted in the LWIR spectrum is the secondary emissivity feature at  $\sim 8800$  nm while the main features resemble quartz.

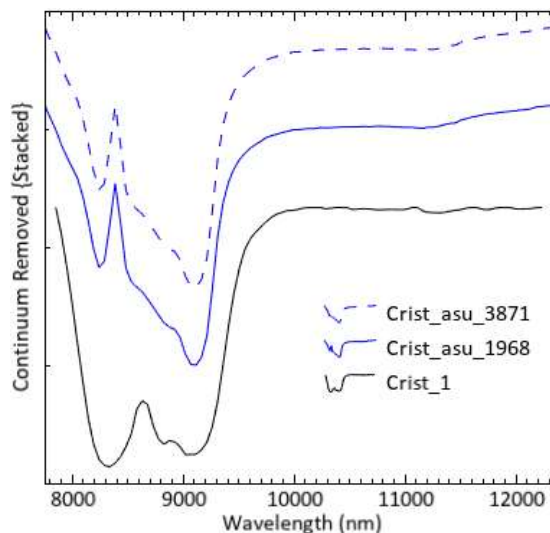


Figure 23: Spectral features of cristobalite sample measured compared to the cristobalite spectra from the ASU spectral library

#### 4.4.5. Opal-A

Opal-A shows Si-O stretching absorption between  $\sim 7700$  nm and  $\sim 10520$  nm. Emissivity spectral feature observations indicate that opal-A have three distinct emissivity minima features at  $\sim 9000$  nm,  $\sim 11500$  nm, and  $\sim 8000$  nm respectively. The deepest feature ( $\sim 9000$  nm), has emissivity peaks near  $\sim 8300$  nm (shorter) on the left shoulder and at  $\sim 10700$  nm (longer) on the right shoulder. The left shoulder is steeper compared to the right shoulder which is gradually diverging away from the symmetry axis. Minor local emissivity minima are observed on the right shoulder of the  $\sim 9000$  nm minimum feature at  $\sim 9500$  nm and  $\sim 10000$  nm respectively. The second emissivity minimum feature ( $\sim 8000$  nm) is bounded by emissivity peaks at  $\sim 8300$  nm on the right shoulder near  $\sim 7800$  nm. Opal-A has its local emissivity minima features on the right shoulder of the main emissivity feature as opposed to both tridymite and cristobalite. The feature near  $\sim 11500$  nm is a characteristic opal-A emissivity feature that is not observed in both tridymite and cristobalite samples.

The opal-A library spectrum shows deepest and 2<sup>nd</sup> deepest emissivity features at  $\sim 8900$  nm and  $\sim 7900$  nm separated by emissivity peak at  $\sim 8300$  nm and secondary features at  $\sim 10100$  nm and  $\sim 11400$  nm respectively. This represents a minor shift of  $\sim 100$  nm to the shorter wavelength compared to the study sample spectrum. These features are clear in the USGS library spectrum. The secondary features are poorly formed in the ASU library spectrum (Figure 24).

The secondary features noted in the opal-A study samples form the most important difference between opal-A and the crystalline quartz, cristobalite, and tridymite in addition to spectral appears. Opal-A secondary features also show the difference from the opal-CT samples depending on the side of the deepest feature they form. For example, opal-A secondary features are formed to the longer wavelengths of the deepest feature while opal-CT secondary features occur to the shorter wavelengths (Figure 27b).

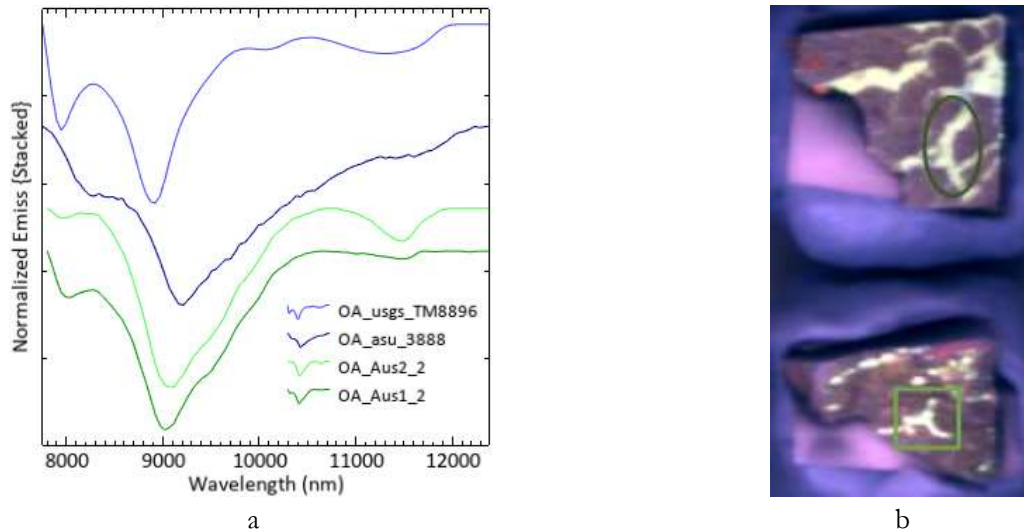


Figure 24: Spectra of opal-A samples (OA\_Aus1 & OA\_Aus2) compared with the standard USGS spectral library spectrum (left) and sample RGB image (38, 29, 13) showing ROIs locations of OA\_Aus1 (top) and OA\_Aus2 (below) (right).

#### 4.4.6. Opal-CT

Opal-CT has its main emissivity features within the **~7700 nm to ~8500 nm** stretch with minor local emissivity peaks as observed by Michalski et al., (2003). From the various opal-CT samples, the same is noted with the main emissivity minimum near **~9000 nm**. Minor local emissivity features are noted to form on the left shoulder of the main emissivity feature as opposed to the observations made in opal-A samples which are on the right shoulder. The **~9000 nm** feature broadens in shape in some Opal-CT samples likely due to increased crystallinity, (Michalski et al., 2003). The various opal-CT samples also have a near **~8000 nm** emissivity minima feature and minor local emissivity features on the left shoulder of the main emissivity feature. A broad emissivity peak occurs near **~8300 nm**. OCT3 spectra show the main emissivity feature near **~9000 nm** at a longer wavelength near **~9100 nm** compared to the other opal-CT samples as shown by the dashed line in Figure 25a. OCT2 sample is observed to have a minor shift of about **~100 nm** to the shorter wavelength position compared with the general opal-CT feature occurrences in the samples. This cannot be attributed to its color influence since OCT1 which is similar in color has a different wavelength position with it. The dashed lines (see below) shows the main emissivity minima features at **~9000 nm** and **~8000 nm**, one of the local emissivity minima and shift in wavelength position to the longer wavelength (shorter dashed line) in OCT3 sample.

The main features are observed at **~9000 nm** (deepest) and **~8000 nm** (2<sup>nd</sup> deepest feature) in the library spectrum. The poorly-firmed local emissivity features also noted on the shorter wavelength of the deepest feature just as observed in the study samples' spectra (Figure 25a).

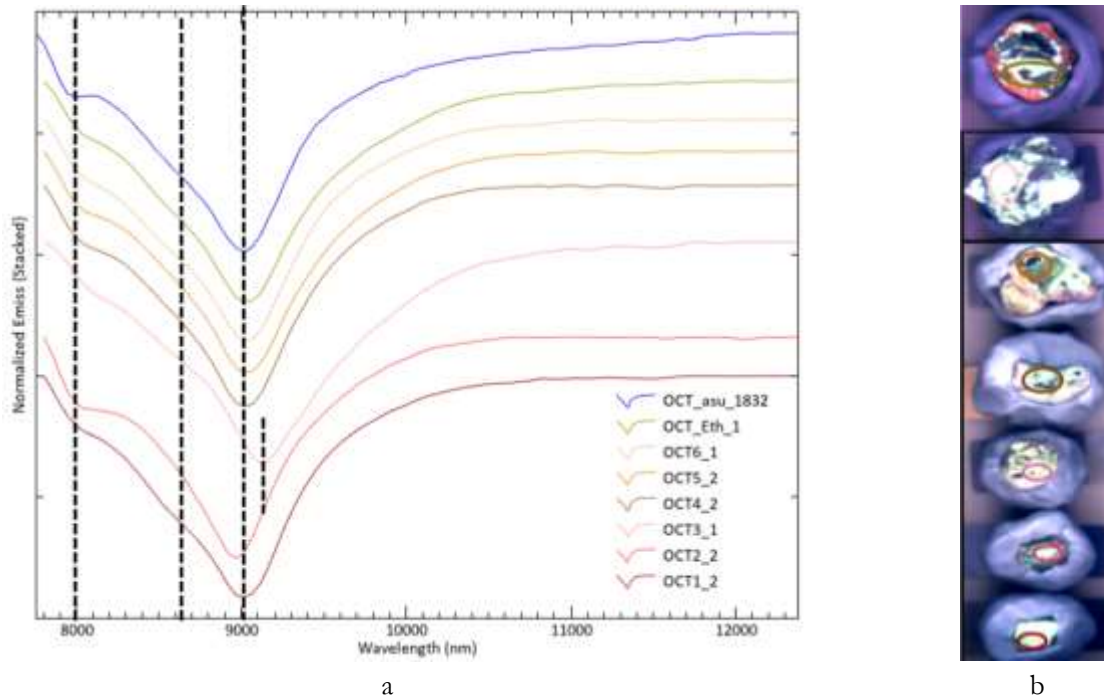


Figure 25: Spectral features of Opal-CT samples compared to ASU spectral library spectrum (a). RGB (38, 29, 13) of LWIR images (b) arranged top to bottom similar to the respective sample spectrum showing ROI. Dashed lines show feature positions

#### 4.4.7. Opal-C

This was initially classified as opal-A (OA\_Gre) but renamed reclassified as an opal-C (OC\_Gre) after the XRD and FTIR-ATR analyses. Two different spectra are observed. Both spectra have the main absorption feature at  $\sim 9300$  nm and emissivity peak at  $\sim 8600$  nm. The 2<sup>nd</sup> feature is noted at  $\sim 8400$  nm in OC\_Gre\_1 and  $\sim 8200$  nm in the OC\_Gre\_2 spectrum. Additionally, OC\_Gre\_2 shows secondary features near  $\sim 11200$  nm,  $\sim 10500$  nm,  $\sim 10000$  nm, and  $\sim 9000$  nm respectively. No opal-C library spectrum was available for comparison with the study sample spectrum. Nonetheless, sample spectra were compared to the only available library spectrum of opal-CT/C with characteristics of both opal-CT and opal-C and have its main peak at  $\sim 8200$  nm and main absorption feature at  $\sim 9000$  nm (Figure 26). The library sample is indicated as fine particles of between 2 mm and 125 microns in size.

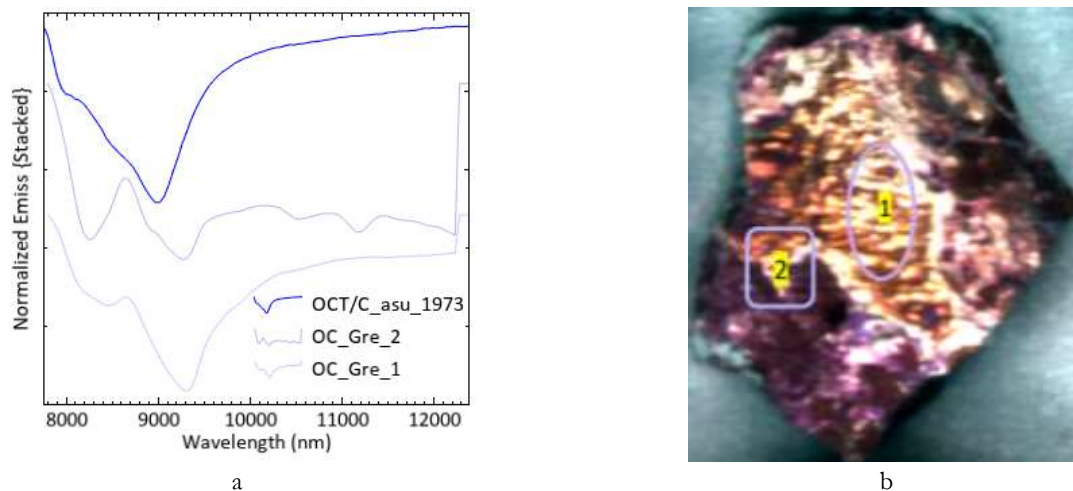


Figure 26: LWIR spectra of the opal-C sample compared to an ASU library spectrum (opal-CT/C) in (a) and RGB image showing ROI 1&2 locations for OC\_Gre\_1 and OC\_Gre\_2 spectra respectively (b)

#### 4.5. Spectral feature difference in the silica polymorphs

Both quartz and chalcedony have diagnostic absorption features at the same wavelength positions at  $\sim 9100$  nm and  $\sim 8300$  nm separated by emissivity peak at  $\sim 8600$  nm (Figure 27a). No major difference is noticed from their LWIR spectra. The absence of local emissivity minima has been seen as the main distinguishing feature between chalcedony/quartz and the other silica polymorphs studied. Tridymite has its main emissivity peak near  $\sim 8300$  nm whereas quartz, chalcedony, and cristobalite have their peak at  $\sim 8600$  nm. Tridymite's main emissivity minimum is at a shorter wavelength compared to cristobalite. Another distinct difference between tridymite and cristobalite is noted in the depths of the 2<sup>nd</sup> deepest absorption feature. The feature is deep and narrow symmetrical in cristobalite compared to the relatively shallow feature in tridymite with a very short right shoulder than the left shoulder.

Spectral feature differences were also observed in the different opaline silica polymorphs that can distinguish them from one another including the crystalline silica polymorphs. Generally, all opaline silica series have minor local emissivity features. To start with, opal-A is characterized by the occurrence of the local emissivity features at longer wavelengths than its deepest feature while opal-CT samples have their secondary emissivity features at shorter wavelengths of the deepest feature (Figure 27b). A distinct broad minimum feature is present at  $\sim 11500$  nm in the opal-A sample but missing in the opal-CT samples. Opal-A has a relatively deeper 2<sup>nd</sup> emissivity feature compared to opal-CT. Both opal-A and opal-CT have their main emissivity peak at  $\sim 8300$  nm although it is not well-formed in opal-CT samples (Figure 27b).

The LWIR spectrum of opal-C is observed to have its secondary emissivity features both at shorter and longer wavelengths of the deepest absorption feature. The spectral shape of the main emissivity features portrays the spectral feature appearance of chalcedony although it has the additional secondary features at longer wavelengths that were not observed in chalcedony spectra. The opal-C emissivity peak at  $\sim 8600$  nm is commonly noted in the crystalline silica series as opposed to the one recorded in the other opaline silica samples i.e.,  $\sim 8300$  nm (Figure 27b).

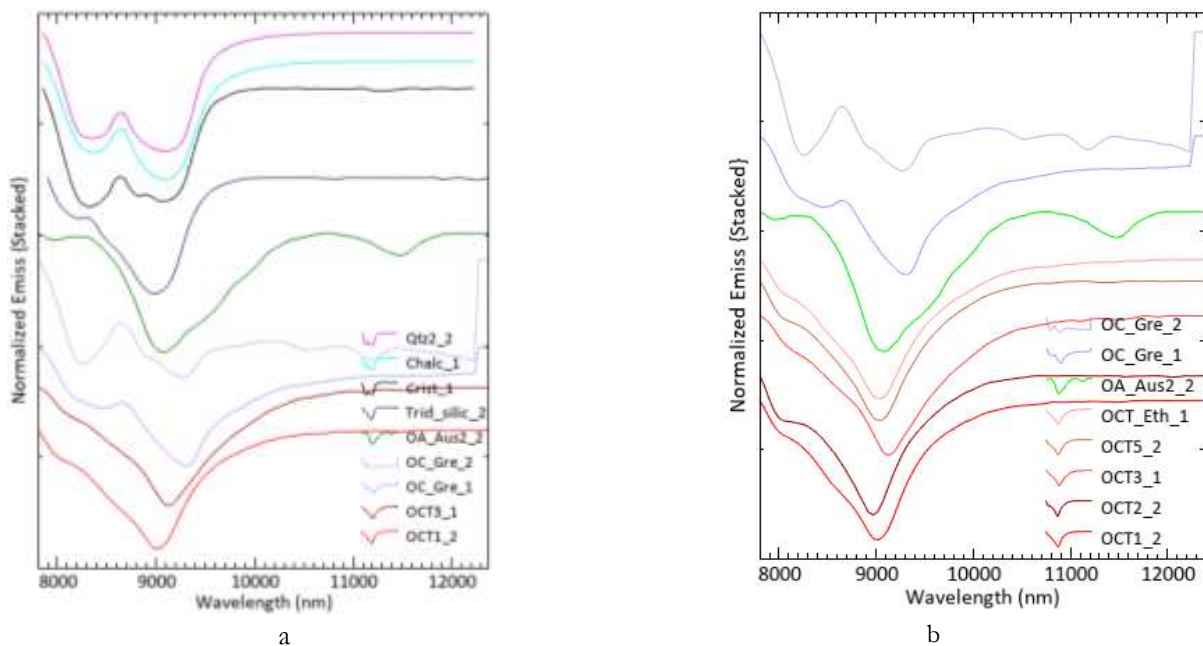


Figure 27: Plots (a) showing the spectral feature differences between the studied silica polymorphs while (b) shows differences between opaline silica series

#### 4.6. Spectral feature changes in silica polymorphs due to increase in crystallinity

The crystalline samples (e.g., quartz, chalcedony, cristobalite) have a broad main absorption feature compared to the opaline silica polymorphs. The 2<sup>nd</sup> deepest feature of the opaline silica generally is at shorter wavelengths (e.g., ranging ~8000 nm) as noted in opal-A and opal-CT spectra compared to the crystalline silica polymorphs (e.g., between ~8200-8300 nm) (Figure 27a). The local minor emissivity features also is an indicator of the changes in crystallinity. The secondary emissivity features are mostly observed in the opaline samples compared to the crystalline series. The FWHM values and the depths of the deepest emissivity feature also demonstrate the spectral feature changes with an increase in crystallinity as summarized in (Table 3).

#### 4.7. Effect of color on spectral features of opaline silica series

Spectral feature analysis of the different opal-CT samples shows little or no effect of sample color appearance. For example, OCT1 and OCT2 are both white have a minor difference of ~50 nm in their wavelength positions. The same is observed when different samples of different colors (OCT1~white and OCT3, OCT4, OCT5, OCT6, and OCT\_Eth in shades of orange) both show the same wavelength positions for the main emissivity features. Nearly all opal-CT samples have their major absorption features at the same wavelength positions except for OCT2 with a minor shift towards shorter wavelength and OCT3 with shifts to the longer wavelength. This also applies to the overall feature shapes except for OCT2 which appears to slightly narrow compared to the other samples. Thus, it can be concluded that color differences do not have much influence on the spectral features of the different opaline silica samples.

#### 4.8. Quantitative analysis of LWIR and XRD features (e.g., magnitude, depth and width) of silica polymorphs

The main deepest emissivity features of the study silica polymorphs were quantitatively compared. The feature FWHM and the depths of the deepest feature were determined for both crystalline and opaline silica samples whereas the 2<sup>nd</sup> deepest feature FWHM and depths could only be calculated for quartz, chalcedony, and cristobalite. Tridymite and the opaline silica rarely show a perfect-shape 2<sup>nd</sup> feature from which a feature FWHM and depth could be calculated compared to the crystalline samples (Figure 27a). The depth and FWHM of the deepest feature are observed to increase in size as the crystallinity reduces (Table 3). Cristobalite is shown to have the least FWHM of ~340 nm and depth of ~0.21 and quartz and chalcedony both with FWHM of ~550 nm but differ in depth at 0.32 and 0.43 respectively. The amorphous silica (opal-A) has the largest FWHM of ~880 nm and depth at 0.78 compared to the other silica polymorphs (Table 3). The XRD main peaks FWHM and magnitude, however, do not show consistency in the different silica polymorphs apart from quartz and chalcedony which have similar peaks (Table 4). Chalcedony is noted to have double the FWHM value of quartz while quartz has a higher peak magnitude than chalcedony from the three main peaks.

Table 3: Calculated FWHM and depths of the LWIR deepest spectral features for the silica polymorphs

Sample spectrum	FWHM of deepest features (~nm)		Feature depth	
	1 <sup>st</sup>	2 <sup>nd</sup>	1 <sup>st</sup>	2 <sup>nd</sup>
Qtz2_2	550	340	0.32	0.21
Chalc1	550	340	0.43	0.20
Crist	340	550	0.21	0.26
Trid	600	-	0.64	-
OA_Aus2	880	-	0.78	-
OCT1	730	-	0.71	-

Table 4: FWHM and magnitude of XRD main peaks for the silica polymorphs calculated using Scherrer equation

Sample	Position of main peaks			FWHM of the main peaks			Magnitudes of the main Peaks		
	1 <sup>st</sup>	2 <sup>nd</sup>	3 <sup>rd</sup>	1 <sup>st</sup>	2 <sup>nd</sup>	3 <sup>rd</sup>	1 <sup>st</sup>	2 <sup>nd</sup>	3 <sup>rd</sup>
Qtz2	3.34	4.25	1.81	0.02	0.03	0.01	470.0	101.2	39.0
Chalc	3.34	4.25	1.81	0.04	0.08	0.02	369.3	51.4	30.8
Crist	5.7	2.7	-	3.98	5.90	-	21.8	13.7	-
Trid	3.47	4.06	4.09	0.78	1.62	0.08	7.1	20.8	41.6
OA_Aus2	4.18	2.45	3.87	0.16	0.04	2.15	4.5	4.0	1.87
OCT1	3.33	4.08	4.29	0.03	0.24	0.12	65.3	32.4	19.0
OCT2	4.12	2.51	-	0.42	3.12	-	15.50	9.09	-
OCT3	4.10	2.94	-	0.35	3.01	-	21.0	4.44	-
OCT6	2.95	5.66	1.81	0.05	0.28	0.03	14.40	5.66	5.20
OCT_Eth	4.10	2.49	3.47	0.42	0.02	2.69	20.2	5.2	2.2
OC_Gre	3.32	4.24	1.81	0.03	0.06	0.02	124.8	11.2	10.1

#### 4.9. LWIR spectral features of calcite varieties

Small differences are observed in the emissivity spectra of the study calcite varieties. Calc1 sample has its main emissivity feature at **~11300 nm**. The sample also appears to form minor emissivity features on the left shoulder of the main emissivity. The feature is formed near **~10400 nm**. The right arm of the main emissivity feature appears steeper than the left (Figure 28a). Two distinct wavelength positions were registered from two spectra obtained from sample Calc2. The first spectrum, Calc2\_1 has its main feature at a longer wavelength near **~11350 nm** while the second spectrum Calc2\_2 displays the feature at a shorter wavelength position near **~11200 nm** (Figure 28a). The two Calc2 spectra are also different in shapes with Calc2\_1 showing a broad trough characteristic of quartz feature while the Calc2\_2 does not show the quartz feature. The right arm of the main feature of Calc2\_2 spectrum less steep with poorly formed secondary features including near **~12200 nm**. The bladed/platy calcite (Bcalc) recorded its emissivity feature at **~11250 nm** and also shows the presence of the quartz feature although it's poorly-formed. A broad secondary feature is noted at a longer wavelength at **~12400 nm** to the right of the main feature (Figure 28a). Comparison with the ASU library spectra shows minor shifts in wavelength positions of between **~50-100 nm** from the **~11300 nm** diagnostic feature. The library spectra also do not display the quartz feature.

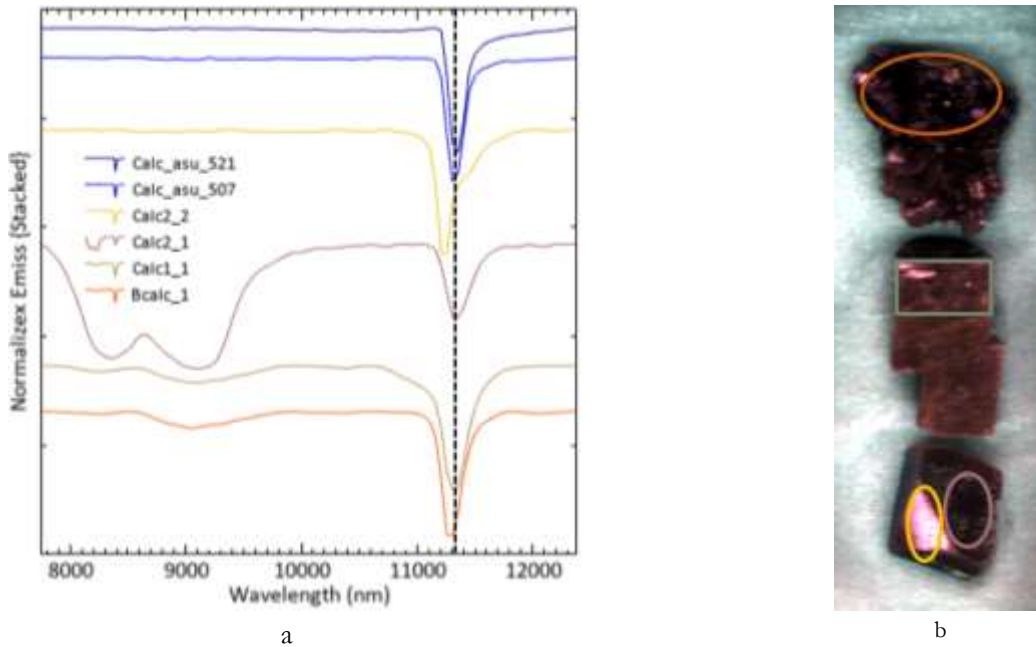


Figure 28: Sample spectra of calcite varieties matched with standard library spectra (fig. a) and RGB of the LWIR image with the ROI where the averaged spectra were extracted (fig. b)

#### 4.10. SWIR Image analysis results

##### 4.10.1. Calcite Varieties

The SWIR absorption features of the three calcite study samples' spectra are observed between  $\sim 2284\text{--}2340\text{ nm}$  and  $\sim 2520\text{--}2542\text{ nm}$  respectively (Figure 29). Other absorption features include the secondary carbonate absorption feature at  $\sim 1875\text{ nm}$ ,  $\sim 1993\text{ nm}$ , and  $\sim 2155\text{ nm}$ . The features are symmetrical in shape.

Bcalc has its features at  $\sim 2335\text{ nm}$  and  $\sim 2531\text{ nm}$  with both their left absorption shoulder different from the right shoulder (Figure 29). The diagnostic secondary carbonate features comprise of a doublet at  $\sim 1875\text{ nm}$  and  $\sim 1993\text{ nm}$  separated by an absorption peak at  $\sim 1892\text{ nm}$ . The right feature of the doublet is deeper than the left feature. Another feature appears at  $\sim 2155\text{ nm}$ . A broad absorption stretch is observed between  $\sim 978\text{ nm}$  and  $\sim 1800\text{ nm}$  with deep features at  $\sim 1100\text{ nm}$ ,  $\sim 1400\text{ nm}$ , and a shallow deep at  $\sim 1700\text{ nm}$  respectively in both Bcalc and Calc1 samples.

Calc1 sample also has a similar absorption feature (deepest) at  $\sim 2335\text{ nm}$  like the Bcalc sample and a different feature shape near  $\sim 2500\text{ nm}$  wavelength position (Figure 29). It shows a more developed second feature at  $\sim 2486\text{ nm}$  which is deeper than the  $\sim 2531\text{ nm}$  feature and the two are separated with a sharp absorption peak at  $\sim 2514\text{ nm}$ . This second feature is poorly developed in the Bcalc sample. Its feature at  $\sim 2155\text{ nm}$  is similar and in the same wavelength position as to the Bcalc sample (Figure 29). The main difference between Bcalc and Calc1 however, is observed in the general appearance of the diagnostic secondary carbonate feature. Whereas Bcalc shows two distinct sharp and deep absorption features separated by an absorption peak, Calc1 shows a broad absorption feature centered at  $\sim 1930\text{ nm}$  characterized by two minor features, one on the right (almost same depth) and the other on the left shoulder.

The Calc2 sample has a broad absorption feature centered at  $\sim 2295$  nm which is different from both Bcalc and Calc1 in shape and wavelength position. The second deepest feature is noted to be similar to Bcalc although at a shorter wavelength position at  $\sim 2520$  nm. Its  $\sim 2155$  nm feature is also at the same position as both Bcalc and Calc1 but with a longer left shoulder as opposed to the symmetrical shoulders in the other two samples. It has a very distinct secondary carbonate feature with similar sharp and deep absorption features at  $\sim 1875$  nm and  $1993$  nm separated by an absorption peak at  $\sim 1920$  nm. Unlike in both Bcalc and Calc1 samples, Calc2 doesn't show well-developed absorption stretch between  $\sim 978$  nm and  $\sim 1800$  but has just the deep feature at  $\sim 1750$  nm.

The sample spectral feature positions compare well with the published spectral library spectra such as USGS with minor position shifts. However, spectral feature shapes are noted to vary especially with regards to the Calc2 sample spectra. Another important spectral feature shape is noted on the diagnostic secondary carbonate feature. Figure 29 below shows SWIR spectral features of calcite variety samples compared to USGS spectral library.

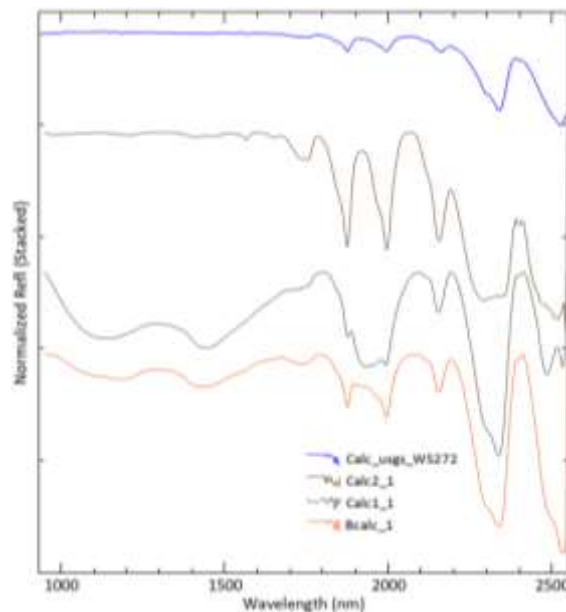


Figure 29: SWIR spectral features of different calcite varieties compared to the USGS spectra and stacked together

#### 4.10.2. Opal-A and Opal-CT

The SWIR spectra of all the opaline silica series have the water features at  $\sim 1400$  nm and  $\sim 1900$  nm and the opal feature near  $\sim 2300$  nm respectively. Opal-A has its main features near  $\sim 2308$  nm,  $\sim 2458$  nm and,  $\sim 1414$  and  $\sim 1914$  nm water features. A broad doublet feature is noted near  $\sim 1768$  nm. The water feature at  $\sim 1414$  nm is sharp with a minor feature on its right shoulder near  $\sim 1460$  nm (Figure 30c). Other features are observed at  $\sim 2458$  nm and  $\sim 2396$  nm. The opal-A sample spectra were compared to the USGS library spectrum and TSG library spectrum. Both the water features and the characteristic opal-A feature compare well with the library spectra (Figure 30d). Opal-CT has slightly broader absorption features when compared to opal-A sample spectra. The water features appear wider at the base as opposed to the opal-A and opal-C sharper features. The opal-CT feature near  $\sim 1780$  has its left arm longer than the right arm which is the opposite in opal-C sample spectrum. The opal-CT main features are formed at  $\sim 2295$  nm,  $\sim 2458$  nm, and water features at  $\sim 1420$  and  $\sim 1900$  nm. Opal-C is observed to have symmetrical features at  $\sim 2300$  nm,  $\sim 1420$  nm,  $\sim 1920$  nm, and a relatively shallow and broad feature at

~1724 nm which appears to have the right arm longer than the left. It also has a small feature on the left arm of the characteristic opal feature at ~2206 nm as noted in Figure 30a.

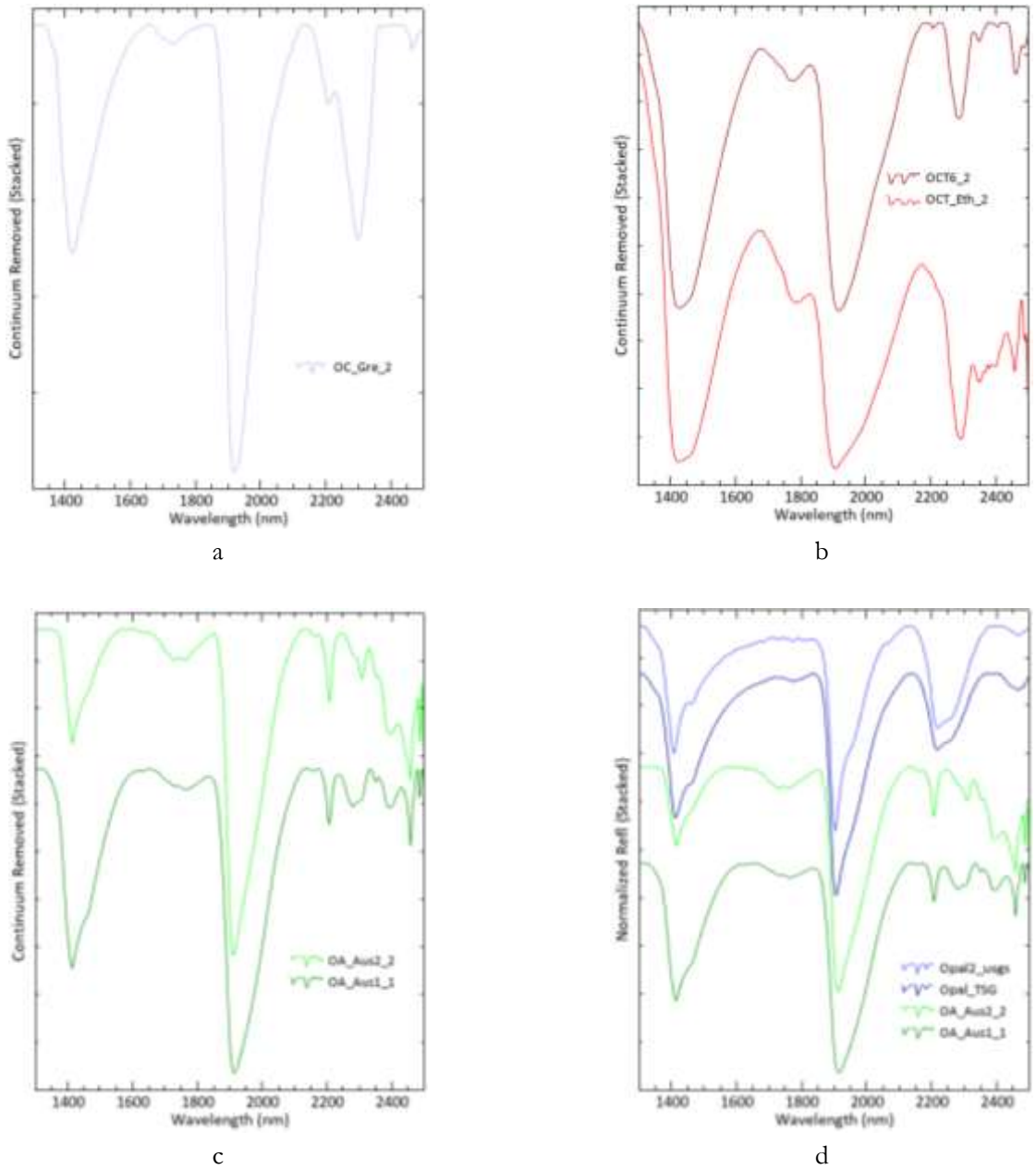


Figure 30: SWIR spectra of opal-C (a), opal-CT samples (b), opal-A samples (c), and comparison of opal-A sample spectra with USGS library spectrum and TSG spectrum (d).

## 5. DISCUSSIONS

### 5.1. LWIR spectral feature differences of silica polymorphs and how they compare to published data

The hyperspectral LWIR image analysis has demonstrated that there exist distinct features in the different silica polymorphs that can be used to distinguish the individual minerals from one another. However, some of the polymorphs such as quartz and chalcedony can hardly be differentiated. The LWIR spectral differences in the different silica polymorphs are mainly noted in the wavelength position shifts, broadening/narrowing of the absorption features and depths of the main features.

#### 5.1.1. Crystalline silica

The main emissivity minima and peaks of all the crystalline samples studied with an exception of tridymite were observed to have common wavelength positions (Figure 27a). The crystalline silica main features are observed within the emissivity range from  $\sim 8000$  nm to  $\sim 9100$  nm and are associated with the Si-O vibrational modes (Goryniuk, 2004; Smith, 1998). The crystalline samples quartz, chalcedony, and cristobalite have their main absorption features near  $\sim 9100$  nm and  $\sim 8300$  nm with an emissivity peak at  $\sim 8600$  nm. Quartz and chalcedony spectra are both similar in shape and wavelength positions of the main emissivity features (Figure 27a). The FWHM of the main emissivity features for quartz and chalcedony measure  $\sim 550$  nm and  $\sim 340$  nm for deepest and 2<sup>nd</sup> deepest features respectively but quartz feature depths differ from those of chalcedony (Table 3). Chalcedony has deeper feature depths of  $\sim 0.43$  and  $0.16$  compared to  $\sim 0.32$  and  $0.21$  of quartz samples representing deepest and 2<sup>nd</sup> deepest features respectively. These feature depth differences have also been documented by other researches. For example, Hardgrove et al. (2016) noted the emissivity feature depth variations in microcrystalline quartz (chalcedony) and quartz noting that the narrowing/broadening in their main features resulted in wavelength position shifts.

Similar observations are evident in the XRD and FTIR-ATR analyses showing quartz, chalcedony, and cristobalite samples having various common features. Chalcedony and cristobalite are characterized by distinct quartz features in both XRD diffractograms (Figure 14) and the FTIR-ATR absorbance spectra (Figure 18a). For example, the XRD diffractogram peaks of chalcedony are all similar to those observed in quartz samples (Figure 14). However, chalcedony diffractogram peaks are broad compared to the relatively narrower quartz peaks. The XRD FWHM for the main peaks denotes chalcedony features to be twice broader with smaller magnitudes compared to the quartz's sharp narrow deep features (Table 4). Frondel (1982) in its findings describes the chalcedony diffractogram peaks as weak X-ray and broad peaks compared to quartz. Both quartz and chalcedony have the same XRD peak positions as noted in the main peaks i.e.,  $\sim 3.34$  Å, and  $\sim 1.81$  Å but slightly differ in peak value near  $\sim 4.25$  Å, with quartz having  $\sim 4.25$  Å while chalcedony higher peak value of  $\sim 4.30$  Å. The clearest difference between quartz and chalcedony is however evident in the FTIR-ATR absorbance features. Chalcedony sample showed a diagnostic chalcedony feature at  $555$   $\text{cm}^{-1}$  (Figure 18a) associated with the hydroxyl bond which causes the Si-OH vibrations (Schmidt and Fröhlich, 2011). The other difference between quartz and chalcedony difference is the chalcedony feature at  $497$   $\text{cm}^{-1}$  that is shifted to  $\sim 505$   $\text{cm}^{-1}$  in quartz (Figure 18a).

The cristobalite sample Crist spectrally resembles quartz with its main absorption features at similar wavelength positions as the fundamental quartz spectral features. The Crist sample, however, shows a secondary feature near  $\sim 8800$  nm which is not seen in the quartz sample (Figure 27a). Additionally, the deepest and 2<sup>nd</sup> deepest Crist features are at  $\sim 8300$  nm and  $\sim 9000$  nm as opposed to quartz features at  $\sim 9000$  nm and  $\sim 8300$  nm respectively. The main emissivity features are associated with the fundamental Si-O

stretching (Goryniuk, 2004; Smith, 1998). There is a significant difference between the spectral appearance of the study cristobalite sample to that of the standard ASU spectral library. To start with, the library spectra have its emissivity peak at **~8300 nm** as opposed to the study sample at **~8600 nm**. Secondly, the library spectra have narrow deep main features with local emissivity near **~8900 and ~8600 nm** while the Crist sample has broad quartz-like features with local emissivity only noted at **~8800 nm**. The local emissivity at **~8800 nm** noted in the Crist sample represents a wavelength shift of about **~100 nm** when compared with library spectra.

The XRD diffractogram peaks of the Crist sample agrees with the LWIR spectral observations. The main diffractogram peaks are observed at **~3.34 Å**, and **~4.25 Å** (Figure 14) which are also the observed main quartz peaks. A broad intensity peak at **~6.88 Å** noted in the Crist sample is missing in the quartz sample diffractogram. Smaller cristobalite peaks which are also noted in opaline silica such as OC\_Gre and OCT1 include **~3.03 Å**, **~1.81 Å**, **~2.23 Å**, **~2.12 Å** and **~2.03 Å** (see Figure 13 and Appendix 7). Likewise, the FTIR-ATR Crist sample spectrum just like the LWIR features and XRD diffractogram peaks has similar features as quartz. The Crist main absorbance features are similar in shape and are formed at the same wavelength positions as quartz main features (Figure 17a). The observed cristobalite features are mainly due to the fundamental vibrations associated with the Si-O stretch as discussed by Smith, (1998) from similar vibrational observations between **~8333 nm ~9100 nm**. Based on all the observations, it is clear that the Crist sample is a quartz mineral with possible traces of cristobalite. These cristobalite traces may be causing the secondary features noted in LWIR at **~8800 nm** as well as the weaker cristobalite peaks in the XRD diffractogram. The overwhelming evidence suggesting a quartz sample can be true given that the Crist sample part studied was embedded within an amethyst quartz host material.

The tridymite emissivity features are distinctly different from all the other crystalline silica samples (quartz, chalcedony, and cristobalite). Physically, tridymite was easily differentiated from chalcedony, quartz, and cristobalite samples using their spectral shape appearance, local emissivity features, and appearance of its main features at shorter wavelengths. It has its main emissivity peak at shorter wavelength position i.e., **~8300 nm** compared to the other crystalline silica samples which were observed at peaks at longer wavelengths i.e., **~8600 nm** (Figure 27a). Tridymite's 2<sup>nd</sup> deepest feature is shifted to the shorter wavelength at **~8200 nm** from the **~8300 nm** position for the other crystalline silica samples. Structurally, it is characterized by the occurrence of poorly-formed local emissivity features within the Si-O vibrational modes caused by the Si-O-Si bonds (Smith, 1998; Michalski et al., 2003). The tridymite standard library spectrum is observed appears broader with the local emissivity features showing a doublet feature with the deepest emissivity feature at the base when compared to the study sample (Figure 22). The library spectrum's 2<sup>nd</sup> feature is also more visible compared to the sample spectrum. The poorly-formed local emissivity features are at the same wavelength positions in both library and study spectra but the 2<sup>nd</sup> feature is at a shorter wavelength in the library spectrum than the study sample spectrum. These variations could be attributed to the fact that the library spectrum was extracted from a natural tridymite sample whereas the study sample was synthesized tridymite. The XRD diffractograms peaks of the tridymite sample are observed at **~4.14 Å** (Figure 14) and near **~2.50 Å** as noted in Appendix 8. These XRD peaks are slightly different from those observed by Awadh and Yaseen (2019) observed the main tridymite XRD peaks near **~4.10 Å** and **~2.51 Å** and described them as the diagnostic tridymite peaks. Just as noted in the emissivity feature variations, this minor peak differences could be attributed to the synthesized sample (e.g., the quality of the synthesis).

### 5.1.2. Opaline silica

The opaline silica polymorphs are characterized by the formation of additional minor local emissivity features apart from the main features at **~9000 nm** and **~8000 nm** caused by the fundamental vibrations

from the Si-O stretching and bending (Goryniuk, 2004). The poorly-formed minor emissivity features are caused by the Si-O-Si vibrations associated with Si-OH (Goryniuk, 2004; Smith, 1998). The opaline silica LWIR spectral features (especially the  $\sim 8000$  nm feature and main emissivity peak at  $\sim 8300$  nm) are formed at shorter wavelength positions compared to the crystalline silica polymorphs (Figure 27a).

Opal-A has its local emissivity features at a longer wavelength of the main emissivity feature at  $\sim 9000$  nm while opal-CT local emissivity features at shorter wavelength positions of main emissivity feature (Figure 27b). This is a major difference noted between these two opaline polymorphs (opal-A and opal-CT). The opal-A local emissivity features are located at  $\sim 11500$  nm and  $\sim 10200$  nm (Figure 24a) which have been attributed to the Si-OH bonds by Smith (1998). On the other hand, the local emissivity features of the opal-CT samples are formed at shorter wavelength positions at  $\sim 8500$  nm and  $\sim 8800$  nm compared to the opal-A sample. All the opal-CT samples have their deepest feature at the same wavelength position except OCT2 slightly shifted ( $\sim 100$  nm) to the shorter wavelength and OCT3 to the longer wavelength (Figure 25a).

The LWIR findings were supported with the findings from the XRD as well as FTIR-ATR analysis. XRD diffractograms analysis of the various opaline silica resulted in varying intensity peaks for the various samples opaline silica studied. The OA\_Aus2 sample has a poorly-formed broad diffractogram peak centered near  $\sim 4.18$  Å and other weak peaks at including  $\sim 2.45$  Å, and  $\sim 2.69$  Å respectively (Figure 15). These broad peaks are due to its highly disordered non-crystalline nature (Curtis et al., 2019). The opal-CT samples have displayed varying XRD patterns of differing peaks. The peaks appear to show the level of the cristobalite-tridymite stacking. For example, some opal-CT samples are observed to have strong tridymite-like layer stacking (indicated with letter T in the diffractograms) while some appear complex with both cristobalite-tridymite layer stacking (marked C and T in the diffractograms) respectively (Figure 15). The opal-CT samples show two main diffractogram peaks, the main broad peak near  $\sim 4.10$  Å and a weak peak near  $\sim 2.51$  Å (Figure 15). This weaker diffractogram peak at  $\sim 2.51$  Å is not observed in the opal-A sample (OA\_Aus2) even though its main peak at  $\sim 4.18$  Å appears like those of some of the opal-CT samples (Figure 15). The opaline silica polymorphs have extensively been studied. Michalski et al. (2003) noted that the opal-CT has a short-range ordering of the cristobalite-tridymite stackings which changes with an increase in crystallinity. The author also indicates that that the crystallinity also may result in either cristobalite/tridymite stacking dominating over the other. The study by Curtis et al. (2019) has demonstrated that the opal-CT samples may have simple or complex diffractogram patterns just as noted in this study.

The opaline silica opal-C (OC\_Gre sample) has its LWIR spectrum exhibiting minor features formed at both shorter and longer wavelengths of the main emissivity absorption feature (Figure 26a). The spectral shape of its main emissivity features (e.g. between 8000-9300 nm) appears like the chalcedony/quartz feature although it a minor feature noted at  $\sim 9000$  nm (Figure 26a). This opal-C spectrum was compared to a spectral library spectrum opal-CT/C suggesting that the library spectrum could not be conclusively classified as either opal-CT or opal-C. The two spectra (library opal-CT/C and OC\_Gre sample) spectral appearances did not show a clear resemblance either. The chalcedony-feature like shape in the OC\_Gre sample suggests a microcrystalline structure probably related to chalcedonic material. The opal-C XRD diffractogram peaks are noted at  $\sim 4.28$  Å with a shorter peak at  $\sim 4.41$  Å. The sample also displayed a strong peak near  $\sim 3.34$  Å, a crystalline quart/microcrystalline chalcedony peak, and other weaker peaks at  $\sim 2.29$  Å and  $\sim 2.12$  Å (Figure 16).

FTIR-ATR results show distinct differences between the crystalline silica and the opaline silica samples. Crystalline silica samples have a doublet absorbance feature near  $\sim 780$   $\text{cm}^{-1}$  while the opaline silica series

have a single feature (Figure 18a). The opaline silica samples also differ from the crystalline samples in appearance i.e., opaline silica samples are characterized by broad small magnitude features compared to the crystalline silica evident from the main absorbance features (Figure 18). A comparison of the opaline silica samples indicates that opal-A (OA\_Aus2) has a broad feature near  $\sim 465 \text{ cm}^{-1}$  with smaller absorbance features that are not observed in either opal-C or opal-CT (Figure 18a). The OA\_Aus2 spectrum is also seen to have a doublet-like feature near the  $\sim 1070 \text{ cm}^{-1}$  feature. Opal-C sample, OC\_Gre generally shows a chalcedonic spectral feature similarity. However, the broadness of the features and the single feature near  $\sim 780 \text{ cm}^{-1}$  disqualifies it from chalcedony which has a doublet at  $\sim 465 \text{ cm}^{-1}$ . OC\_Gre also has a distinct absorbance feature at  $\sim 620 \text{ cm}^{-1}$  and a small feature at the shoulder of the  $\sim 1100 \text{ cm}^{-1}$  feature near  $\sim 1155 \text{ cm}^{-1}$  that differentiates it from opal-A and opal-CT samples. These feature differences amongst the different opaline silica series are in agreement with XRD analysis results and the reclassification OA\_Eth to OCT\_Eth and OA\_Gre to OC\_Gre. The OC\_Gre feature near  $\sim 1155 \text{ cm}^{-1}$  is noted from the findings of Curtis et al. (2019). Adamo et al. (2010) observed that opal-C can be distinctly differentiated from the other opaline silica polymorphs using its absorption features at  $\sim 620 \text{ cm}^{-1}$  and the smaller feature on the shoulder of the  $\sim 1100 \text{ cm}^{-1}$  respectively.

SWIR spectral features of the different opaline silica polymorphs are characterized by distinct opaline features near  $\sim 2300 \text{ nm}$  associated with the Si-OH vibrational modes and active molecular stretching and bending associated with OH and H<sub>2</sub>O bonds near  $\sim 1400 \text{ nm}$  and  $\sim 1900 \text{ nm}$  respectively (Goryniuk, 2004; Milliken et al., 2008). Comparatively, the opaline silica polymorphs have shown feature differences noted from their spectra. The opaline silica series all show a slightly different spectral shape of the feature at  $\sim 1400 \text{ nm}$ . For example, Opal-A has a sharp reflectance with a minor shoulder on the right arm while opal-C shows a relatively less sharp feature without an arm, and the opal-CT feature is broader compared to both opal-A and opal-C (Figure 30). The main absorption feature of opal-A is located to the longer wavelength at  $\sim 2308 \text{ nm}$  followed by that of opal-C at  $\sim 2300 \text{ nm}$  and opal-CT at the shortest wavelength position at  $\sim 2295 \text{ nm}$  (Figure 30). The minor wavelength shifts in the main absorption feature stated above point to the changes in the degree of the disordering and stackings involved in the different opaline silica polymorphs with the highly-disordered opal-A having its main absorption feature at longer wavelength compared to the cristobalite-tridymite disordering. The main opaline silica absorption features as recorded in this study represent nearly  $\sim 100 \text{ nm}$  wavelength position difference compared to observations by Milliken et al. (2008) which stated that the main opaline silica features occur between  $\sim 2210\text{-}2260 \text{ nm}$ .

## 5.2. LWIR spectral differences due to crystallinity of silica polymorphs

There are noticeable changes in both feature shape, width, depth, and wavelength position shifts observed throughout the various silica polymorphs. There is shifting in wavelength position to the longer wavelength as well as shallowing of the 2nd deepest emissivity feature as crystallinity increases i.e., the opaline silica polymorphs have the feature near  $\sim 8000 \text{ nm}$  compared to the  $\sim 8300 \text{ nm}$  for the crystalline silica (Figure 27a). The FWHM of the deepest feature is also observed to increase from the crystalline samples to the amorphous opal-A. Quartz/chalcedony both have  $\sim 550 \text{ nm}$  compared to opal-A with  $\sim 800 \text{ nm}$  (Table 3) of the deepest feature an indicator of the effects of crystalline changes. Besides, the local emissivity features are observed in the non-crystalline opaline silica but disappear as crystallinity increases.

## 5.3. LWIR spectral feature differences of different colored opaline silica

No significant observation has been made to suggest that there are spectral feature changes e.g., shape or wavelength position which is associated with the differences in physical color appearance. For instance,

opal-CT samples with different colors are noted to similar wavelength positions for the main emissivity features (Figure 25a). According to Mukherjee (2011), the color-play-of noticed in different opaline silica samples results from the diffracted light by the packed hydrated silica spheres forming the opaline minerals. This, therefore, may explain why the differently colored opal-CT samples still display similar emissivity features.

#### 5.4. Quantitative comparison of LWIR and XRD features (e.g., magnitude, depth and width) of silica polymorphs

The quantitative comparison of the broadness (FWHM) of the various silica polymorphs shows the feature systematic increase in the widths as the crystallinity of the sample minerals reduces i.e., small widths in crystalline series and large widths in non-crystalline series. This applies also to the depths of the emissivity features as observed on the deepest feature values (Table 3). The FWHM of the deepest feature of quartz and chalcedony is about **~550 nm** while that of opal-A deepest feature is **~880 nm**. Quartz deepest feature depth is smaller at **0.32** and gets higher as the samples become less crystalline as observed in opal-A deepest feature with a value of **0.78** (Table 3). From the XRD diffractograms, the samples show varying values of FWHM and magnitudes for the first 3 main diffractogram peaks. The XRD main features' FWHM for quartz and chalcedony shows that chalcedony FWHM values for the main peaks are twice those of quartz (Table 4). Quartz's main features magnitudes are higher than those of chalcedony.

#### 5.5. Calcite LWIR spectral feature differences in comparison with published data

The study samples have displayed their main emissivity at  $\sim 11300$  nm (Calc1),  $\sim 11350$  nm and  $\sim 11200$  nm (Calc2), and  $\sim 11250$  nm for the bladed/platy calcite (Bcalc) variety. All samples displayed the typical calcite feature near  $\sim 11300$  nm (Green and Schodlok, 2016; Lane and Christensen, 1997) although some samples have shown shifts of between  $\sim 50$ - $100$  nm. The Calc2 main feature near  $\sim 11200$  nm suggests that the sample could be having contents of Mg ions. In its findings, Green and Schodlok (2016) observed that dolomite carbonate variety has a diagnostic feature near  $\sim 11236$  nm which is close to the observed value for Calc2 sample. The samples have a secondary quartz-like emissivity feature in the wavelength range between  $\sim 8000$ - $9000$  nm (strong quartz-like feature noted in Calc2 variety). The quartz feature is an indication of the presence of some quartz material in the samples. The main emissivity feature is observed at  $\sim 11300$  nm in Calc1 variety. From the XRD results, the 3 different calcite samples all have the same diffractogram peak values. The differences of the samples are indicated by the peak broadness/sharpness. The bladed calcite shows broad weak peaks compared to the other calcite samples (Figure 17). From the SWIR spectra, the Calc2 sample has a broad reflectance feature near  $\sim 2295$  nm compared to the other calcite varieties.

#### 5.6. Possible cause of shifts in spectral feature positions in calcite varieties

The shifts in wavelength positions for the different samples range between  $\sim 50$ - $100$  nm. Calc2 calcite variety wavelength position of the emissivity feature near  $\sim 12200$  nm is closer to  $\sim 11236$  nm, the values determined to be a diagnostic feature position of dolomite by Green and Schodlok (2016). This implies that the shifts could be due to mineralogical changes.

## 6. CONCLUSIONS AND RECOMMENDATIONS

### 6.1. Conclusions

Several observations have been made from the different study samples showing distinguishable LWIR spectral features of the different silica polymorphs. XRD and FTIR-ATR techniques were both used in first classifying the different silica polymorphs. The SWIR analysis of the SWIR-active samples has also provided very useful information on whether the opaline silica polymorphs and the calcite varieties show any differences.

The crystalline silica polymorphs are distinctly different from the non-crystalline silica (opaline silica) polymorphs both in spectral feature shape and wavelength positions. Crystalline silica samples (quartz, chalcedony, cristobalite, and tridymite) have their emissivity peak and the 2nd deepest feature at shorter wavelength positions compared to the opaline silica. The 2nd deepest feature is formed at ~8200 nm (tridymite)/~8300 nm (quartz, chalcedony, cristobalite) with emissivity peak at ~8300 nm (tridymite)/~8600 nm (quartz, chalcedony, cristobalite). The opaline silica 2nd feature is near ~8000 nm with the main emissivity peak at ~8300 nm. The crystalline samples are observed to have narrower features as noted in quartz (~340 nm) while the opaline silica samples are broader in size (i.e., opal-A ~880 nm). The formation of local emissivity features in the opaline silica samples is also another important difference between the crystalline and opaline silica polymorphs.

Quartz and chalcedony have similar spectral feature appearances at the same wavelength positions but distinctly different from other silica polymorphs with an exception of the study cristobalite sample. Despite the similarity in appearance, their deepest feature depths are different. Chalcedony has a deeper main feature nearly about 1.5 times that of quartz.

The LWIR spectral features observed from the Crist sample cannot be relied on conclusively as true spectral features of cristobalite. The spectrum highly resembles a quartz mineral with typical quartz features at ~8300 nm and ~9000 nm separated by quartz emissivity peak of ~8600 nm respectively. The library spectrum of cristobalite does not compare well with the Crist sample spectrum except for the minor local emissivity feature at ~8900 nm which is nearly in the same wavelength position with a small hump-like feature near ~8800 nm (~100 nm shift) in the Crist sample. The XRD and FTIR-ATR results confirm the observations made from the LWIR spectral analysis. The XRD diffractogram of the Crist sample is dominated by the quartz peaks including ~3.34, and ~4.25 Å. The absorbance features from the FTIR-ATR also strongly resemble quartz features. Therefore, this study considers the Crist sample as a quartz mineral with possible traces of cristobalite.

Tridymite has its emissivity peak and 2nd feature at shorter wavelength positions at ~8300 nm and ~8200 nm than both chalcedony and quartz with emissivity peaks at ~8600 nm and 2nd feature at ~8300 nm respectively. Apart from the feature position, tridymite has a broad main feature and a relatively small shallow feature while quartz and chalcedony have closely related features. Compared to opaline silica polymorphs, tridymite shows a relatively narrow well-formed 2nd feature at a longer wavelength (~8200 nm) to the poorly-formed broad feature at ~8000 nm for the opaline silica polymorphs.

The opaline silica polymorphs can be distinguished from one another based on the position of their local emissivity minima. Opal-A has local emissivity features at longer wavelengths at ~11500 nm and ~10500 nm whereas opal-CT has such features at shorter wavelengths at ~8500 nm and ~8800 nm. The

chalcedonic spectral appearance of opal-C indicates a possible presence of microcrystalline material in the opal-C sample.

The emissivity feature positions and width changes with crystallinity. For example, crystalline samples have emissivity features at longer wavelength positions (e.g., peaks: quartz/chalcedony (~8600 nm), tridymite (~8200 nm); 2nd feature: quartz/chalcedony (~8300 nm), tridymite (~8200 nm)) compared to opaline silica peaks at ~8200 nm and 2nd feature at ~8000 nm respectively. The opaline silica also has broad deeper main features than the crystalline silica. Local minor emissivity minima are observed to form as crystallinity reduces (e.g., more evident in the opaline silica than in quartz/chalcedony)

No visible LWIR spectral changes due to the physical color appearance of the different opaline silica samples were observed. Likewise, not enough spectral changes are observed in the calcite samples to conclusively distinguish the bladed calcite from the other calcite varieties

## **6.2. Recommendations**

Applying the observed results on to downhole geothermal drill cuttings for the determination of the various silica polymorph varieties as intended in objective 2 of this study but which could not be carried out due to the ongoing COVID-19 pandemic. Further LWIR spectroscopy investigations are also recommended especially on cristobalite, opal-C, and bladed calcite to be able to ascertain the exact wavelength positions and shape of their emissivity features which was limited in this study since only one sample each was studied.

## LIST OF REFERENCES

---

- Adamo, I., Ghisoli, C., and Caucia, F., 2010, A contribution to the study of FTIR spectra of opals: *Neues Jahrbuch Fur Mineralogie-Abhandlungen*, v. 187/1, p. 63–68, doi:10.1127/0077-7757/2010/0161.
- Akaku, K., 1990, Geochemical study on mineral precipitation from geothermal waters at the fushime field, Kyushu, Japan: *Geothermics*, v. 19, p. 455–467, doi:10.1016/0375-6505(90)90058-J.
- Alt-Epping, P., Diamond, L.W., Häring, M.O., Ladner, F., and Meier, D.B., 2013, Prediction of water–rock interaction and porosity evolution in a granitoid-hosted enhanced geothermal system, using constraints from the 5km Basel-1 well: *Applied Geochemistry*, v. 38, p. 121–133, doi:10.1016/j.apgeochem.2013.09.006.
- Awadh, S.M., and Yaseen, Z.M., 2019, Investigation of silica polymorphs stratified in siliceous geode using FTIR and XRD methods: *Materials Chemistry and Physics*, v. 228, p. 45–50, doi:10.1016/j.matchemphys.2019.02.048.
- Baldrige, A.M., Hook, S.J., Grove, C.I., and Rivera, G., 2009, The ASTER spectral library version 2.0: *Remote Sensing of Environment*, v. 113, p. 711–715, doi:10.1016/j.rse.2008.11.007.
- Bargar, K.E., Keith, T.E.C., and Beeson, M.H., 1993, Hydrothermal alteration in the Mount Hood area, Oregon: <https://pubs.usgs.gov/bul/2054/report.pdf>.
- Bedell, R.L., Rivard, B., Browning, D., and Coolbaugh, M., 2017, Spectral Geology and Remote Sensing Paper 81 Thermal Infrared Sensing for Exploration and Mining-An Update on Relevant Systems for Remote Acquisition to Drill Core Scanning, *in* Tschirhart, V. and Thomas, M.D. eds., *Proceedings of Exploration*, v. 17, p. 881–897, <http://www.dmec.ca/getattachment/a9235e86-de6f-41d0-8bc3-c59d88993d66/Resources/Exploration-17>.
- Calvin, W.M., Littlefield, E.F., and Kratt, C., 2015, Remote sensing of geothermal-related minerals for resource exploration in Nevada: *Geothermics*, v. 53, p. 517–526, doi:10.1016/j.geothermics.2014.09.002.
- Calvin, W.M., and Pace, E.L., 2016, Mapping alteration in geothermal drill core using a field portable spectroradiometer: *Geothermics*, v. 61, p. 12–23, doi:10.1016/j.geothermics.2016.01.005.
- Chauviré, B., Rondeau, B., and Mangold, N., 2017, Near infrared signature of opal and chalcedony as a proxy for their structure and formation conditions: *European Journal of Mineralogy*, v. 29, p. 409–421, doi:10.1127/ejm/2017/0029-2614.
- Christensen, P.R., Bandfield, J.L., Hamilton, V.E., Howard, D.A., Lane, M.D., Piatek, J.L., Ruff, S.W., and Stefanov, W.L., 2000, A thermal emission spectral library of rock-forming minerals: *Journal of Geophysical Research: Planets*, v. 105, p. 9735–9739, doi:10.1029/1998JE000624.
- Clark, R.N., 1999, Spectroscopy of Rocks and Minerals and Principles of Spectroscopy. *Manual of Remote Sensing*, *in* Rencz, A.N. ed., *Remote Sensing for the Earth Sciences: Manual of Remote Sensing*, v. 3, p. 3–58.
- Coolbaugh, M.F., Kratt, C., Fallacaro, A., Calvin, W.M., and Taranik, J.V., 2007, Detection of geothermal anomalies using Advanced Spaceborne Thermal Emission and Reflection Radiometer (ASTER) thermal infrared images at Bradys Hot Springs, Nevada, USA: *Remote Sensing of Environment*, v. 106, p. 350–359, doi:10.1016/j.rse.2006.09.001.
- Curtis, N.J., Gascooke, J.R., Johnston, M.R., and Pring, A., 2019, A Review of the Classification of Opal with Reference to Recent New Localities: *Minerals*, v. 9, p. 299, doi:10.3390/min9050299.
- Diamond, L.W., and Alt-Epping, P., 2014, Predictive modelling of mineral scaling, corrosion and the performance of solute geothermometers in a granitoid-hosted, enhanced geothermal system: *Applied Geochemistry*, v. 51, p. 216–228, doi:10.1016/j.apgeochem.2014.09.017.
- Elzea, J.M., Odom, I.E., and Miles, W.J., 1994, Distinguishing well ordered opal-CT and opal-C from high temperature cristobalite by x-ray diffraction: *Analytica Chimica Acta*, v. 286, p. 107–116, doi:10.1016/0003-2670(94)80182-7.
- Fox, N., Parbhakar-Fox, A., Moltzen, J., Feig, S., Goemann, K., and Huntington, J., 2017, Applications of hyperspectral mineralogy for geoenvironmental characterisation: *Minerals Engineering*, v. 107, p. 63–77, doi:10.1016/j.mineng.2016.11.008.
- Frondel, C., 1982, Structural hydroxyl in chalcedony (type B quartz): *American Mineralogist*, v. 67, p. 1248–1257.
- García, A.V., Thomsen, K., and Stenby, E.H., 2006, Prediction of mineral scale formation in geothermal and oilfield operations using the Extended UNIQUAC model: *Geothermics*, v. 35, p. 239–284,

doi:10.1016/j.geothermics.2006.03.001.

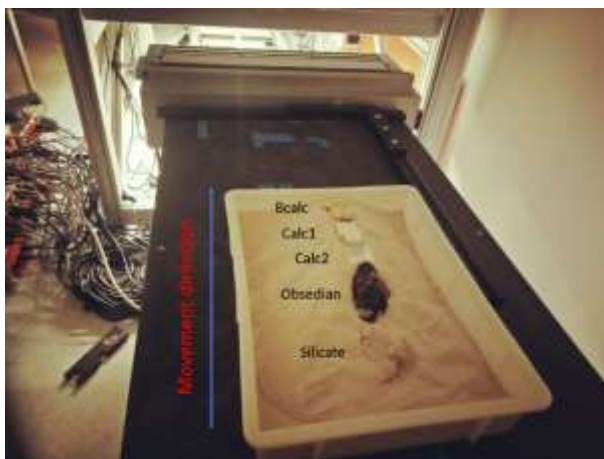
- Godinho, J.R.A., and Withers, P.J., 2018, Time-lapse 3D imaging of calcite precipitation in a microporous column: *Geochimica et Cosmochimica Acta*, v. 222, p. 156–170, doi:10.1016/j.gca.2017.10.024.
- Goryniuk, M.C., 2004, The reflectance spectra of opal-A (0.5–25  $\mu\text{m}$ ) from the Taupo Volcanic Zone: Spectra that may identify hydrothermal systems on planetary surfaces: *Geophysical Research Letters*, v. 31, p. L24701, doi:10.1029/2004GL021481.
- Green, D., and Schodlok, M., 2016, Characterisation of carbonate minerals from hyperspectral TIR scanning using features at 14 000 and 11 300 nm: *Australian Journal of Earth Sciences*, v. 63, p. 1–7, doi:10.1080/08120099.2016.1225601.
- Hardgrove, C.J., Rogers, A.D., Glotch, T.D., and Arnold, J.A., 2016, Thermal emission spectroscopy of microcrystalline sedimentary phases: Effects of natural surface roughness on spectral feature shape: *Journal of Geophysical Research: Planets*, v. 121, p. 542–555, doi:10.1002/2015JE004919.
- Hedenquist, J.W., 1991, Boiling and dilution in the shallow portion of the Waiotapu geothermal system, New Zealand: *Geochimica et Cosmochimica Acta*, v. 55, p. 2753–2765, doi:10.1016/0016-7037(91)90442-8.
- Henry, D.G., Watson, J.S., and John, C.M., 2017, Assessing and calibrating the ATR-FTIR approach as a carbonate rock characterization tool: *Sedimentary Geology*, v. 347, p. 36–52, doi:10.1016/j.sedgeo.2016.07.003.
- Herdianita, N.R., Browne, P.R.L., Rodgers, K.A., and Campbell, K.A., 2000, Mineralogical and textural changes accompanying ageing of silica sinter: *Mineralium Deposita*, v. 35, p. 48–62, doi:10.1007/s001260050005.
- van den Heuvel, D.B., Gunnlaugsson, E., Gunnarsson, I., Stawski, T.M., Peacock, C.L., and Benning, L.G., 2018, Understanding amorphous silica scaling under well-constrained conditions inside geothermal pipelines: *Geothermics*, v. 76, p. 231–241, doi:10.1016/j.geothermics.2018.07.006.
- Ilieva, A., Mihailova, B., Tsintsov, Z., and Petrov, O., 2007, Structural state of microcrystalline opals: A Raman spectroscopic study: *American Mineralogist*, v. 92, p. 1325–1333, doi:10.2138/am.2007.2482.
- Jamero, J., Zarrouk, S.J., and Mroczek, E., 2018, Mineral scaling in two-phase geothermal pipelines: Two case studies: *Geothermics*, v. 72, p. 1–14, doi:10.1016/j.geothermics.2017.10.015.
- Jébrak, M., 2015, Hydrothermal Alteration, *in* *Encyclopedia of Astrobiology*, Berlin, Heidelberg, Springer Berlin Heidelberg, p. 1156–1157, doi:10.1007/978-3-662-44185-5\_5150.
- Koerting, F., Rogass, C., Kaempf, H., Lubitz, C., Harms, U., Schudack, M., Kokaly, R., Mielke, C., Boesche, N., and Altenberger, U., 2015, Drill core mineral analysis by means of hyperspectral imaging spectrometer HySpex, XRD, and ASD in proximity of the Mytina Maar, Czech Republic: *ISPRS - International Archives of the Photogrammetry, Remote Sensing and Spatial Information Sciences*, v. XL-1-W5, p. 417–424, doi:10.5194/isprsarchives-XL-1-W5-417-2015.
- Kokaly, R.F., Clark, R.N., Swayze, G.A., Livo, K.E., Hoefen, T.M., Pearson, N.C., Wise, R.A., Benzel, W.M., Lowers, H.A., Driscoll, R.L., and Klein, A.J., 2017, USGS Spectral Library Version 7: U.S. Geological Survey Data Series 1035, 61 p., <https://doi.org/10.3133/ds1035>
- Kruse, F.A., Bedell, R.L., Taranik, J. V, Peppin, W.A., Weatherbee, O., and Calvin, W.M., 2012, Mapping alteration minerals at prospect, outcrop and drill core scales using imaging spectrometry: *International Journal of Remote Sensing*, v. 33, p. 1780–1798, doi:10.1080/01431161.2011.600350.
- Lane, M.D., and Christensen, P.R., 1997, Thermal infrared emission spectroscopy of anhydrous carbonates: *Journal of Geophysical Research: Planets*, v. 102, p. 25581–25592, doi:10.1029/97JE02046.
- Lenher, V., 1921, Silic Acid: *Journal of the American Chemical Society*, v. 43, p. 391–396, doi:10.1021/ja01436a002.
- Libbey, R.B., and Williams-Jones, A.E., 2016, Compositions of hydrothermal silicates and carbonates as indicators of physicochemical conditions in the Reykjanes geothermal system, Iceland: *Geothermics*, v. 64, p. 15–27, doi:10.1016/j.geothermics.2016.04.007.
- Lynne, B.Y., Campbell, K.A., Moore, J.N., and Browne, P.R.L., 2005, Diagenesis of 1900-year-old siliceous sinter (opal-A to quartz) at Opal Mound, Roosevelt Hot Springs, Utah, U.S.A.: *Sedimentary Geology*, v. 179, p. 249–278, doi:10.1016/j.sedgeo.2005.05.012.
- Majorowicz, J., and Minea, V., 2015, Geothermal Energy Potential in Low Enthalpy Areas as a Future Energy Resource: Identifying Feasible Targets, Quebec, Canada, Study Case: *Resources*, v. 4, p. 524–547, doi:doi.org/10.3390/resources4030524.

- Michalski, J.R., Kraft, M.D., Diedrich, T., and Sharp, T.G., 2003, Thermal emission spectroscopy of the silica polymorphs and considerations for remote sensing of Mars: *Geophysical Research Letters*, v. 30, p. 2008, doi:10.1029/2003GL018354.
- Milliken, R.E., Swayze, G. A., Arvidson, R. E., Bishop, J. L., Clark, R. N., Ehlmann, B. L., Green, R. O., Grotzinger, J. P., Morris, R. V., Murchie, S. L., Mustard, J. F., and Weitz, C., 2008, Opaline silica in young deposits on Mars: *Geology*, v. 36, p. 847, doi:10.1130/G24967A.1.
- Mukherjee, S., 2011, *Applied Mineralogy; Applications in Industry and Environment* (S. Mukherjee, Ed.): Springer, Dordrecht, The Netherlands, 584 p., <http://gen.lib.rus.ec/book/index.php?md5=46B339352F52DB2EE5D43A088E0C5D6D>.
- Müller, C.M., Pejčić, B., Esteban, L., Piane, C.D., Raven, M., and Mizaikoff, B., 2015, Infrared Attenuated Total Reflectance Spectroscopy: An Innovative Strategy for Analyzing Mineral Components in Energy Relevant Systems: *Scientific Reports*, v. 4, p. 6764, doi:10.1038/srep06764.
- Poonosamy, J., Westawalbesloh, C., Deissmann, G., Mahrous, M., Curti, E., Churakov, S. V., Klinkeberg, M., Kohlheyer, D., von Lieres, E., Bosbach, D., and Prasianakis, N. I., 2019, A microfluidic experiment and pore scale modelling diagnostics for assessing mineral precipitation and dissolution in confined spaces: *Chemical Geology*, v. 528, p. 119264, doi:10.1016/j.chemgeo.2019.07.039.
- Reyes, A.G., 1990, Petrology of Philippine geothermal systems and the application of alteration mineralogy to their assessment: *Journal of Volcanology and Geothermal Research*, v. 43, p. 279–309, doi:10.1016/0377-0273(90)90057-M.
- Richter, B., Steingrímsson, B., Ólafsson, M., and Karlsdóttir, R., 2010, Geothermal Surface Exploration in Iceland, *in* Proceedings World Geothermal Congress, Bali, Indonesia, Iceland GeoSurvey, p. 25–29.
- Ruff, S.W., Farmer, J. D., Calvin, W. M., Herkenhoff, K. E., Johnson, J. R., Morris, R. V., Rice, M. S., Arvidson, R. E., Bell III, J. F., Christensen, P. R., and Squyres, S. W., 2011, Characteristics, distribution, origin, and significance of opaline silica observed by the Spirit rover in Gusev crater, Mars: *Journal of Geophysical Research*, v. 116, p. E00F23, doi:10.1029/2010JE003767.
- Schmidt, P., and Fröhlich, F., 2011, Temperature dependent crystallographic transformations in chalcedony, SiO<sub>2</sub>, assessed in mid infrared spectroscopy: *Spectrochimica Acta Part A: Molecular and Biomolecular Spectroscopy*, v. 78, p. 1476–1481, doi:10.1016/j.saa.2011.01.036.
- Schodlok, M.C., Green, A., and Huntington, J., 2016, A reference library of thermal infrared mineral reflectance spectra for the HyLogger-3 drill core logging system: *Australian Journal of Earth Sciences*, v. 63, p. 941–949, doi:10.1080/08120099.2016.1234508.
- Shinohara, Y., and Kohyama, N., 1990, Synthesis of well crystallized cristobalite as a reference mineral: *Industrial Health*, v. 28, p. 139–143, doi:10.2486/indhealth.28.139.
- Simmons, S.F., and Christenson, B.W., 1994, Origins of calcite in a boiling geothermal system: *American Journal of Science*, v. 294, p. 361–400, doi:10.2475/ajs.294.3.361.
- Simmons, S.F., Mauk, J.L., and Simpson, M.P., 2000, The mineral products of boiling in the Golden Cross epithermal deposit, *in* New Zealand Minerals & Mining Conference Proceedings, Auckland, Geology Department, University of Auckland, p. 209–216.
- Smith, D.K., 1998, Opal, cristobalite, and tridymite: Noncrystallinity versus crystallinity, nomenclature of the silica minerals and bibliography: *Powder Diffraction*, v. 13, p. 2–19, doi:10.1017/S0885715600009696.
- Specim, 2014, Spectral Camera LWIR: Specim Spectral Imaging, p. 1–2, <https://www.specim.fi/hyperspectral-cameras/> (accessed October 2019).
- Stimac, J., Sihotang, A.M., Mussofan, W., Baroek, M., Jones, C., Moore, J.N., and Schmitt, A.K., 2019, Geologic controls on the Muara Laboh geothermal system, Sumatra, Indonesia: *Geothermics*, v. 82, p. 97–120, doi:10.1016/j.geothermics.2019.06.002.
- Tappert, M.C., Rivard, B., Fulop, A., Rogge, D., Feng, J., Tappert, R., and Stalder, R., 2015, Characterizing Kimberlite Dilution by Crustal Rocks at the Snap Lake Diamond Mine (Northwest Territories, Canada) using SWIR (1.90–2.36  $\mu$  m) and LWIR (8.1–11.1  $\mu$  m) Hyperspectral Imagery Collected from Drill Core: *Economic Geology*, v. 110, p. 1375–1387, doi:10.2113/econgeo.110.6.1375.
- Tian, H., Xu, T., Zhu, H., Yang, C., and Ding, F., 2019, Heterogeneity in mineral composition and its impact on the sealing capacity of caprock for a CO<sub>2</sub> geological storage site: *Computers & Geosciences*, v. 125, p. 30–42, doi:10.1016/j.cageo.2019.01.015.
- Tut Haklidir, F., and Haklidir, M., 2017, Fuzzy control of calcium carbonate and silica scales in geothermal systems: *Geothermics*, v. 70, p. 230–238, doi:10.1016/j.geothermics.2017.07.003.

- Vaughan, R.G., Calvin, W.M., and Taraniq, J. V., 2003, SEBASS hyperspectral thermal infrared data: surface emissivity measurement and mineral mapping: *Remote Sensing of Environment*, v. 85, p. 48–63, doi:10.1016/S0034-4257(02)00186-4.
- Yoo, S., Mito, Y., Ueda, A., and Matsuoka, T., 2013, Geochemical Clogging in Fracture and Porous Rock for CO<sub>2</sub> Mineral Trapping: *Energy Procedia*, v. 37, p. 5612–5619, doi:10.1016/j.egypro.2013.06.483.
- Zaini, N., van der Meer, F., and van der Werff, H., 2014, Determination of Carbonate Rock Chemistry Using Laboratory-Based Hyperspectral Imagery: *Remote Sensing*, v. 6, p. 4149–4172, doi:10.3390/rs6054149.

# LIST OF APPENDICES

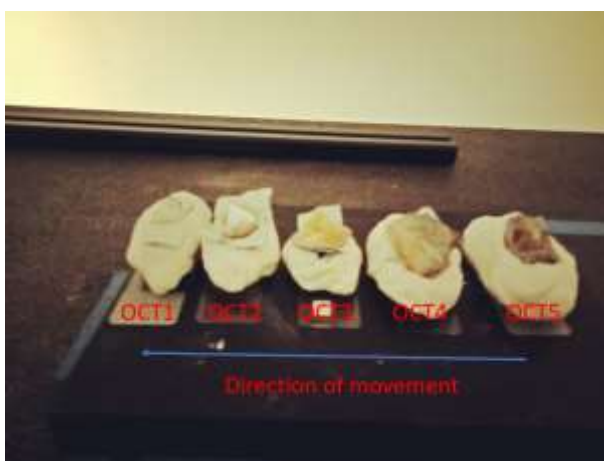
---



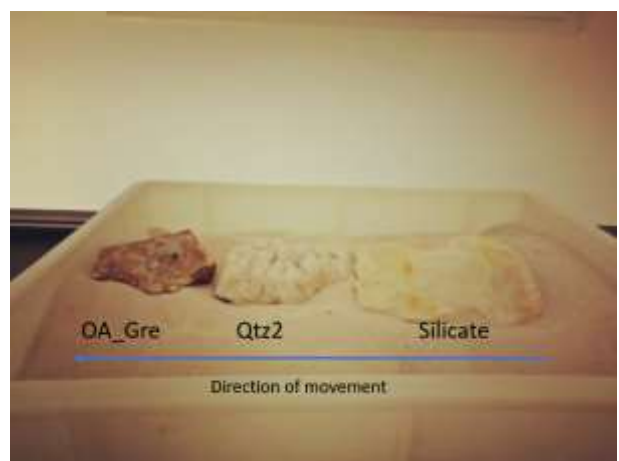
a



b

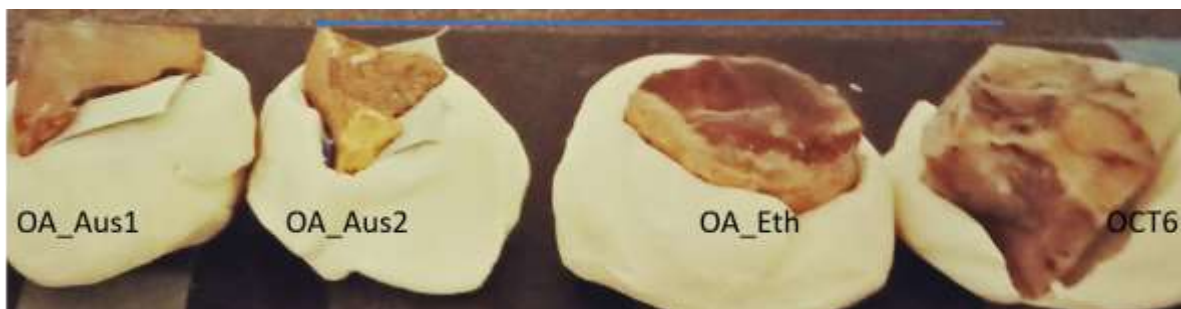


c

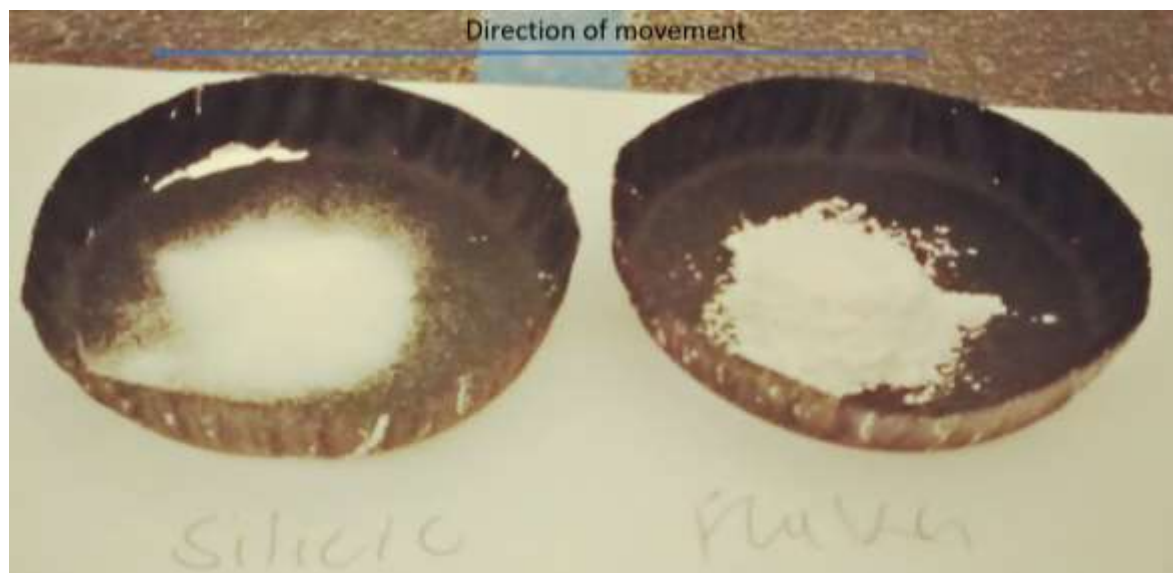


d





e

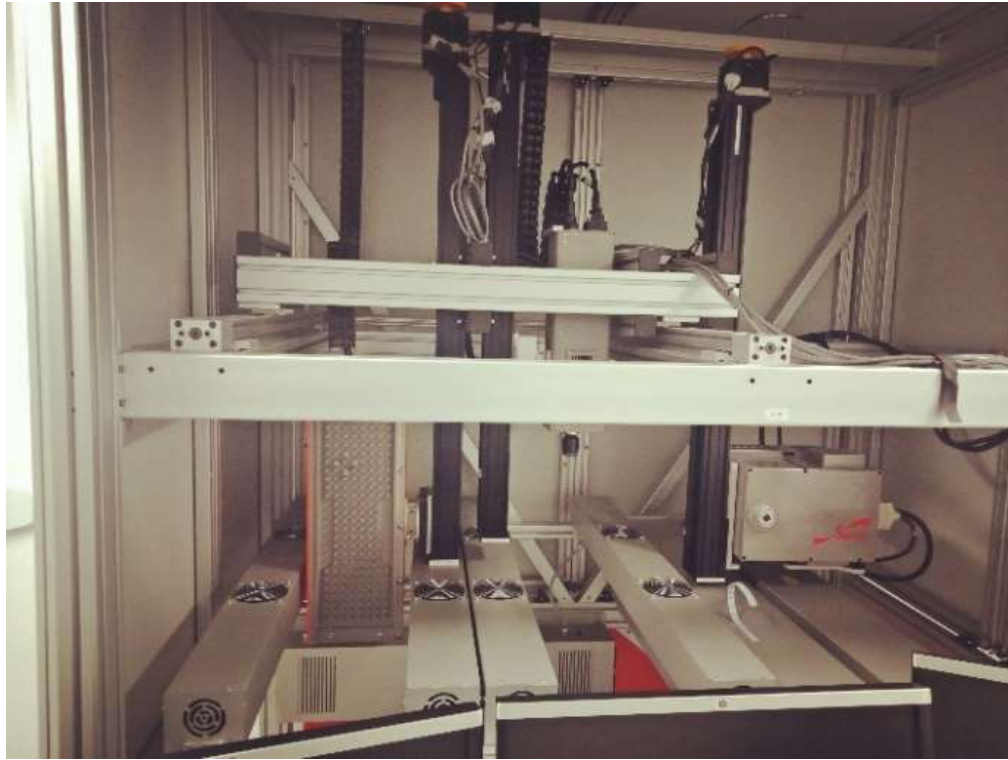


f

Appendix 1: Photos of all the samples arranged in a sand-filled box (a & d) or on top of putty on a plunk of wood during measurements at the BGR lab in Hannover, Germany.



Appendix 2: XRD log file showing how the different samples were powdered for XRD and FTIR-ATR analysis

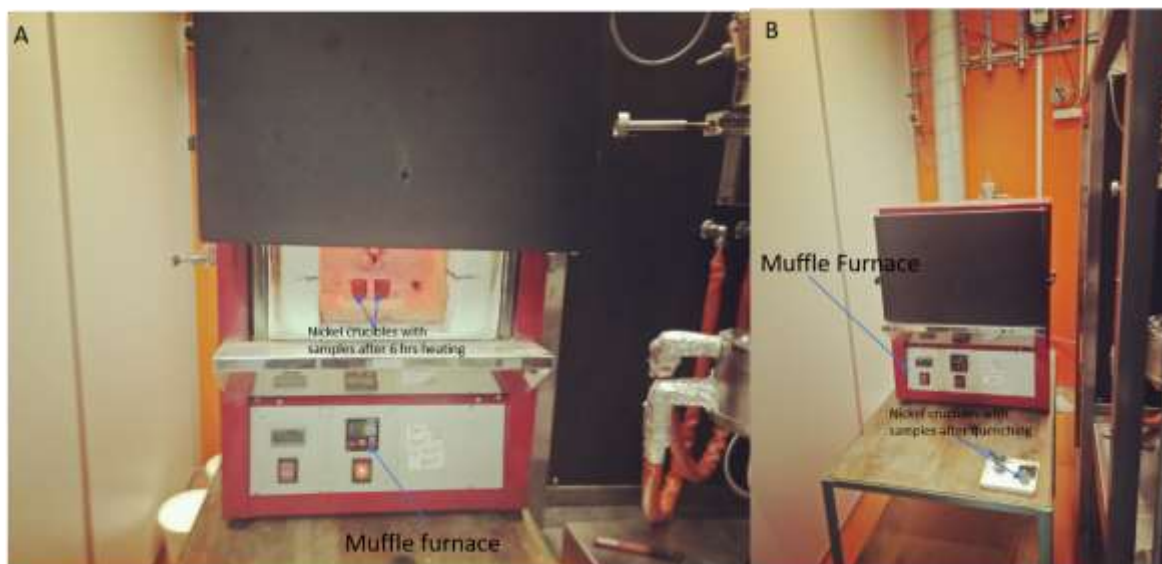


Appendix 3: Arrangement of the spectral LWIR and SWIR cameras at BGR, Hannover, Germany.



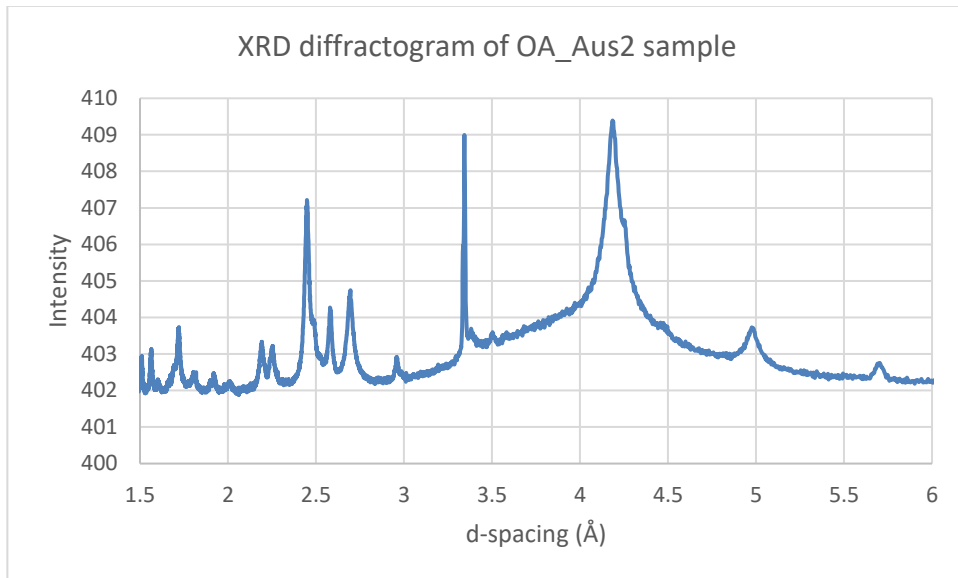
**Drill\_cuttings\_log.pdf**

Appendix 4: Downhole geothermal drill cuttings from Olkaria, Kenya collected during fieldwork

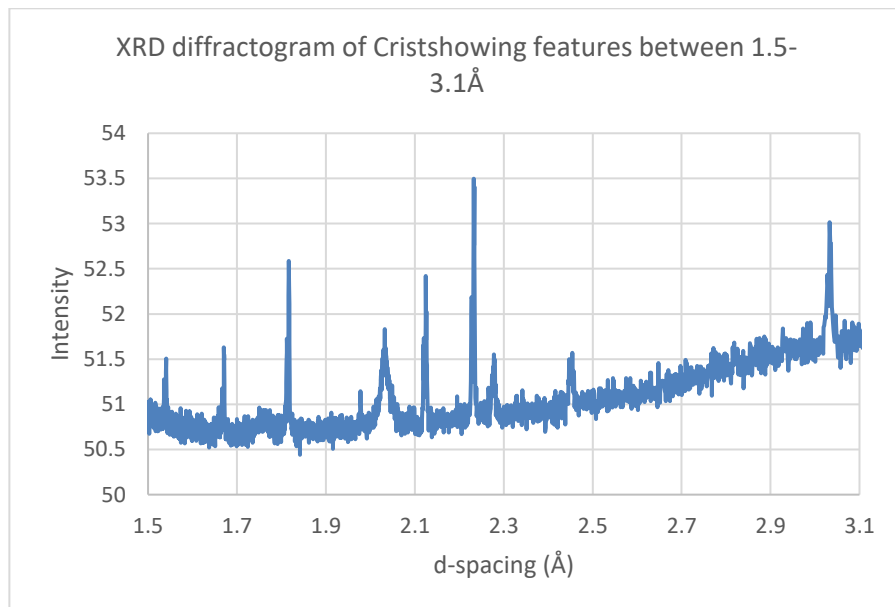


Appendix 5: Synthesis of tridymite samples at the University of Twente's high-pressure laboratory. Figure (A) showing samples in the furnace after 6 hrs heating to 1000°C and (B) after quenching

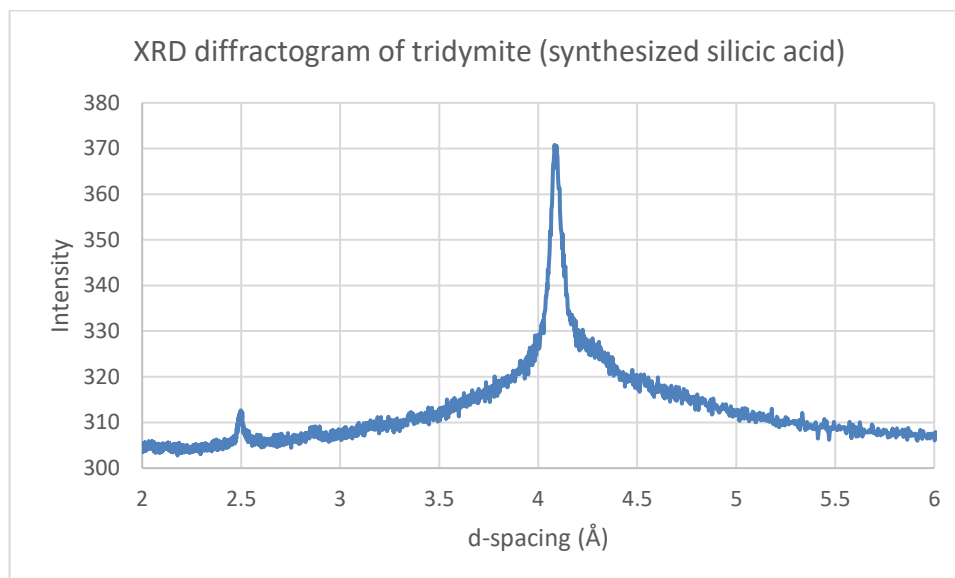
Appendix 6: XRD diffractogram for opal-A sample (OA\_Aus2)



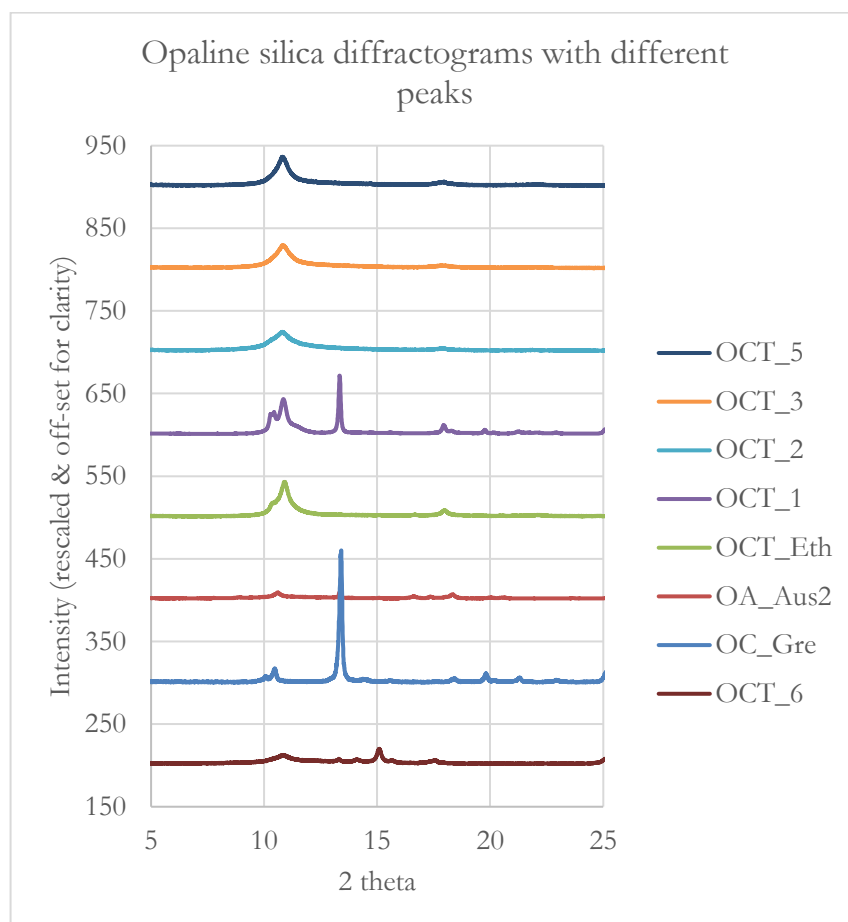
Appendix 7: Rescaled XRD diffractogram for Crist sample showing minor peaks between 1.5-3.1 Å



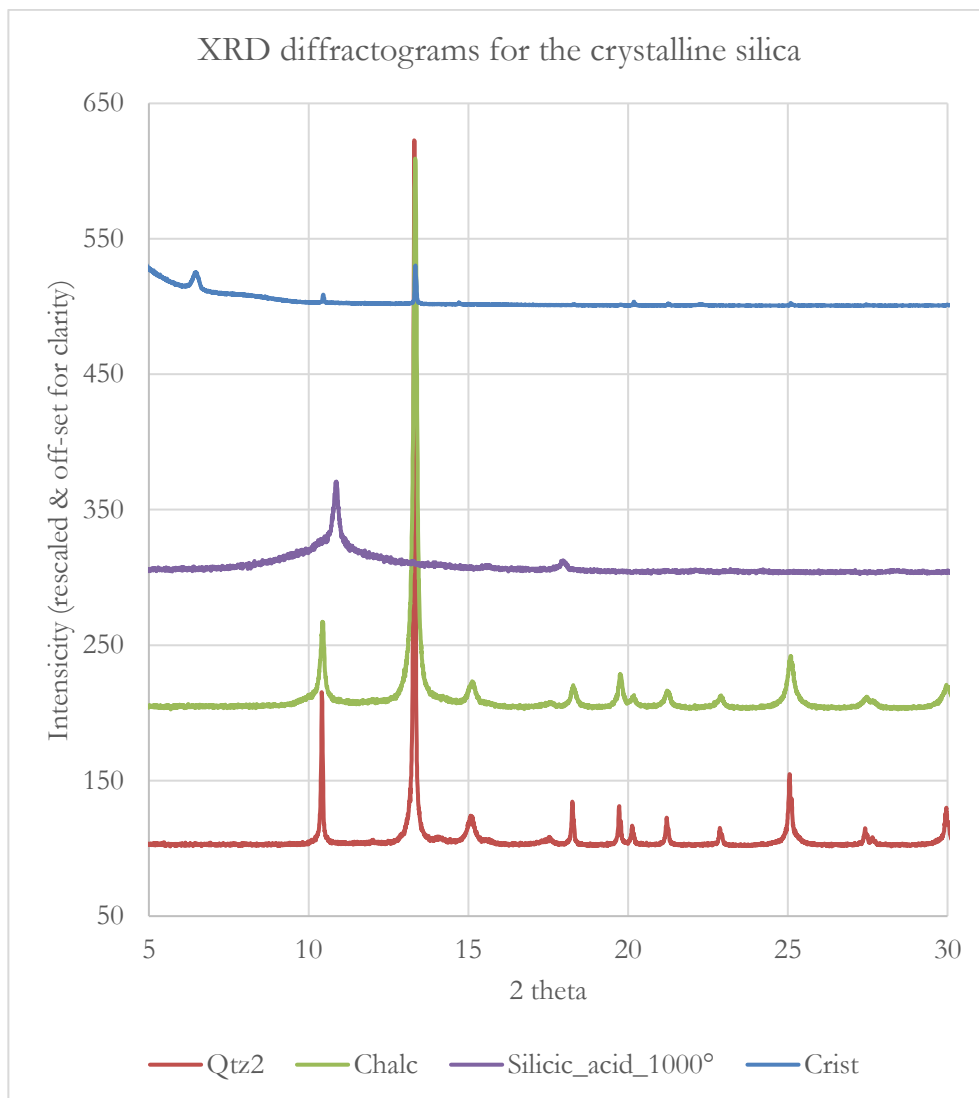
Appendix 8: XRD diffractogram of tridymite showing the main intensity peaks at  $\sim 2.50 \text{ \AA}$  and  $\sim 4.09 \text{ \AA}$



Appendix 9: The original XRD data of the study samples represented in 2 theta diffractograms



Major peaks of the opaline silica polymorphs opal-A (OA), opal-C (OC), and opal-CT (OCT) samples



Diffractograms of the crystalline silica series quartz, chalcedony, cristobalite and the silicic acid-synthesized tridymite

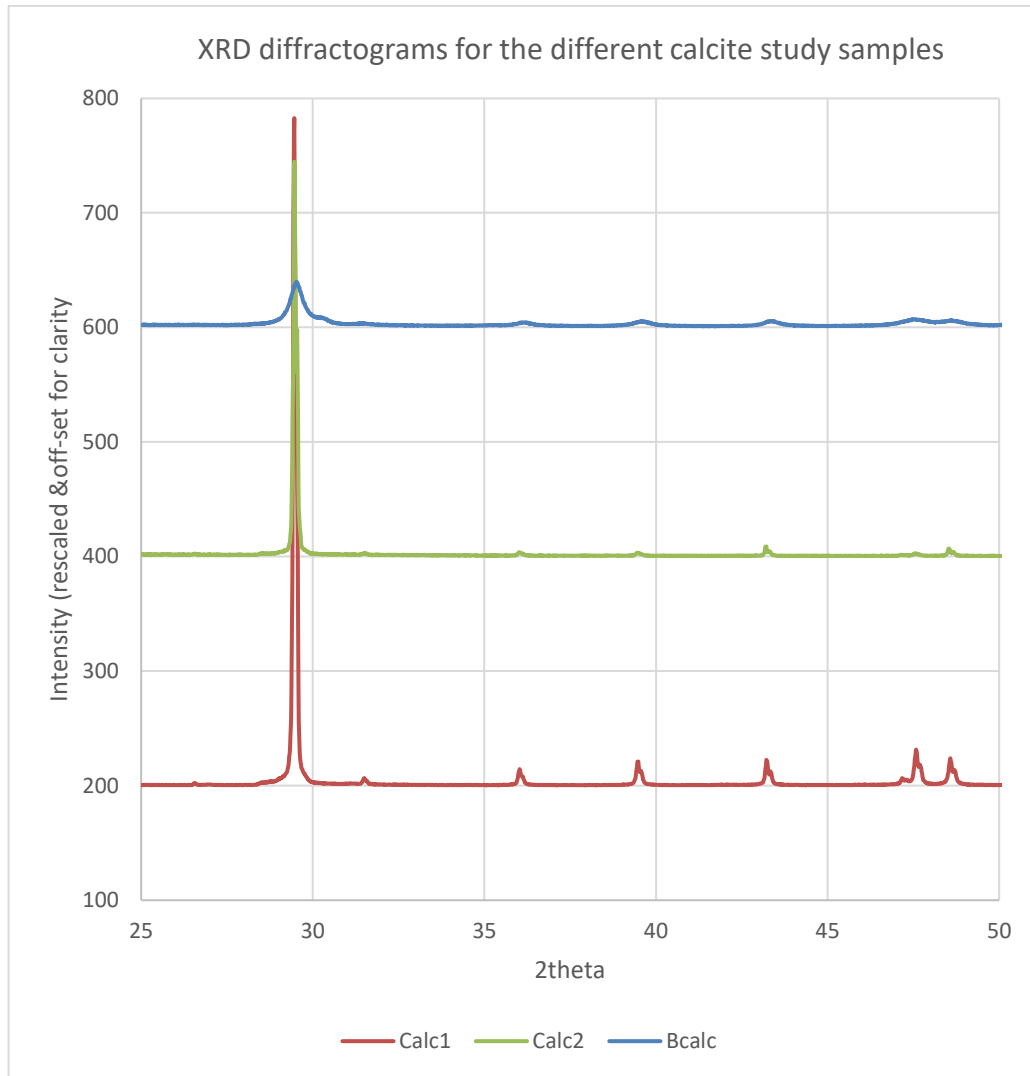


Figure showing the intensity differences of the study calcite samples in 2 theta. Bcalc representing bladed calcite